CR–206882

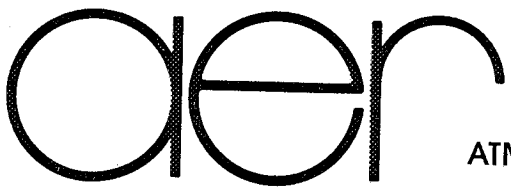

ATMOSPHERIC AND ENVIRONMENTAL RESEARCH, INC.

December 16, 1997

Dr. Yogesh Sud
Code 913
NASA Goddard Space Flight Center
Greenbelt, MD 20771

Re: Final report, contract NAS 5-32861 (AER Project P602)

Dear Dr. Sud:

This report, prepared by Atmospheric and Environmental Research, Inc., will function as the final report on the project.

We finished our assessments of the NASA Goddard Earth Observing System-1 Data Assimilation System (GEOS-1 DAS), regarding heating rates, energetics and angular momentum quantities. These diagnostics can be viewed as measures of climate variability. We have done extensive work, including comparisons with the NOAA/NCEP reanalysis system of momentum and energetics diagnostics. On these subjects, an extended abstract in the Proceedings of the American Meteorological Society Seventh Conference on Climate Variations has appeared (Enclosed), and we have also presented a report to the First International Conference on Reanalyses in October 1997. Our proceedings for that conference is also enclosed. A manuscript, entitled "Global momentum signals from reanalysis systems," by D.A. Salstein and R.D. Rosen, is under preparation for publication on this subject as well.

Two manuscripts on aspects of assessments of model behavior from the Atmospheric Model Intercomparison Project (AMIP), in which two Goddard general circulation models participate, have been accepted by journals. They are focused on atmospheric angular momentum (Hide, R., J.O. Dickey, S.L Marcus, R.D. Rosen, and D.A. Salstein, 1997: Atmospheric angular momentum fluctuations in global circulation models during the period 1979-1988. J. Geophys. Res., 102, 16423-16438), and water vapor and its transports (Gaffen, D.J., R.D. Rosen, D.A. Salstein, and J.S. Boyle, 1997: Evaluation of tropospheric water vapor simulations from the Atmospheric Model Intercomparison Project, J. Climate, 10, 1648-1661). Copies of reprints are included.

Dr. Salstein submitted two "Diagnostic Subproject proposals" to the Program for Climate Model Diagnosis and Intercomparison of the Lawrence Livermore National Laboratory to continue the work on atmospheric diagnostics in the areas of angular momentum and water vapor. Dr. Salstein will take the lead in the proposal on angular momentum and he is a participant in the proposal on water vapor and its transports. Both proposals were accepted. This acceptance will lead to involvement in the "AMIP-2" project, in which more advanced models will be used for these intercomparisons. Here, the models in the intercomparison projects will be run for 18-year periods, an extension of the previous project that will encompass more ENSO events.

840 MEMORIAL DRIVE, CAMBRIDGE, MA 02139-3794
TEL: (617) 547-6207 FAX: (617) 661-6479

December 16, 1997

Dr. Yogesh Sud
Code 913
NASA Goddard Space Flight Center
Greenbelt, MD 20771
page 2

We have noted that GEOS-1 and NOAA/NCEP global atmospheric angular momentum values are coherent on time scales down to about three days. Furthermore, they agree with the series of Earth angular momentum, as measured by tiny fluctuations in the rotation rate of the Earth, reckoned as variations in the length of day. The torques that effect such changes in atmospheric and Earth momentum consist principally of the friction torque, acting tangentially, against the surface of the land and the mountain torque, based on normal pressure gradients against the mountainous topography. Our work has shown the influence of particular mountain systems, including the Rockies, Himalayas, and Andes, upon mountain torques on time scales shorter than about two weeks. Aspects of this work were presented at the Fall American Geophysical Union in December 1996. Other portions of the work, as well as a paper on the AMIP project, were presented at the European Geophysical Society meeting in April 1997. A manuscript, entitled "Regional sources of mountain torque variability and high-frequency fluctuations in atmospheric angular momentum," by Iskenderian and Salstein, has been accepted and is in press at *Monthly Weather Review* (copy enclosed). We hosted Olivier de Viron, a visiting student from the Royal Observatory of Brussels, who calculated the torques from the GEOS-1 DAS analyses that link the surface pressure patterns of the atmosphere with various motions of the Earth. In so doing we have also investigated the "gravitational torque" associated with the pull of the Earth on the changing mass of the atmosphere. A manuscript (De Viron, O., Ch. Bizouard, D. Salstein , and V. Dehant, 1997: Atmospheric torque on the Earth and comparison with the atmospheric angular momentum variations) is under preparation on the results of this work; a copy of the abstract is enclosed.

We have been involved in a collaboration with Dr. Sud, of Goddard Space Flight Center, whose purpose is to examine the impact of mountainous areas on diagnoses of the atmosphere. To that end we have examined one year of data from three experiments, in which (1) the full Himalayan mountains are included (2) the Himalayan mountains have been reduced to 50% of their height, and (3) the Himalayan mountains have been reduced to 10% of their height. Some initial findings of the study are as follows: The largest impact of the Himalayas occurs in the Northern Hemisphere during winter season, and, most specifically, during February and March. This result indicates that the variations of wind and temperature during this cold season lead to a reduction in the eddy kinetic energy and eddy-available potential energy, indicating the necessity of this mountainous area for producing the phenomena under question. We have studied the zonal mean and eddy kinetic and available potential energy values for the SIB147 run (full mountains), SIB149 run (50% mountains) and SIB148 (10% mountains. Interestingly the zonal mean energy terms appear to affected by the mountains in the Northern Hemisphere, especially in the winter.

Earlier in the project, Dr. Salstein convened and chaired a session at the Spring 1996 American Geophysics Union Meeting in Baltimore, on the topic of Earth System Dynamics. Participants in that session included invited speakers from NASA Goddard

December 16, 1997

Dr. Yogesh Sud
Code 913
NASA Goddard Space Flight Center
Greenbelt, MD 20771
page 3

Space Flight Center, who highlighted the developments of the Goddard Laboratory for Atmospheres, in relation to the atmospheric component of the planetary angular momentum balance.

We worked out assessments of the NASA Goddard Earth Observing System-1 Data Assimilation System (GEOS-1 DAS), regarding energetics and angular momentum quantities. The energetics diagnostics, in particular, are useful in determining a measure of the types of climate signals during the multi-year period already analyzed as part of the GEOS DAS-1 reanalysis effort. For example, we see a distinct difference in the zonal mean and in the eddy kinetic energy terms between a year featuring a warm Pacific water El Niño event (1987) and one that had a cold La Niña event (1988). We presented some of our results concerning this topic at the Annual NOAA Climate Diagnostics Workshop in November 1995, in a presentation entitled, "Angular momentum and energetics in reanalysis products." There we focused on comparisons of the NASA EOS DAS-1 system with the NOAA NCEP/NCAR Reanalysis Project. Some of the differences in the energetics terms led us to conclude that the mean zonal winds and eddy terms had considerable differences. A copy of the relevant Proceedings contribution from that workshop is enclosed.

In a related vein, we have compared the heating rates from the GEOS DAS-1 with values of outgoing longwave radiation for an eight-year period. We found, in particular, that there is considerable correlation in the west central Pacific between (negative) heating and vertically averaged latent heating. Also, comparisons of latent heating in a Goddard Global Circulation Model with and without the inclusion of downdrafts were performed. The effect of such a parameterization is particularly influential in the tropics. An Extended Abstract for the AMS Tenth Conference on Numerical Weather Prediction, addresses this subject and is included here too.

A book chapter by D.A. Salstein, Mean Properties of the Atmosphere, in *Composition, Chemistry, and Climate of the Atmosphere* has been published with some support from this NASA Program. Enclosed is a single copy of this chapter in its final form.

Sincerely yours,

David A. Salstein

David A. Salstein
Principal Investigator

Enclosures

cc: Contracting Officer, Code 289, 1 copy
Center for AeroSpace Information, 2 copies, Publications and graphics services section, Code 253.1

Preprints

TENTH CONFERENCE ON NUMERICAL WEATHER PREDICTION

July 18-22, 1994

Portland, Oregon

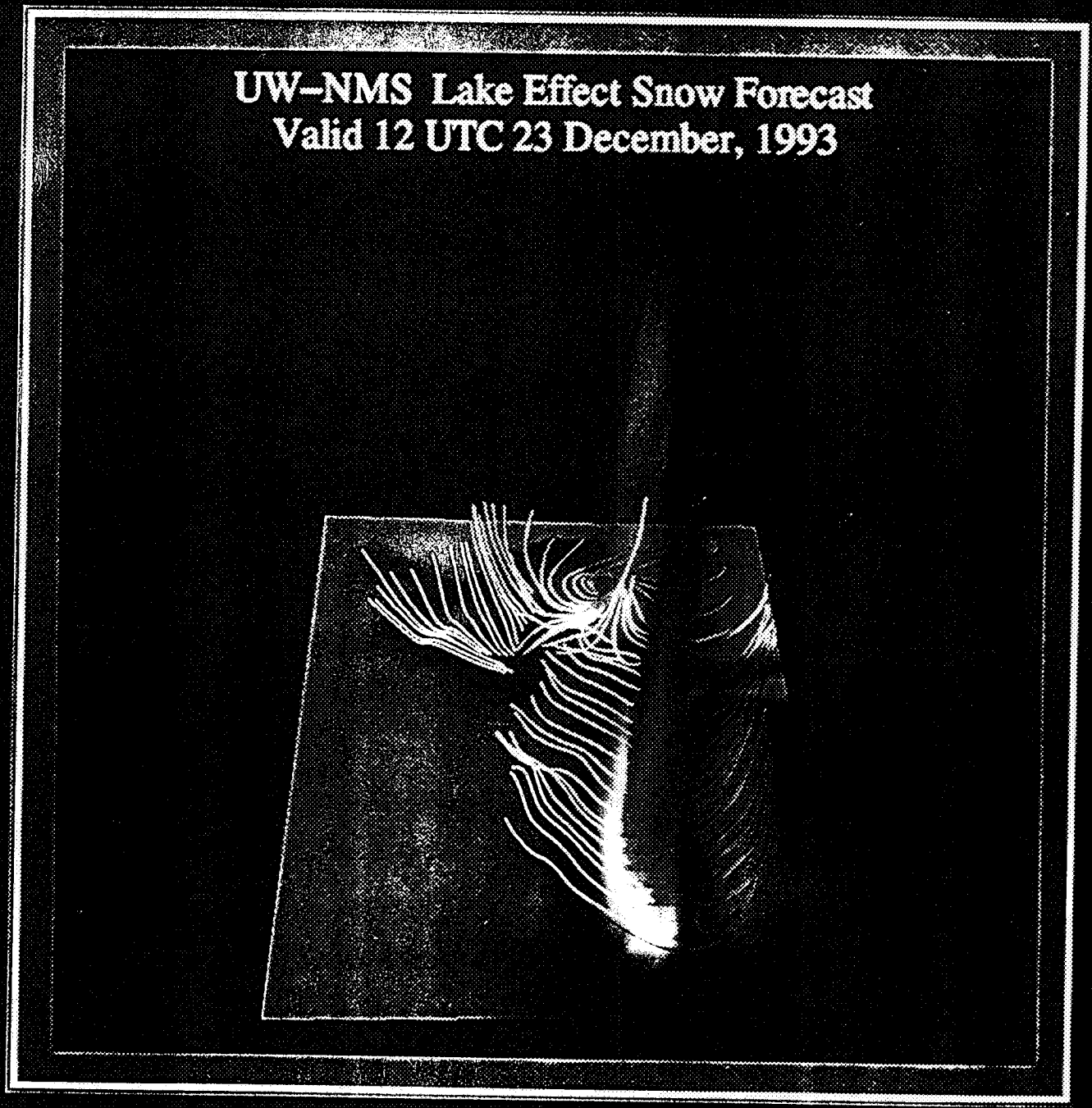

AMERICAN METEOROLOGICAL SOCIETY

3B.3 LARGE-SCALE DIABATIC HEATING IN A MODEL WITH DOWNDRAFTS

David A. Salstein[1] and Yogesh C. Sud[2]

[1]Atmospheric and Environmental Research, Inc., Cambridge, MA 02139
[2]Laboratory for Atmospheres, NASA Goddard Space Flight Center, Greenbelt, MD 20233

1. INTRODUCTION

A physically based scheme was developed and implemented by Sud and Walker (1993) to include the effects of convective downdrafts (CD) to complement a parameterization for moist convection. It calculates the downdraft mass flux at different levels in the atmosphere and is designed to augment the parameterization that includes the re-evaporation of rain (Sud and Molod 1988).

The CD scheme has been included here in a one-year simulation with the 17-layer GLA General Circulation Model (GCM) documented in Table 3 of Sud and Walker (1993). Parallel to this run is a CONTROL simulation without the CD parameterization. Over the maritime tropical continent, Sud and Walker (1993) note that after implementing CD, a reduction occurs in the precipitation, which was excessive there in simulations without CD; other regions have marginal changes in precipitation.

The simulations were used to examine the impact of the CD parameterization on diabatic heating component fields studied by Salstein and Rosen (1990) for the 9-layer version of the GLA GCM. The availability of the heating component fields allows an assessment of their relative roles in driving the global atmospheric energy cycle, through the generation of available potential energy, G(APE). Thus, we re-evaluate this aspect of the energy cycle here.

We examine the distribution of diabatic heating and its roles in the propagation of intraseasonal fluctuations in the tropics, and also in generating APE in each hemisphere. Because CD has a strong impact on latent heating due to the cooling effect of rain re-evaporation, a particular focus is on that heating component.

2. INTRASEASONAL SIGNALS IN LATENT HEAT

Temporal changes in patterns of latent heating, like those in precipitation, are related to the large-scale dynamics of the atmosphere. On intraseasonal time scales, fluctuations in latent heating produced by convection in the tropics may be a signature of the Madden-Julian oscillation. Convection, in turn, is related to the rising motion, and hence divergence in the upper atmosphere. Knutson and Weickmann (1987) have documented intraseasonal oscillations in potential fields, related to the divergence, which typically are manifested as eastward-moving patterns in the deep tropics. Here we calculate vertically averaged patterns of latent heating throughout much of the depth of the free atmosphere in the deep tropics (10S-10N). Aspects of motion at different time scales of latent heat patterns produced by the simulation are examined either by considering the raw fields directly or by filtering them in specific intraseasonal bands, as Vincent et al. (1991) did in studying 200-hPa potential fields calculated from ECMWF analyses. On rapid scales, some pulses in the raw latent heating, moving westward across the tropical Atlantic to South America, can be seen in Fig. 1. After applying a filter in the 40-80 day band (Fig. 2a), cases of tropical eastward propagation in latent heating become clear. In this band, propagation patterns typically start over Africa, or the Indian Ocean, and travel to the central Pacific, occasionally moving farther east across the date line with time scales of motion of about two months. After applying instead a band-pass filter at shorter periods, between 27-44 days, eastward propagation also occurs [not shown], though

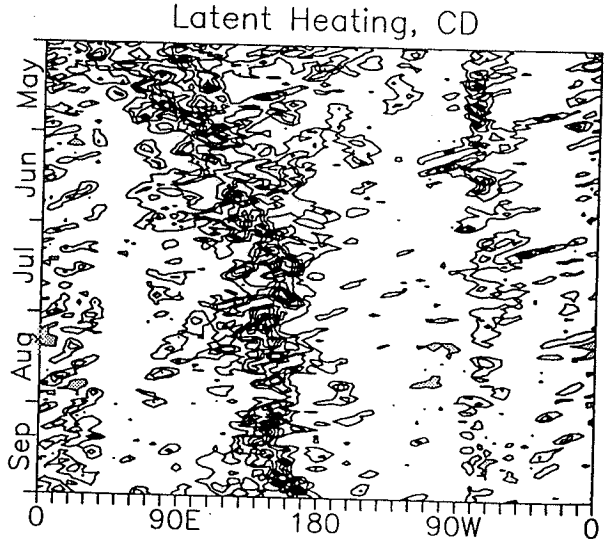

Fig. 1. Distribution in time and longitude of latent heating between 10N and 10S, averaged between 850 and 200 hPa, from the GLA model including convective downdrafts for 5 months of a simulation. Contours are 2 K day^{-1}.

with almost double the speed. After band-pass filtering, the westward-moving pulses in Fig. 1 vanish.

Comparing results from Fig. 2a with a similar analysis of the CONTROL run (Fig. 2b) reveals some differences in character. The bands with peaks between 0 and 90E in May and June, for example, have stronger amplitude in the CD case than in the CONTROL case. Also, the patterns have somewhat less of a standing character near 150E in CD. To isolate the traveling disturbances more compactly, eigenvector approaches, such as extended Empirical Orthogonal Function analysis are useful.

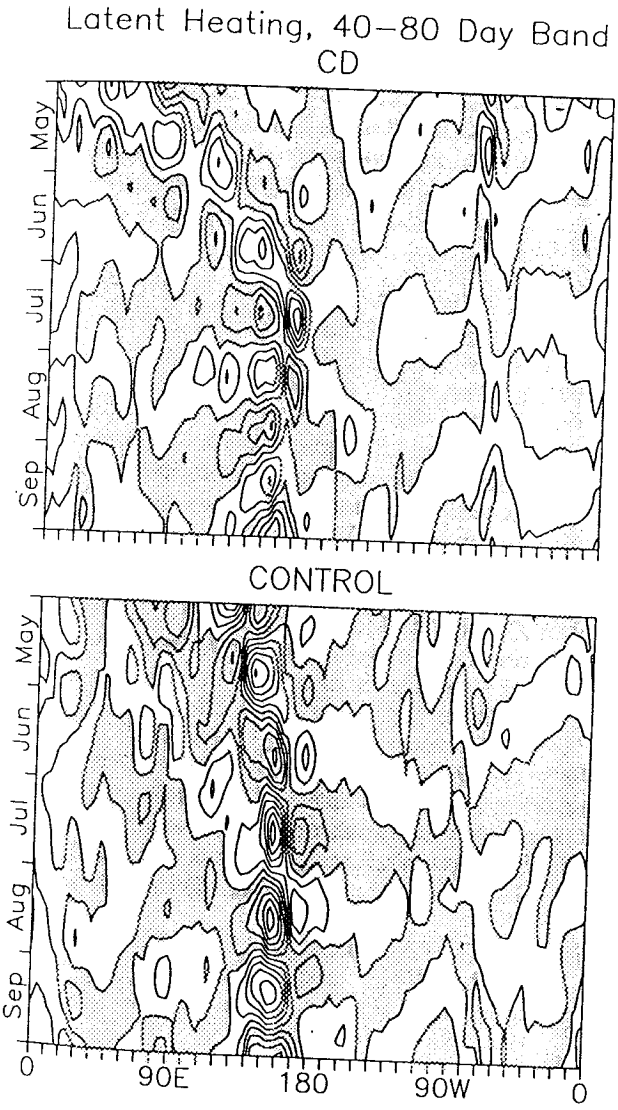

Fig. 2(a). Same as Fig. 1, but after applying a 40-80 day band-pass filter. Contours are 0.5 K day^{-1}. (b) Same as (a), but for CONTROL.

3. DIABATIC HEATING AND ENERGETICS

To determine the role of the heating fields from the CD run on the large-scale energetics of the atmosphere, we have first calculated monthly and annual distributions of the four components of diabatic heating. We isolate from the CD run the mean annual distribution of the four components of diabatic heating; zonal mean annual cross-sections are shown in Fig. 3.

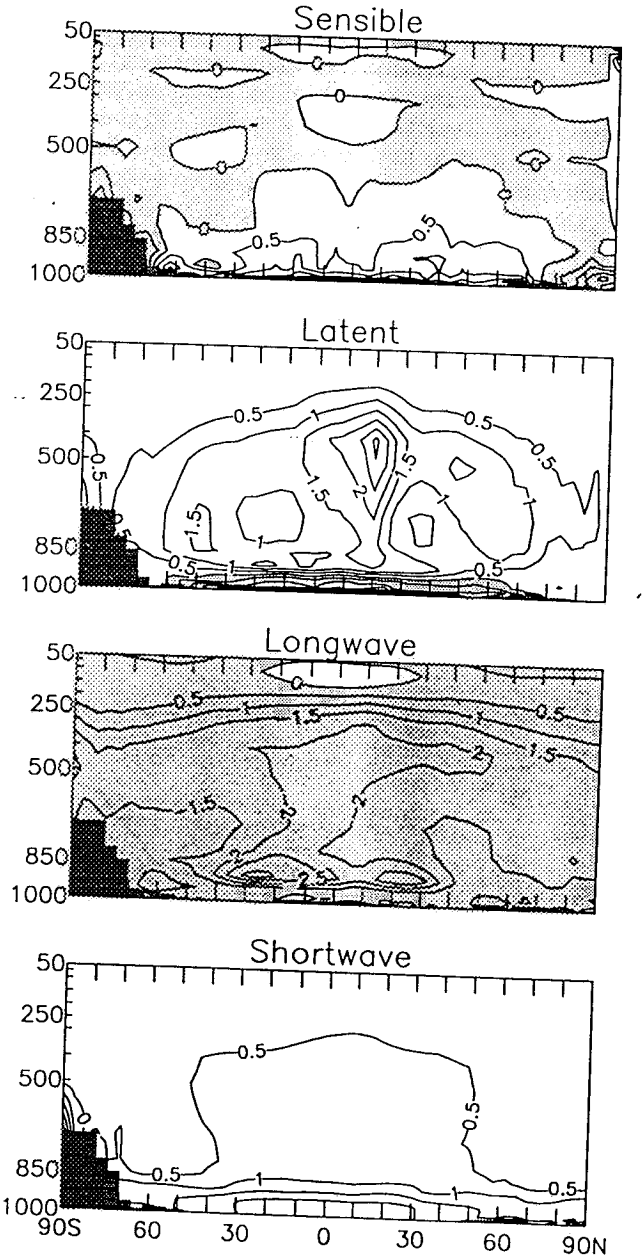

Fig. 3. Annual and zonal mean values of four components of diabatic heating, from the simulation with convective downdrafts. Units are K day^{-1}, and negative values are shaded.

In addition to the strong latent heating through the depth of the free atmosphere, a shallow area of cooling from the evaporative downdrafts is also visible; such cooling is larger than is the case of CONTROL without evaporative downdrafts. Correspondingly, sensible heating of the boundary layer becomes larger for the CD simulation as compared to the CONTROL run [not shown], compensating in part for the latent cooling there.

When each of the four fields is combined with the temperature fields on a daily basis, values for the generation of available potential energy by the heating processes can be obtained. Both the zonal mean portion and eddy portions of G(APE) can be computed from these fields. Typically, latent, sensible, and shortwave processes tend to have a positive G(APE) due to a positive correlation with temperature; longwave has a negative correlation and hence reduces the APE.

We present in Fig. 4 the generation of zonal mean APE in each hemisphere in the "free" atmosphere between 950 and 50 hPa from CD run. The annual cycles of these terms are considerable, and the values in the two hemispheres are largely out of phase with each other. The values of G(APE) due to latent and sensible heating in the low boundary layer, 1000 - 950 hPa, are small parts (by amplitude) of G(APE). However, the proportion of these two components produced in the boundary layer is relatively large considering the shallowness of that layer. In November, the month of the largest magnitude boundary layer value for G(APE) by latent heating in the NH, its value is nearly 20% of that in the free atmosphere and it is of opposite sign, reducing the strength of G(APE) by the latent process. In turn, extra G(APE) from boundary layer sensible heating tends to compensate for this reduction.

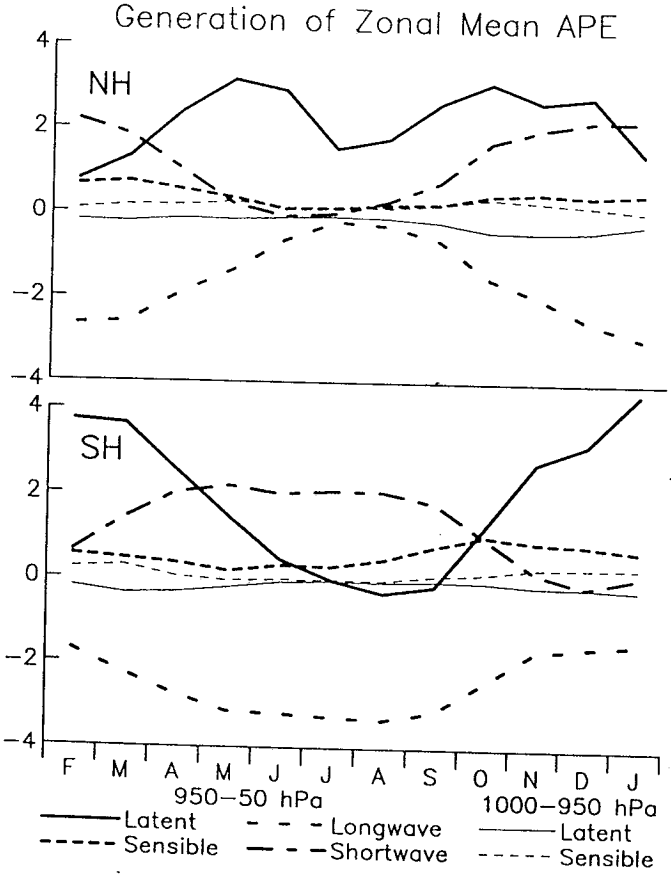

Fig. 4. Generation of zonal mean available potential energy in the northern and southern hemispheres, for each month of the simulation with convective downdrafts by four components in the free atmosphere (950-50 hPa), and for latent and sensible heating in the boundary layer (1000 - 950 hPa). Units are Wm^{-2}.

ACKNOWLEDGMENTS: The work was supported under NASA Contract NAS5-31333 to AER. We thank P. Nelson of AER and G. H. Walker of GSFC for help in production of the data and analyses. R.D. Rosen of AER made several helpful comments on this work.

REFERENCES

Knutson, T.R., and K.M. Weickmann, 1987: 30-60 day atmospheric oscillations; Composite life cycles of convection and circulation anomalies. *Mon. Wea. Rev.*, 115, 1407-1436.

Salstein, D.A., and R.D. Rosen, 1990: Comparisons of model-produced heating component fields. Proceedings of the Fourteenth Annual Climate Diagnostics Workshop, U.S. Dept. Commerce/NOAA, 250-155.

Sud, Y.C., and A. Molod, 1988: The roles of dry convection cloud radiation feedback processes and the influence of recent improvements in the parameterization of convection in the GLA GCM. *Mon. Wea. Rev.*, 116, 2366-2387.

Sud, Y.C., and G.H. Walker, 1993: A rain evaporation and downdraft parameterization to complement a cumulus updraft scheme and its evaluation using GATE data. *Mon. Wea. Rev.*, 121, 3019-3039.

Vincent, D.G., T.M. Sperling, A. Fink, S. Zube, and P. Speth, 1991: Intraseasonal oscillation of convective activity in the tropical Southern Hemisphere. *J. Clim.*, 4, 40-53.

Angular momentum and energetics in reanalysis products

David A. Salstein and Richard D. Rosen
Atmospheric and Environmental Research, Inc., Cambridge, MA 02139

1. *Introduction.* Questions about climate variability demonstrate the need to reanalyze the historical state of the atmosphere using a modern analysis system applied to as consistent a set of observational data as possible. Two such reanalysis sets are now being prepared: one by NCEP/NCAR, eventually spanning several decades (Kalnay and Jenne 1991); and one using the NASA Goddard Earth Observing System Data Assimilation System (GEOS-1 DAS), being run for about a decade but developed with future inputs of space-based data in mind (Schubert et al. 1991).

The currently available pilot series from these reanalyses span more than five years. Here we examine the potential for these data to contribute to climate studies by considering aspects of the planetary budgets of atmospheric angular momentum and energetics.

2. ***Angular momentum diagnostics.*** Atmospheric angular momentum (AAM) about Earth's axis is a well-determined quantity, which has been shown to be remarkably consistent with measurements of the Earth's rotation rate in that its variations are proportional to those in the length of day (l.o.d.) on timescales between several days and years. In addition, AAM is being used as a verification tool for atmospheric models (Salstein and Rosen 1994) such as those contributing to the Atmospheric Model Intercomparison Project. Estimates of this quantity have been made from several weather centers (Salstein et al. 1993), and although values produced by different centers had moderate differences a decade or more ago, they are in better agreement today. New estimates of AAM based on reanalyses have the potential to reduce the errors that existed in earlier years.

The difference between AAM and equivalent values of l.o.d. for individual years is typically smaller when the AAM value is based on NCEP/NCAR reanalysis than when it is derived from operational analyses. Indeed, a seven-year set (1985-91) of values shows the reduction in rms to be about 30%; this result (Fig. 1) was determined using the full vertical extent of the analysis domains and after removing a low-order signal not related to atmosphere-solid Earth momentum exchange.

The differences in AAM between reanalyses and operational analyses appear to derive from zonal winds in the tropics and southern hemisphere mid to high latitudes. Reanalysis appears to have stronger easterly momentum than do operational values, in general. Interestingly also, reanalysis-based AAM values are temporally smoother than their operational counterparts, as a spectral analysis of such values over the five years demonstrates (Fig. 2).

An advantage of reanalysis data derives from the inclusion of higher levels than was the case heretofore. Use of such levels is typically required for momentum balances on seasonal scales (Rosen and Salstein 1991). For example, the semiannual amplitude in l.o.d. of 0.173 milliseconds during 1985-91 is not matched by the troposphere alone (amplitude equivalent to 0.116 ms), but including of the stratosphere up to the 20 millibar level reduces the difference with the l.o.d.-derived value by about one half (amplitude equivalent to 0.144 ms).

Values of AAM, when distributed into zonal belts, can be used to study the structure of climate anomalies. The GEOS-1 system, for example, shows the 1987 El Niño maximum and 1988 La Niña minimum in the subtropics, each signal with a precursor near the equator one year earlier.

Such a result, first noted by Dickey et al. (1991), may eventually be generalized over many decades with the reanalysis-based values.

NCEP/NCAR and NASA GEOS-1-based values of AAM are in rather close agreement with each other, with the two sets showing a strong coherence on intraseasonal time scales that remains statistically significant down to about three days (Fig. 3). From this result, we may infer that the reanalysis sets have consistent zonal wind fields.

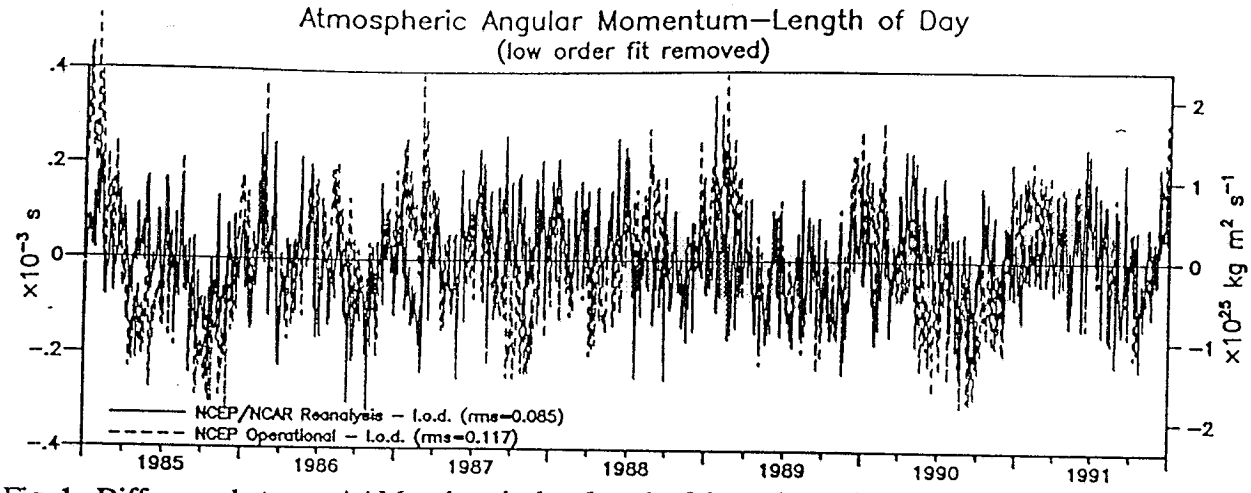

Fig. 1. Difference between AAM and equivalent length of day values, given in two proportional scales, l.o.d. on left and AAM on right. AAM is derived from NCEP/NCAR reanalyses and NCEP operational analyses. A low-order fit, representing non-atmospheric effects, is removed from the difference series.

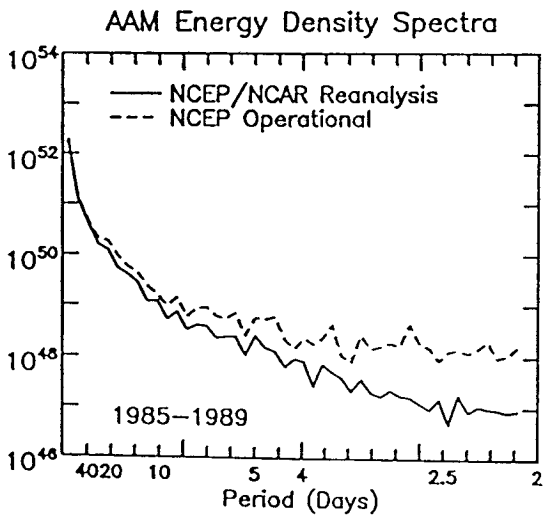

Fig. 2. Energy density spectra of AAM from NCEP/NCAR reanalyses and NCEP operational analyses for 1985-1989, based on once-daily values. Units are (kg m^2 s^{-1})^2 x day.

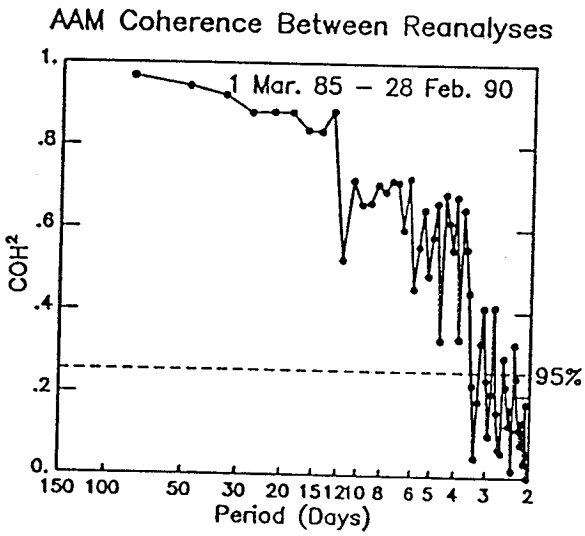

Fig. 3. Square of coherence between AAM values (to 20 millibars) from the NCEP/NCAR and NASA GEOS-1 DAS reanalyses over five years,and an estimate of the 95% level of significance.

3. *Energy diagnostics.* The atmosphere may be considered as a heat engine in which potential energy is converted into kinetic energy (Peixoto and Oort 1992). Moreover, these energy forms may be partitioned into their zonal mean and eddy components, with conversions taking place between such components by actions of meridional eddy transports. Potential energy is generated through differential heating of the atmosphere through diabatic processes; the generation of its zonal mean form, for example, requires a positive correlation of heating rate and temperature across the (hemispheric or global) domain. The diabatic processes involved are those of sensible, latent, longwave radiational, and shortwave radiational heating.

Signals in the strength of atmospheric energy forms, conversions, and generation can be indicative of important interannual variations. We used the first five years of the NASA GEOS-1 analysis to analyze atmospheric energetics in monthly periods. Potential and kinetic energy contents of each hemisphere display strong annual signals, with all zonal mean and eddy components strongest during a hemisphere's winter. Furthermore, the northern hemisphere signal dominates the seasonal signal. When the mean seasonal cycle is removed, the transition from 1987 El Niño maximum to 1988/1989 La Niña minimum is clearly visible in the energy signals in both hemispheres (Fig. 4). The time series of zonal mean available potential energy generation displays a signal in which the portion associated with latent heat explains much of the character of total energy generation (Salstein and Sud 1994). Moreover, interannual signals in anomaly generation terms also indicate an impact of the ENSO cycle.

We have also made a preliminary estimate of the differences in the energetics between the NCEP/NCAR and GEOS-1 DAS reanalyses during the 1987-1988 period, which are relatively small (only 5% or less of the typical values). Some of the larger differences are in the zonal mean available potential energy in the southern hemisphere and eddy kinetic energy in both hemispheres, in which the NCEP/NCAR values tend to be less than those of GEOS-1 DAS. After examining zonal-mean zonal wind values, we find, for March 1988, the month with the largest difference in mean kinetic energy, that such a difference is related to the strength and position of the jets, which tend to be stronger and placed more equatorward in the NCEP/NCAR analysis. As for eddy kinetic energy, the two-year mean conditions show that the zonal mean variance in the winds in NCEP/NCAR is less than that of GEOS-1 throughout much of the globe, but in particular in the southern hemisphere jet, which is centered near 50S and 250 millibars (Fig. 5).

4. *Acknowledgments.* Support for this study came from NOAA Climate and Global Change Program grant NA46GP0212, and from NASA EOS Program grant NAGW-2615 and Global Modeling and Analysis Program contract NAS5-32861.

5. *References*

Dickey, J. O., S. L. Marcus, and R. Hide, 1992: Global propagation of interannual fluctuations in atmospheric angular momentum. *Nature*, 357, 484-488.

Kalnay, E. and R. Jenne, Summary of the NMC/NCAR reanalysis workshop of April 1991. *Bull. Amer. Metoeorol. Soc.*, 72, 1897-1904.

Peixoto, J.P., and A.H. Oort, 1992: *Physics of Climate*, Amer. Inst. Phys., New York, 520 pp.

Rosen, R.D., and D.A. Salstein, 1991: Comment on "A seasonal budget of the Earth's axial angular momentum" by Naito and Kikuchi. *Geophys. Res. Lett.*, 18, 1925-1926

Salstein, D.A., D.M. Kann, A.J. Miller, and R.D. Rosen, 1993: The Sub-bureau for Atmospheric Angular Momentum of the International Earth Rotation Service: A meteorological data center with geodetic applications. *Bull. Amer. Meteorol. Soc.*, 74, 67-80.

Salstein, D.A., and R.D. Rosen, 1994: Validation of model-based and analyzed momentum and moisture diagnostics. *Proc. 19th NOAA Climate Diagnostics Workshop*, College Park, MD.

Salstein,D.A., and Y. Sud.1994: Large-scale diabatic heating in a model with downdrafts. *Proc. 10th Conf. on Numerical Weather Prediction*, Amer. Meteror. Soc., 72-74.

Schubert, S. D., R.B. Rood, and J. Pfaendtner, 1993: An assimilated dataset for Earth science applications. *Bull. Amer. Meteorol. Soc.*, 74, 2331-2342.

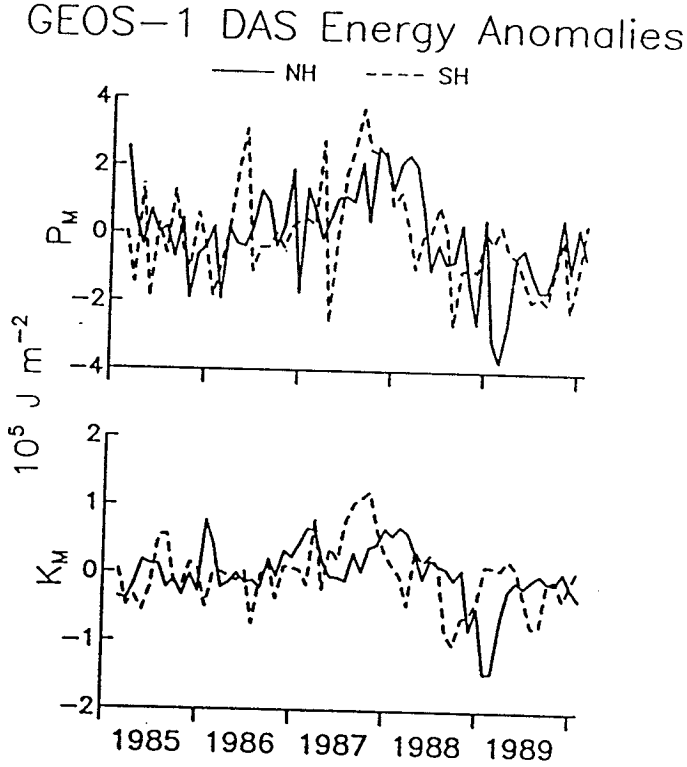

Fig. 4. Hemispheric anomaly values from five-year calendar-monthly means for zonal mean potential and zonal mean kinetic energies, based on the NASA GEOS-1 DAS system.

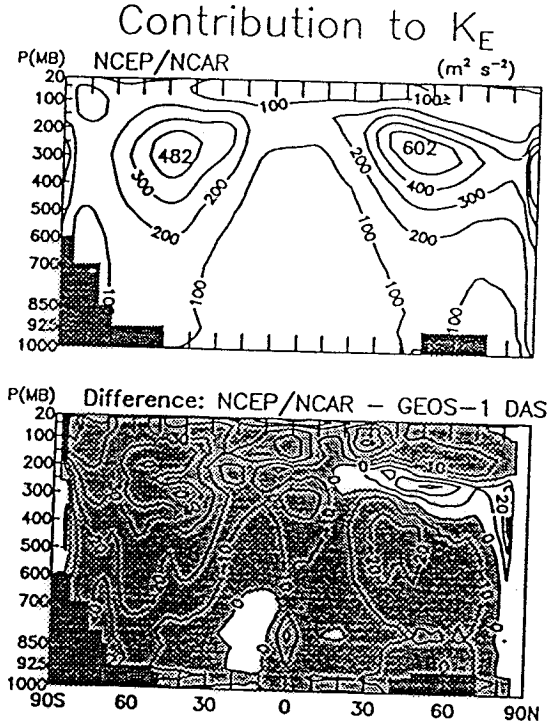

Fig. 5. Pressure-latitude distribution, 1987/88 of the mean square transient and standing eddy wind components from one reanalysis and from the difference between two reanalyses. Values are proportional to eddy kinetic energy. Light and dark shading represent negative values and high topography regions respectively.

COMPOSITION, CHEMISTRY, AND CLIMATE OF THE ATMOSPHERE

▼

Edited by

Hanwant B. Singh

VAN NOSTRAND REINHOLD
I(T)P™ A Division of International Thomson Publishing Inc.
New York • Albany • Bonn • Boston • Detroit • London • Madrid • Melbourne
Mexico City • Paris • San Francisco • Singapore • Tokyo • Toronto

Proceedings, First International Conference on Reanalyses

GLOBAL MOMENTUM AND ENERGY PARAMETERS FROM REANALYSES

David A. Salstein and Richard D. Rosen
Atmospheric and Environmental Research, Inc.
840 Memorial Drive, Cambridge, Massachusetts 02139 USA
Telephone: 617-547-6207
Telefax: 617-661-6479
e-mail: salstein@aer.com

ABSTRACT

Global atmospheric angular momentum and energy parameters have been computed four times daily from the NCEP/NCAR and NASA GEOS-1 systems. Global momentum from both reanalyses are significantly coherent on periods greater than 2-3 days. Atmospheric angular momentum series based on reanalyses agree better with Earth rotation changes than did operationally-based estimates. Because the reanalysis domain includes most of the stratosphere, prominent quasi-biennial and semi-annual signals are better represented than in previous operationally-based products. Moreover, the lengthy reanalyses allow an investigation of anomalous behavior like that of the current El Niño event, which is characterized by strong westerly momentum anomalies between 30 S and 30 N.

Large-scale kinetic and potential energy statistics have also been calculated using reanalysis-based winds and temperatures. Moreover, the generation of available potential energy, $G(P_M)$, is estimated from diabatic heating fields obtained from the model residing within reanalysis systems. Lengthy series of zonal mean potential energy, kinetic energy, and $G(P_M)$ all display evidence of ENSO forcing. ENSO anomalies in tropical latent heating are prominent in producing negative anomalies of energy generation.

1. INTRODUCTION

Reanalysis fields from the National Centers for Environmental Prediction/National Center for Atmospheric Research (NCEP/NCAR) [1] since 1968 and the NASA Goddard Earth Observing System Data Assimilation System [2] for 1980-1995 are used here to calculate global and regional values of atmospheric angular momentum and energetics quantities. These parameters may be used to monitor various aspects of dynamics within the atmosphere and the whole Earth system, and they also function as indices of climate. Such global statistics are also useful because they are related to other properties of the planet including its rotation rate (length of day) and its energy balance, both of which may be monitored by independent techniques.

Besides the advantage that the reanalyses have removed many of the heterogeneities of operational analyses, their domain also extends higher through much of the upper stratosphere (to 10 hPa for NCEP/NCAR and about 20 hPa for GEOS-1 DAS), as opposed to the 50 hPa level for earlier analyses. Thus, global momentum and energetics diagnostics over a broad range of time scales can be more confidently assessed.

2. ATMOSPHERIC ANGULAR MOMENTUM (AAM) DIAGNOSTICS

The signature of global mean AAM [3] based on nearly three decades of NCEP/NCAR reanalyses (Fig. 1) includes a dominant seasonal component and interannual variability with peaks in El Niño years, the strongest of which occurred during the 1982-83 ENSO warm event. Global values of AAM from the two reanalyses are very close, with an r.m.s. difference (after means have been removed) of 0.32×10^{25} kg m^2 s^{-1} during the 15-year period that both sets overlap. A coherence analysis between the two sets shows significant agreement on variations of around 2-3 days and longer (Fig. 2). Coherences in Fig. 2 do begin to fall below 0.6 at around a 10-day period, although there is evidence (not shown) that the two series have become closer since 1980, especially in the band between 3 and 6 days.

Root-mean-square differences between the angular momentum of the atmosphere and that of the solid Earth, determined from geodetic measurements of the length of day, are typically small, as would be expected from the conservation of angular momentum in the Earth-atmosphere system. These differences (Fig. 3) are about 25 per cent lower when AAM values from NCEP/NCAR reanalysis are used than

differences based on the operational AAM values. Thus we conclude that a significant improvement has taken place in the quality of the reanalysis fields, compared with the previous operational product.

The AAM values during the current calendar year have been anomalously high compared to the long-term record, for several months, particularly since mid-July (Fig. 4a). This anomaly appears to be a consequence of the current El Niño that began to form in March/April 1997. When the global signals are separated regionally into latitude belts [3], positive anomalies spread across most of the low latitudes but particularly strong between 20 S and 30 S in recent months (Fig. 4b).

The raising of the upper level to 10 hPa in the NCEP/NCAR reanalyses allows us to study the long-term character of stratospheric angular momentum. In this regard, Fig. 5 shows the impact of the stratospheric quasi-biennial oscillation (QBO) on the global momentum above 100 hPa [4] with higher levels producing a stronger signal. Further analysis shows that the upper stratosphere is needed to provide enough momentum for global balance on the quasi-biennial scale. The stratosphere also contains a major semiannual signature, evident with a more rapid filter [not shown], which may be interpreted as a combination of annual momentum signatures in the two hemispheres that peak in different seasons.

3. ENERGETICS AND DIABATIC HEATING

The availability of the reanalysis fields, including those produced by the forecast model at the core of the reanalysis system, enables one to diagnose the complete energy cycle of the atmosphere. In this framework [5], the atmosphere can be viewed as a heat engine, producing kinetic energy from the portion of potential energy due to differential heating that is available for conversion. In earlier studies we focused on using monthly energy parameters to examine of the energy cycle from an analysis system and we used these values to assess the quality of the system [6]. Here we consider variability in the 15-year set of GEOS-1 DAS reanalysis-based energetics values.

Kinetic and available potential energy in its zonal mean and eddy forms have strong annual signatures in both hemispheres, all peaking in each hemisphere's respective winter season. Time series of anomalies from the annual cycle during 1980-95 (Fig. 6) reveal a marked decrease in zonal mean potential and kinetic energies from the El Niño warm event year of 1987 to the La Niña phase of cold Pacific sea surface temperatures in 1988-89. Potential energy, in particular, remains anomalously low for about four years after that period. The effects of the other El Niño events were less clear by this measure.

Available potential energy in the atmosphere is generated by diabatic heating, whose long-term rates from latent, sensible, and shortwave and longwave radiational processes are shown in Fig. 7a using GEOS-1 DAS. The strongest heating rates in the mid to upper troposphere derive from the latent process; sensible heating is strong but confined to the lowest layers. Heating by shortwave radiational processes is more than balanced by stronger cooling from longwave processes.

The relative importance of these heating terms to the energetics of the atmosphere can be assessed by examining $G(P_M)$, the generation of zonal mean available potential energy, which has been calculated for each month of the record from each heating term separately. This generation term depends approximately on the spatial correlation between the heating rates and the temperature field. Latent heating, tends to carry the annual signature of the total [7]. Northern Hemisphere interannual anomalies during El Niño years are negative, driven largely by the latent heat contribution (Fig. 7b). The strong 1983 extreme appears to be due to a southward shift in tropical latent heating compared to the mean position.

CONCLUSIONS

Atmospheric angular momentum (AAM) and energetics series from the NCEP/NCAR and GEOS-1 DAS reanalyses reflect a number of climatic signals. The AAM records are very consistent with observations of length of day; AAM values from the two reanalyses are coherent on all but very short time scales (<2-3 days). Inclusion of the stratosphere produces a strong quasi-biennial signal in AAM. Reanalysis-based series of kinetic and potential energies and mechanisms for energy generation identify El Niño signals.

ACKNOWLEDGEMENTS

The research reported here was supported under the NOAA Climate and Global Change Program through Grant NA46GP0212 the NASA General Circulation and Modeling Program through Contract NAS 5-32861, and NSF Grant ATM-9632559. Programming assistance was provided by P. Nelson of AER.

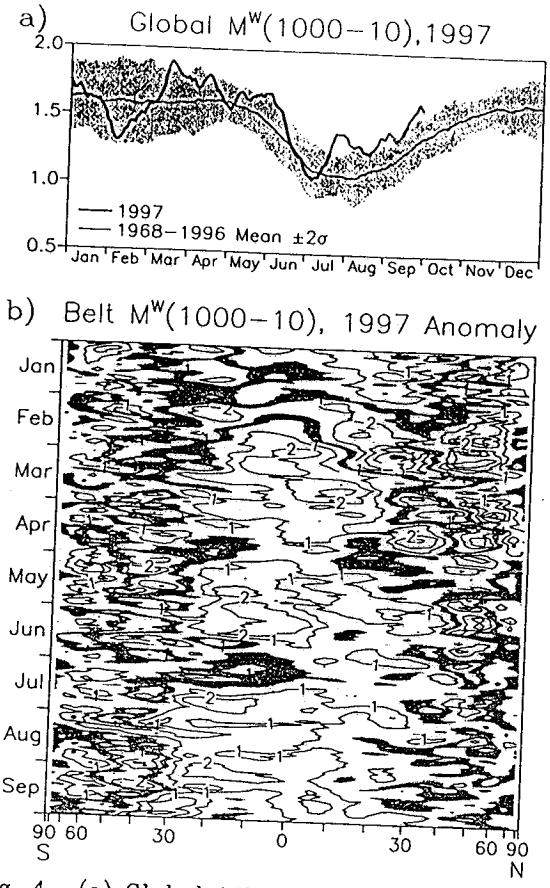

Fig. 4. (a) Global AAM 1997 values to date (heavy line), the mean annual series from the NCEP/NCAR reanalysis (light line) and its 2−standard deviation spread (shaded area). (b) Anomalies of 1997 AAM values in latitude belts from the long−term mean annual cycle. Positive values are anomalous westerly AAM; negative, easterly, AAM anomalies are shaded.

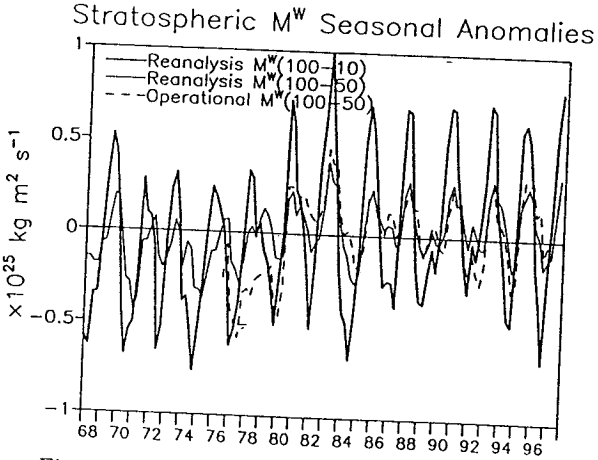

Fig. 5. Stratospheric AAM anomalies from the mean seasonal cycle between 10 and 100 hPa based on the NCEP/NCAR reanalysis (heavy solid), and between 10 and 50 hPa based on reanalysis (light solid) and operational (dashed).

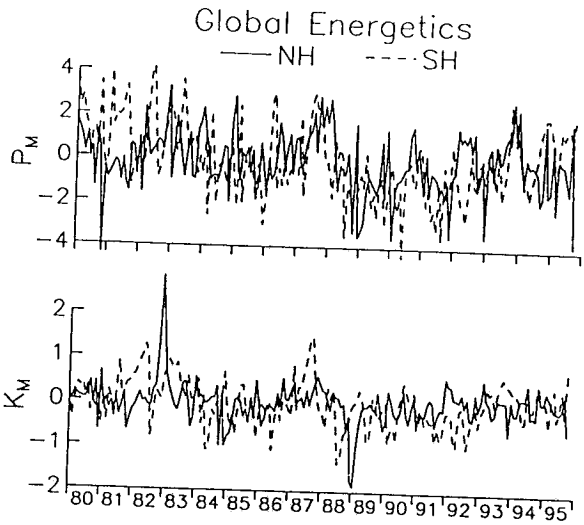

Fig. 6. Anomalies from the mean annual cycle of zonal mean available potential (P_M) and kinetic (K_M) energies, based on the GEOS−1 DAS analysis in both hemispheres. Units are 10^5 J m^{-2}.

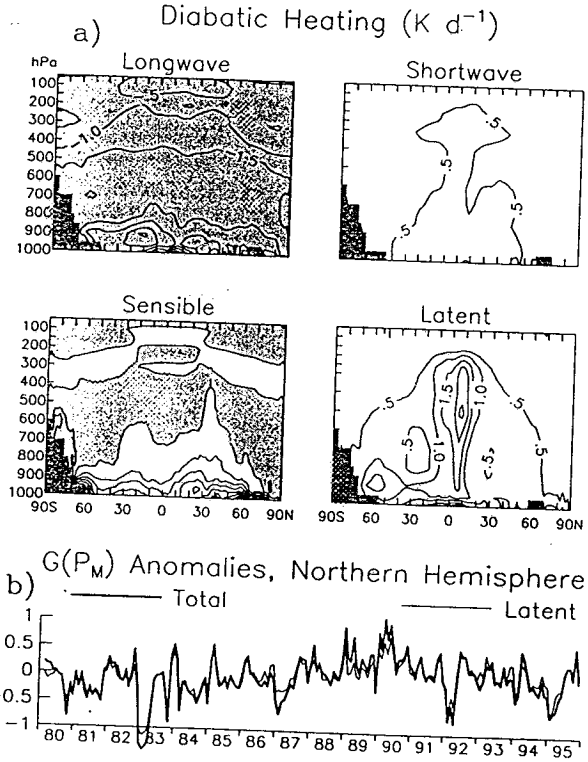

Fig. 7. (a) Zonal mean values of the four components of diabatic heating, based on the GEOS−1 DAS model, for 15 years. Negative values, denoting cooling, are shaded. Units are degrees per day. (b) Anomalies from the mean annual cycle of the generation of available potential energy in the N.H. for the latent component of diabatic heating and the total heating during all months over 15 years. Units are W m^{-2}.

REFERENCES

[1] Kalnay, E., et al., 1996: The NCEP/NCAR 40-year Reanalysis Project. *Bull. Amer. Meteorol. Soc.*, 77, 437-471.

[2] Schubert, S.D., R.B. Rood, and J. Pfaendtner, 1993: An assimilated dataset for Earth science applications. *Bull. Amer. Meteor. Soc.*, **74**, 2331-2342.

[3] Rosen, R.D., and D.A. Salstein, 1983: Variations in atmospheric angular momentum on global and regional scales and the length of day. *J. Geophys. Res.*, **88**, 5451-5470.

[4] Chao, B.F., 1989: Length-of-day variations caused by El Niño-Southern Oscillation and Quasi-biennial Oscillation. *Science*, **243**, 923-925.

[5] Peixoto, J.P., and A.H. Oort, 1992: *Physics of Climate*, AIP Press, New York, 520 pp.

[6] Salstein, D.A., R.D. Rosen, W.E. Baker, and E. Kalnay, 1987: Impact of satellite-based data on FGGE general circulation statistics. *Quart. J. Roy. Meteor. Soc.*, **113**, 255-278.

[7] Salstein, D.A., and R.D. Rosen, 1997: Global momentum and energy signals from reanalysis systems. Preprint volume, 7th Conf. on Climate Variations, American Meteorological Society, 344-348.

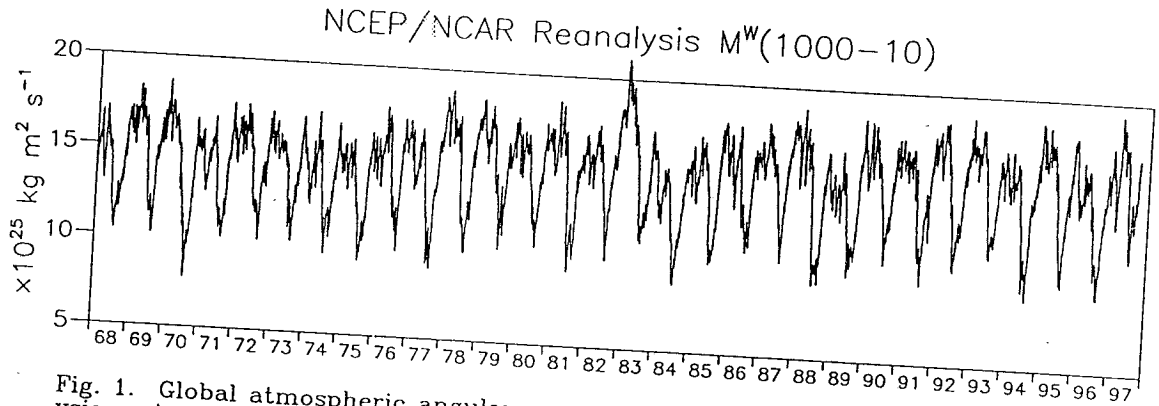

Fig. 1. Global atmospheric angular momentum (AAM) from the NCEP/NCAR reanalysis system between 10 and 1000 hPa, plotted once daily.

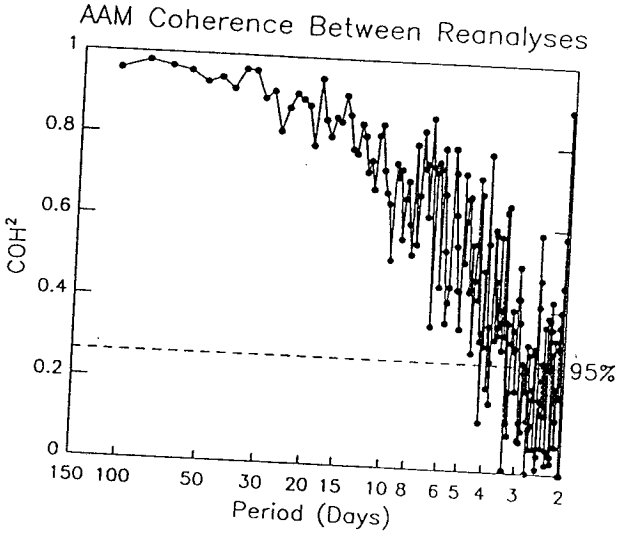

Fig. 2. Coherence between AAM values from the NCEP/NCAR and GEOS-1 DAS reanalyses during their fifteen-year overlap period, and the estimated 95% level of significance.

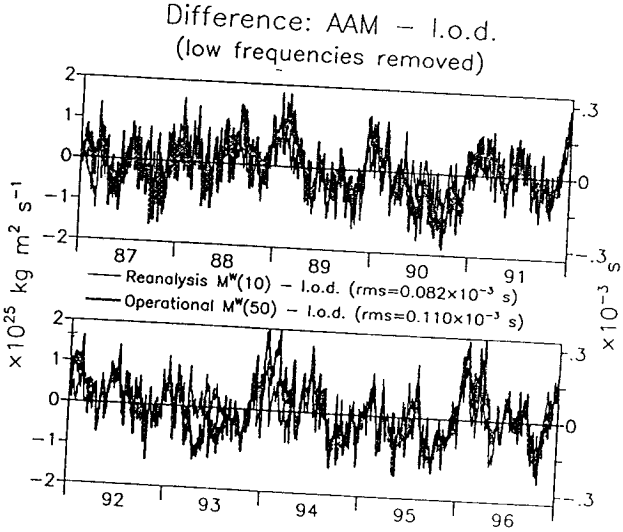

Fig. 3. The differences of length of day from both the reanalysis-based and operationally-based AAM, given in both AAM units and equivalent l.o.d. units.

Invited Presentation

Reprinted from the preprint volume of the ***7th Conference on Climate Variations,*** *2-7 February 1997, LongBeach, California, by the AMS, Boston, Massachusetts*

12.1

GLOBAL MOMENTUM AND ENERGY SIGNALS FROM REANALYSIS SYSTEMS

David A. Salstein and Richard D. Rosen
Atmospheric and Environmental Research, Inc., Cambridge, Massachusetts

1. INTRODUCTION

Lengthy analyses of the state of the atmosphere are becoming available in which observations from a variety of sources over the years have been combined to produce relatively homogeneous atmospheric fields. One such set of "reanalyses," prepared by the National Centers for Environmental Prediction/National Center for Atmospheric Research (NCEP/NCAR), is intended to span about 40 years of records (Kalnay et al. 1996). Another set, developed mostly to assimilate upcoming space-based data anticipated during the era of the Earth Observing System (EOS), is produced using the NASA Goddard Data Assimilation System (Schubert et al. 1993). Reanalyses of the atmosphere from the NCEP/NCAR system now span more than 17 years, and that of GEOS-1 DAS over 8 years.

Earlier operational analyses were produced by a succession of systems, each representing the state-of-the-art extant in its own era, and so introduce heterogeneities into time series derived from them. Other important improvements that the reanalysis systems incorporate are: (i) production of 4-times daily data (versus twice daily) and (ii) inclusion of vertical levels through much of the upper stratosphere (to 10 hPa for NCEP/NCAR and about 20 hPa for GEOS-1 DAS), as opposed to the 50 hPa level for earlier operational analyses.

Here we examine a number of global and regional statistics related to atmospheric angular momentum (AAM) and energetics. Our goal is to document the behavior of these indices as captured by the reanalyses, as a prelude to understanding aspects of the mechanisms of large-scale atmospheric behavior and variability. Another goal is to compare results obtained from the reanalyses with those based on operational products.

Corresponding author address: David A. Salstein, AER, Inc., 840 Memorial Drive, Cambridge, MA 02139; e-mail <salstein@aer.com>.

2. ATMOSPHERIC ANGULAR MOMENTUM

The signature of global mean AAM (Fig. 1a) includes a strong annual amplitude and interannual variability with peaks in El Niño years, the strongest peak in the reanalysis period occurring during the major 1982-83 ENSO warm event. Root-mean-square differences between the angular momentum of the atmosphere and that of the solid Earth, determined from geodetic measurements of the length of day, are typically small (e.g., Rosen and Salstein 1983), as would be expected from the conservation of angular momentum in the Earth-atmosphere system. These differences (Fig. 1b) are about 30 per cent lower when AAM values from NCEP/NCAR reanalysis are used than differences based on the operational AAM values. This result, based on information from totally independent measurements of Earth rotation, leads us to conclude that a significant improvement has taken place in the quality of the reanalysis fields, as compared with the operational product. Conversely, the availability of historically consistent reanalyzed values of AAM and related parameters is important for assessing global geodetic properties (Salstein et al. 1993).

Global values of the two reanalyses are themselves very close, with an r.m.s. difference (after means have been removed) of 3×10^{24} kg m^2 s^{-1}, equivalent to 0.05×10^{-3} s in l.o.d. units, during the 8-year period that both reanalysis sets overlap. A coherence analysis between the two sets shows significant agreement on variations of around 3 days and longer, with loss of coherence only at the very shortest time scales in this global quantity (Fig. 2).

When global AAM signals are separated regionally into latitude zones, they typically yield tropical easterly and middle latitude westerly momentum values (Rosen and Salstein 1983), as illustrated in Fig. 3a for the first six months of 1987. Note that the difference between reanalysis and operational

angular momentum fields (Fig. 3b) reveals that reanalyses contain generally enhanced easterlies in the tropics with dampened westerlies in the southern subtropics during the March peak associated with El Niño .

The elevation of the upper level to 10 hPa in the NCEP/NCAR reanalyses allows us to study the character of stratospheric angular momentum during nearly two decades. In this regard, Fig. 4 shows the impact of the stratospheric quasi-biennial oscillation (QBO) on the interannual variability of global momentum above 100 hPa, as suggested earlier by Chao (1989) and others. The stratosphere also contains a strong global semiannual signature, which may be interpreted as a combination of annual signals in the two hemispheres that peak in different seasons.

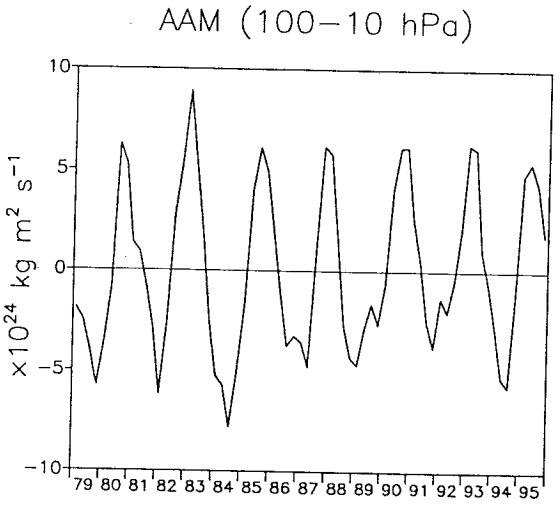

Fig. 4. Stratospheric AAM anomalies from the mean annual cycle between 10 and 100 hPa based on the NCEP/NCAR reanalysis.

3. ENERGETICS AND DIABATIC HEATING

The availability of the reanalysis fields, along with fields produced by the forecast model at the core of the reanalysis system, enables one to diagnose the complete energy cycle of the atmosphere. In this framework (e.g. Peixoto and Oort 1992), the atmosphere can be viewed as a heat engine, producing kinetic energy from the portion of potential energy due to differential heating that is available for conversion. In earlier studies we focused on monthly energy parameters to examine signals of the energy cycle from an analysis system and how these might be used to assess the quality of that system (e.g. Salstein et al. 1987). Here we assess their mean state and variability from the 8-year set of GEOS-1 DAS based energetics values.

Kinetic and available potential energies in their zonal mean and eddy forms have strong annual signatures in both hemispheres, all peaking in each hemisphere's respective winter season. Time series of energy anomalies from the annual cycle during 1985-93 (Fig. 5) reveal a marked decrease in potential and kinetic energies from the El Niño warm event year of 1987 to the La Niña phase of cold Pacific sea surface temperatures in 1988-89. Potential energy, in particular, remains anomalously low after that period.

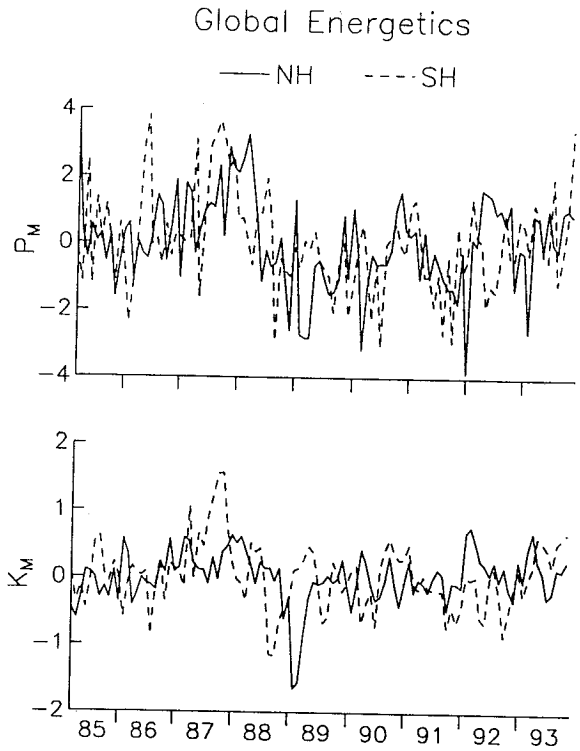

Fig. 5. Anomalies from the mean annual cycle of zonal mean available potential (P_M) and kinetic (K_M) energies, based on the GEOS-1 DAS analysis in two hemispheres. Units are 10^5 J m^{-2}.

To begin examining the origin of disagreements in energy terms between the two reanalyses, we

$G(P_M)$ by latent heating tends to determine the behavior of the total, peaking in the autumn/winter of each hemisphere. The other three terms largely balance each other; here longwave radiational processes generate negative available potential energy because cooling rates are largest where the atmosphere is the warmest. On interannual time scales, series of the generation terms (not shown) contain some evidence for an ENSO signature, but this feature is less defined than was the case in Fig. 5.

Acknowledgments. The research reported here was supported under the NOAA Climate and Global Change Program through Grant NA46GP0212 and the NASA General Circulation and Modeling Program through Contract NAS 5-32861.

REFERENCES

Chao, B.F., 1989: Length-of-day variations caused by El Niño-Southern Oscillation and Quasi-biennial Oscillation. *Science*, **243**, 923-925

Kalnay E., et al., 1996: The NCEP/NCAR 40-year reanaylsis project. *Bull. Amer. Meteorol. Soc.*, 77, 437-471.

Peixoto, J.P. and A.H. Oort, 1992: *Physics of Climate*, AIP Press, New York.

Rosen, R.D., and D.A. Salstein, 1983: Variations in atmospheric angular momentum on global and regional scales and the length of day. *J. Geophys. Res.*, **88**, 5451-5470.

Salstein, D.A., R.D. Rosen, W.E. Baker, and E. Kalnay, 1987: Impact of satellite-based data on FGGE general circulation statistics. *Quart. J. Roy. Meteor. Soc.*, **113**, 255-278.

Salstein, D.A., D.M. Kann, A.J. Miller, and R.D. Rosen 1993: The Sub-bureau for Atmospheric Angular Momentum of the International Earth Rotation Service: A meteorological data center with geodetic applications. *Bull. Amer. Meteor. Soc.*, **74**, 67-80.

Schubert, S.D., R.B. Rood, and J. Pfaendtner, 1993: An assimilated dataset for Earth science applications. *Bull. Amer. Meteor. Soc.*, **74**, 2331-2342.

Atmospheric torque on the Earth and comparison with the atmospheric angular momentum variations

O. de Viron*, Ch. Bizouard**, D. Salstein†, V. Dehant*
* Royal Observatory of Belgium, Avenue Circulaire, 3
B-1180 Brussels, Belgium
** Observatoire de Paris, Avenue de l'Observatoire, 61
F-75014 Paris, France
† Atmospheric and Environmental Research Inc., Memorial Drive, 840
Cambridge, MA 02139, USA

December 12, 1997

Abstract

The purpose of this paper is to compute the atmospheric torque on the Earth including the oceans, with a particular emphasis on the equatorial components. This opens another possibility for computing accurately the atmospheric effect on Earth orientation in space, whose classical approach was focused on the budget-based analysis of the atmospheric angular momentum. The expression of the total interaction torque coming from the interaction between the atmosphere and the Earth is derived from the angular momentum balance equation. Such a torque is composed of three parts due to pressure, gravitation, and friction. Each of these torque components is evaluated numerically by a semi-analytical approach and their orders of magnitude are intercompared.

For the equatorial components, the gravitational torque and the pressure torque have amplitudes largely above that of the friction torque, with these two main torques having the same order of magnitude but opposite signs. The numerical value of the total interaction torque is shown to be close to the atmospheric angular momentum time derivative, in the time domain. The correlation between the two time series is investigated as a function of the frequency. It is shown to be very good at low frequency, and decreases slowly when frequency increases; the correlation is still significant up to 0.5 cycle per day, but the correlation coefficient reduces to 0.5 in the diurnal frequency band.

Evaluation of Tropospheric Water Vapor Simulations from the Atmospheric Model Intercomparison Project

DIAN J. GAFFEN

NOAA/Environmental Research Laboratories, Air Resources Laboratory, Silver Spring, Maryland

RICHARD D. ROSEN AND DAVID A. SALSTEIN

Atmospheric and Environmental Research, Inc., Cambridge, Massachusetts

JAMES S. BOYLE

Program for Climate Model Diagnosis and Intercomparison, Lawrence Livermore National Laboratory, Livermore, California

(Manuscript received 3 May 1996, in final form 8 November 1996)

ABSTRACT

Simulations of humidity from 28 general circulation models for the period 1979–88 from the Atmospheric Model Intercomparison Project are compared with observations from radiosondes over North America and the globe and with satellite microwave observations over the Pacific basin. The simulations of decadal mean values of precipitable water (W) integrated over each of these regions tend to be less moist than the real atmosphere in all three cases; the median model values are approximately 5% less than the observed values.

The spread among the simulations is larger over regions of high terrain, which suggests that differences in methods of resolving topographic features are important. The mean elevation of the North American continent is substantially higher in the models than is observed, which may contribute to the overall dry bias of the models over that area. The authors do not find a clear association between the mean topography of a model and its mean W simulation, however, which suggests that the bias over land is not purely a matter of orography.

The seasonal cycle of W is reasonably well simulated by the models, although over North America they have a tendency to become moister more quickly in the spring than is observed. The interannual component of the variability of W is not well captured by the models over North America. Globally, the simulated W values show a signal correlated with the Southern Oscillation index but the observations do not. This discrepancy may be related to deficiencies in the radiosonde network, which does not sample the tropical ocean regions well. Overall, the interannual variability of W, as well as its climatology and mean seasonal cycle, are better described by the median of the 28 simulations than by individual members of the ensemble.

Tests to learn whether simulated precipitable water, evaporation, and precipitation values may be related to aspects of model formulation yield few clear signals, although the authors find, for example, a tendency for the few models that predict boundary layer depth to have large values of evaporation and precipitation. Controlled experiments, in which aspects of model architecture are systematically varied within individual models, may be necessary to elucidate whether and how model characteristics influence simulations.

1. Introduction

Water vapor and the processes that control its abundance in the troposphere play a major role in the global climate system. The condensation of water vapor, for example, with its attendant release of latent heat, provides much of the energy to drive the atmosphere's circulation. Water vapor also strongly modulates the transfer of radiation within the atmosphere and so, through this process as well, influences the overall energy balance of the planet. Finally, with its great mobility and brief atmospheric residence time, water vapor is a central component of the global hydrological cycle.

Because of the importance of water vapor in the climate system, and, presumably, in climate models, a number of assessments of simulations of humidity by general circulation models (GCMs) have been performed. Rind et al. (1991) and Del Genio et al. (1994) compared satellite observations of upper-tropospheric humidity with simulations by the GISS GCM. (See Table 1 for model abbreviations.) Gaffen and Barnett (1992) compared interannual variations of specific humidity from radiosonde observations with simulations from the University of Hamburg version of the ECMWF GCM, and Chen et al. (1996) compared a more recent version of that model with satellite-derived estimates of

Corresponding author address: Dr. Dian J. Gaffen, NOAA (R/E/AR), 1315 East–West Highway, Silver Spring, MD 20910.
E-mail: Dian.Gaffen@noaa.gov

© 1997 American Meteorological Society

TABLE 1. Model abbreviations.

BMRC	Bureau of Meteorology Research Centre, Australia
CCC	Canadian Centre for Climate Research
CNRM	Centre Nationale de Recherches Météorologiques, France
COLA	Center for Ocean–Land–Atmosphere Studies
CSIRO	Commonwealth Scientific and Industrial Research Organization, Australia
CSU	Colorado State University
DERF	Dynamical Extended Range Forecasting (GFDL)
DNM	Department of Numerical Mathematics of the Russian Academy of Sciences
ECMWF	European Centre for Medium-Range Weather Forecasts
GFDL	Geophysical Fluid Dynamics Laboratory
GISS	Goddard Institute for Space Studies
GLA	Goddard Laboratory for Atmospheres
GSFC	Goddard Space Flight Center
JMA	Japan Meteorological Agency
LMD	Laboratoire de Météorologie Dynamique, France
MGO	Main Geophysical Observatory, Russia
MPI	Max-Planck-Institut für Meteorologie, Germany
MRI	Meteorological Research Institute, Japan
NCAR	National Center for Atmospheric Research
NMC	National Meteorological Center (now the National Centers for Environmental Prediction)
NRL	Naval Research Laboratory
SNG	SUNYA/NCAR Genesis model
SUNYA	State University of New York at Albany
UCLA	University of California, Los Angeles
UGAMP	Universities Global Atmospheric Modelling Programme, United Kingdom
UIUC	University of Illinois at Urbana-Champaign
UKMO	U.K. Meteorological Office
YONU	Yonsei University, Korea

precipitable water and upper-tropospheric relative humidity. Roads et al. (1992) compared the Los Alamos GCM with NMC analyses of water vapor, water vapor flux, and water vapor flux divergence. Boyle (1993) and Phillips et al. (1995) examined the effect of horizontal resolution in the ECMWF model on precipitable water, among other things. Soden and Bretherton (1994) compared the ECMWF and NCAR GCMs' precipitable water and upper-tropospheric humidity fields with operational analyses and with satellite observations. Bony and Duvel (1994) and Bony et al. (1995) used satellite observations and ECMWF analyses of precipitable water to evaluate the LMD GCM for the period of the Atmospheric Model Intercomparison Project (AMIP), and Salathé et al. (1995) compared GLA model simulations of upper-tropospheric humidity for the AMIP with satellite observations. Thompson and Pollard (1995) compared satellite-derived observations of precipitable water with simulations by the SNG model, and Roads et al. (1996) compared NMC analyses of precipitable water and moisture flux convergence with climatological fields from the NCAR GCM.

While shedding light on aspects of particular models' humidity simulations, these studies do not give a broader sense of the state of the science in the ability of GCMs to model humidity and moisture flux fields. The Atmospheric Model Intercomparison Project has provided an opportunity to compare systematically various aspects of many GCM humidity simulations with observations. Here, we compare humidity and meridional moisture flux simulations produced for the AMIP with observations to evaluate GCM simulations of both the climatology and the seasonal and interannual variability of tropospheric water vapor.

2. The Atmospheric Model Intercomparison Project

A project of the World Meteorological Organization's World Climate Research Programme, the AMIP is an international effort to evaluate the ability of atmospheric GCMs to simulate the global climate of the decade 1979–88 (Gates 1992). The 30 participating modeling groups followed a common experimental plan that involved using identical model boundary conditions of observed monthly mean sea surface temperature and sea ice, a constant concentration of atmospheric carbon dioxide (345 ppm), and a solar constant of 1365 W m^{-2}. Model output was provided for a specified set of fields in a standard format.

Twenty-five diagnostic subprojects have been examining various aspects of the simulations. This paper reports on some of the work of AMIP Diagnostic Subproject 11, entitled "Validation of Humidity, Moisture Fluxes, and Soil Moisture in GCMs." Results concerning soil moisture are reported by Robock et al. (1995). Other AMIP results related to the hydrological cycle can be found in the following studies: Lau et al. (1995) on precipitation and evaporation, Duvel et al. (1997) on the clear-sky greenhouse effect of water vapor and the distribution of water vapor over ocean regions, Weare et al. (1995) on cloudiness, and Srinivasan et al. (1995) on tropical precipitation.

This study involves several AMIP monthly mean standard output fields: gridded precipitable water W, evaporation E, precipitation P, and zonal-mean specific humidity q. We were unable to examine relative humidity simulations because gridded relative humidity fields were not required as standard output. The availability of monthly mean values directed our attention to seasonal and longer timescales. We analyzed output from 28 of the AMIP models, listed in Table 1, that passed the quality control tests made at Lawrence Livermore National Laboratory by the Program for Climate Model Diagnosis and Intercomparison, which is responsible for AMIP coordination.

Because water vapor is a short-lived atmospheric constituent with high spatial and temporal variability, its distribution is particularly difficult to measure. Therefore, a reliable global water vapor dataset for model evaluation over the AMIP decade is not available. Over land, radiosonde data are most useful, despite their known shortcomings (Elliott and Gaffen 1991; Soden and Lanzante 1996). Over ocean, where surface micro-

wave emissions are reasonably homogeneous, satellite microwave measurements are becoming suitable but are not available for all years of the AMIP decade. We used different observational datasets for three different regions, and we will present our results for each in the following three sections. We discuss first the results for North America, where our observational data are plentiful and most reliable. Then, we examine a region of the atmosphere with a different underlying surface: the Pacific Ocean. Third, we follow with a look at the global scale.

3. Precipitable water over North America

a. North American radiosonde data

Our best verification data for the AMIP period are radiosonde observations over the North American continent. We used a dense and homogeneous network of 129 stations, depicted in Fig. 1a, in Canada, the United States, and Mexico, most of which used the VIZ radiosonde (Gaffen 1993, 1996). Daily soundings for the AMIP period (1979–88) were used to create monthly means of W, the integral of specific humidity with respect to pressure, in the column from the surface to 300 hPa, at each station. [Details about the data processing can be found in Ross and Elliott (1996a,b).] Monthly values were accepted only if at least 10 days of data were available for the month.

The station monthly mean data were then interpolated onto a 4° lat × 4° long grid (Fig. 1a). Gridpoint values were computed as a simple linear, distance-weighted average of observations from all stations within a radius of 2° lat of the grid point. To ensure the representativeness of gridded climatological values for the 10-yr period, a nearby station needed to report at least 9 of the 10 possible values for each calendar month for each grid box. For this spatial resolution, the radiosonde network samples Mexico and the United States quite well; typically about 95% of the grid boxes in each zonal band have stations within the specified radius. Poleward of 50°N sampling is worse—the comparable statistic is about 75%—in part because of the sparser network but also because of missing humidity data at 300 hPa in winter.

Examination of the data for both 0000 and 1200 UTC showed that, over most of the continent, the observed climatology of precipitable water is only minimally affected by choice of observation time. The North American decadal mean W for 0000 and 1200 UTC differs by less than 1%. Only over Mexico are the 0000 and 1200 UTC monthly means noticeably different, probably because some Mexican stations did not make 0000 UTC observations during the latter years of the period. Therefore, we chose to analyze North American 1200 UTC monthly means only. The monthly means for the models, however, were based on at least four samples per simulated day.

For comparison, model W fields over continental North America were regridded to the same 4° resolution as the observations. The observed and modeled monthly means were used to create 10-yr mean values for each calendar month, and monthly and seasonal anomalies were defined as the difference between a given value and the 10-yr mean for the appropriate month or season.

b. Climatological precipitable water

Figure 1 shows the observed and simulated climatologies of W over North America, namely, observed decadal mean values (Fig. 1a) and the median of the decadal mean simulations for the 28 models (Fig. 1b). Throughout this paper, we use the median as a measure of central tendencies of the GCM simulations because it is robust (in dealing with a non-Gaussian distribution) and resistant (to outliers). Likewise, we use the interquartile range (IQR; the difference between the upper- and lower-quartile values) as a robust and resistant measure of the spread among the 28 simulations. [See Wilks (1995) for a recent discussion of these statistics.]

As expected, both the observations (Fig. 1a) and simulations (Fig. 1b) show a general decrease of W with latitude and lower W values over the high terrain of the western mountains. The differences between the median of the model simulations and the observations (Fig. 1c) are small relative to either value and are generally less than 2 mm. As indicated in Fig. 1c, the models tend to be slightly moister than observed in the central and northeastern parts of the continent, and slightly drier than observed over western North America and the southeastern United States.

1) Continental averages

To facilitate intermodel comparison, we examined the average W for the entire continent for the entire AMIP decade. The observations were averaged using the gridded data and assigning the appropriate zonal average value to any land grid boxes without data (see Fig. 1a). Spatial averages for the simulations were computed using all available continental values and the land masks appropriate to each model. Offshore island regions were excluded from the continental averages.

Figure 2 shows the observed mean North American W value of 15.2 mm (1 mm = 1 kg m^{-2}) and values for each of the 28 models. The median value from the models is 14.5 mm, 5% less than observed, and is shown in the box plot, which, following Tukey (1977), also gives the 25th and 75th percentile values (and thus the IQR) and the minimum and maximum values. The IQR of model values is 1.4 mm, about 10% of the median value; the full range is 3.6 mm.

We note that the minimum observed annual mean North American W is 14.8 mm (for 1979) and that fully half the models never achieve an annual mean value as

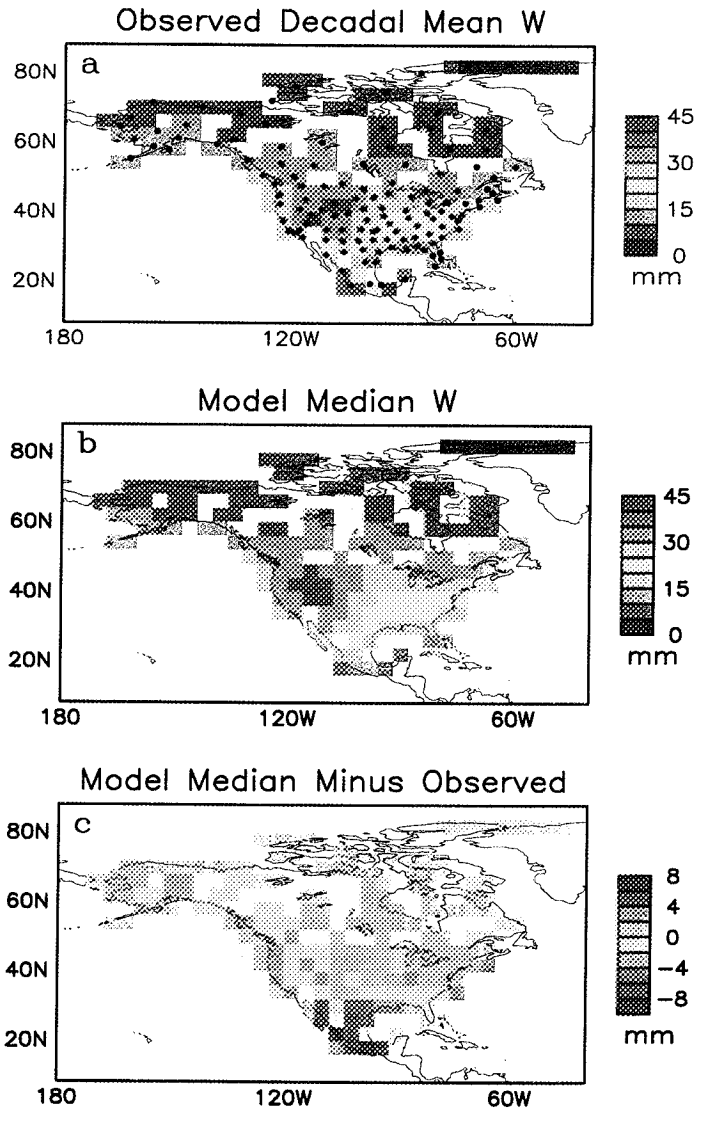

FIG. 1. (a) Decadal mean W as observed over North America and the locations of radiosonde stations for which data were used in this part of the study. (b) Median values of 28 model simulations of the decadal mean W at the locations of the observations. (c) The difference between the model median and observed fields.

large as this during any of the 10 yr of the simulations. This lack of overlap in the annual results suggests that the differences between the models and the observation are significant. By the same token, three models had all 10 annual mean values higher than the maximum observed annual mean of 15.6 mm (for 1986).

The extreme model mean values are from the SUNYA and NCAR models (Fig. 2), which represent successive generations of the Community Climate Model. This indicates that models derived from the same original code can produce highly dissimilar results.

2) TOPOGRAPHY AND PRECIPITABLE WATER

Because W is a column-integrated quantity, and because water vapor content decreases rapidly with height,

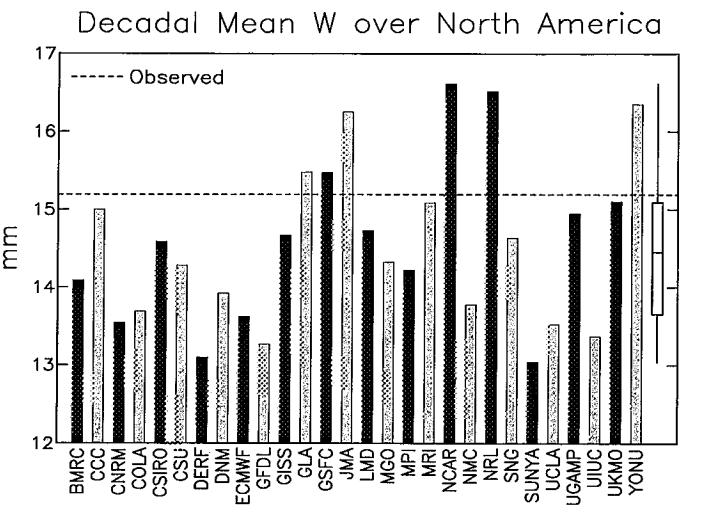

FIG. 2. Decadal mean W averaged over North America from 28 AMIP models (bars) and as observed by radiosondes (dashed line). The box plot at right gives the distribution of model values including the minimum, 25th, 50th, and 75th percentile, and maximum values.

surface topography has a strong influence on W, which may provide a possible explanation for the dry bias in many of the models. The average elevation of the North American continent, as "sampled" by the 129-station radiosonde network (Fig. 1a), is 290 m. For the 24 GCMs with available surface elevation data, the mean North American elevation ranged from 470 to 886 m, with a median value of 556 m. The discrepancy between the radiosonde network mean elevation and those of the GCMs is due, in part, to the tendency for radiosonde stations to be located in low elevation areas, and, in part, to the enhancement of orography in five of the GCMs (Phillips 1994). Thus the models are "missing" about 270 m of the planetary boundary layer, which could account for about 1 mm of precipitable water.

We cannot explain each model's individual bias, however, by invoking topographic considerations. Thus, it is not the case that the driest models have the highest mean elevations. In fact, there is no significant correlation between mean model elevation and decadal mean W over North America.

3) ZONAL AVERAGES

To summarize the models' performance as a function of latitude, we examined the zonal and decadal mean precipitable water over North America. Figure 3 shows the distribution of the models' meridional profiles of W, in zonal bands of 4° latitude in width, and the observed values. The medians are about 5% lower than the observations for much of the region between 32° and 68°N latitude, which includes most of the United States and Canada. Again, the IQRs of the model values are about 10% of the median values. As noted earlier, the observations used here are based on measurements at 1200 UTC only. Because the 1200 UTC zonal mean values

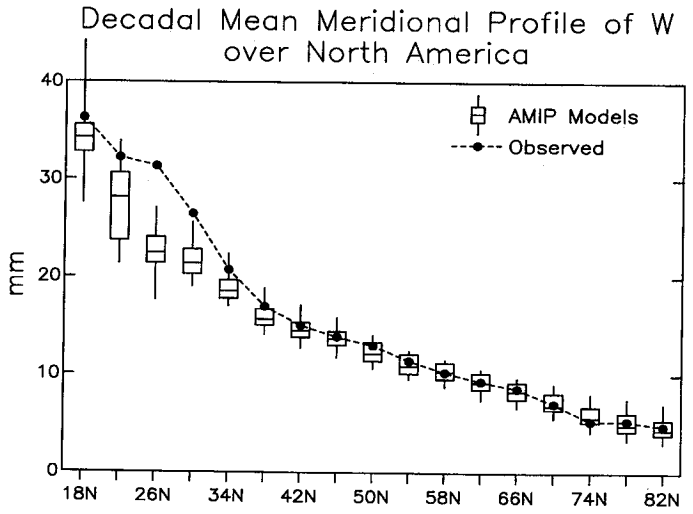

FIG. 3. Decadal and zonal mean distribution of W over North America as observed (circles) and the distribution of 28 modeled values (box plots).

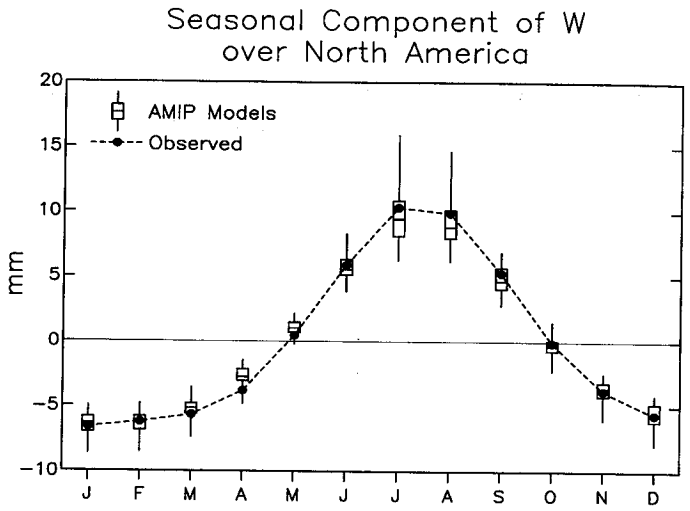

FIG. 4. Climatological seasonal component of W averaged over North America as observed (circles) and the distribution of 28 modeled values (box plots).

are, on average, about 1.5% lower than the 0000 UTC values, it is likely that the low bias we find in the models compared with the 1200 UTC data (Fig. 3) is an underestimate of the true bias.

South of 32°N, over Mexico, the models tend to be drier than is observed by as much as 28%, as anticipated by Fig. 1c. We note that the models with high horizontal resolution tend to produce lower simulated W values over Mexico than low-resolution models, perhaps because the high-resolution models better represent the high topography, while the radiosonde stations tend to be in lower elevation, coastal locations (Fig. 1a).

c. *Seasonal cycle*

Over North America the climatological seasonal cycle of precipitable water is readily apparent. The radiosonde observations indicate that summer (JJA) continental-average W reaches 23.9 mm, compared with 9.0 mm in winter (DJF). These extreme season values are not symmetric about the annual average of 15.2 mm; the summer departure from the annual average is larger than the winter departure. This asymmetry is consistent with the fairly constant relative humidity from month to month over North America (Gaffen et al. 1992b; Ross and Elliott 1996a), so that W increases roughly exponentially with temperature according to the Clausius–Clapeyron relation.

Figure 4 shows the climatological seasonal component of W over North America, defined, for each model and for the observations, by the twelve monthly mean W values for the decade minus the annual mean W for the decade, to remove biases among the latter (Fig. 2). The median values from the models are quite close to the observed, differing by no more than 1.1 mm for any given month.

A noticeable difference between the models and observations is that the models tend to become moister in spring more quickly than the atmosphere, but in the summer the models' medians are drier than observed. This tendency is consistent with a possible systematic error in GCMs' land surface parameterizations, namely, excessive evaporation in spring and insufficient evaporation in summer (P. Viterbo 1996, personal communication; Viterbo and Beljaars 1995).

Most of the models are in good agreement, but some model values are significant outliers. The IQRs and the full ranges of the model values are typically less than 1.5 and 4.5 mm, respectively, except during July and August when they are about twice as large.

One might expect model biases in W to be seasonally consistent, that is, that models that are overly dry in summer would also be biased dry in winter. Examining the seasonal model values in more detail, we note a distinct lack of association, however, between the summer and winter W values, as shown in Fig. 5. The nonparametric Spearman rank correlation coefficient (Wilks 1995) between JJA and DJF W values for the models is an insignificant -0.03. This result suggests that the model biases are not simply related to model architecture but are somehow linked to the treatment of physical processes that vary seasonally, such as convection, evaporation, and precipitation. We examine this possibility in more detail later.

The range of the seasonal cycle of W over North America, defined as the difference between the summer and winter mean climatological W values, is 14.9 mm in the radiosonde observations, as shown in Fig. 6. Model values range from 10.5 to 21.3 mm, but the median model value, 14.1 mm, is remarkably close to the observed. The observed peak of the seasonal cycle occurs in July, and the minimum is in January (Fig. 4). More than three-quarters of the models correctly simulate this measure of the phase of the seasonal cycle. The rest

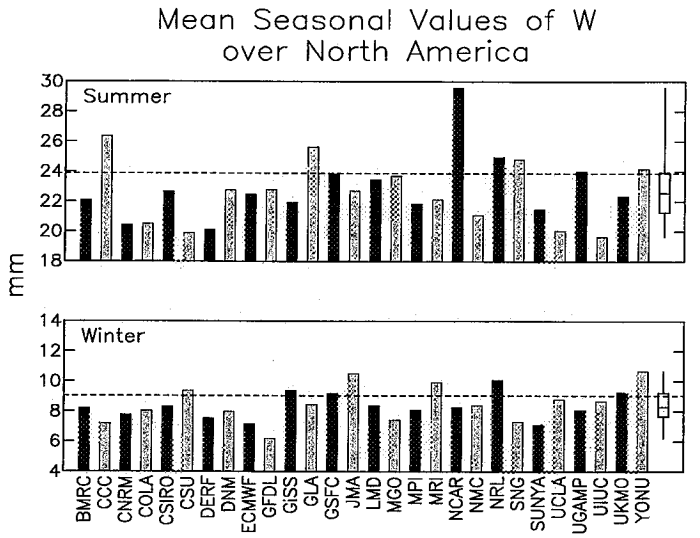

FIG. 5. Climatological summer (JJA, top) and winter (DJF, bottom) values of W over North America for each model and as observed (horizontal dashed lines). The box plots give the distribution of model values.

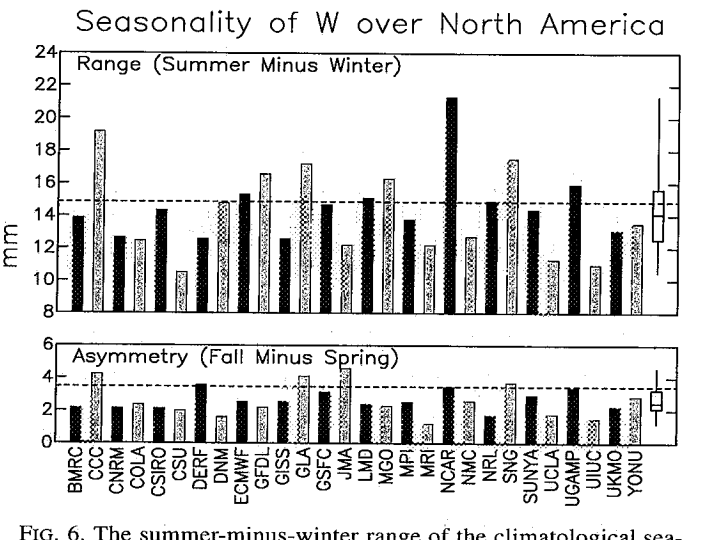

FIG. 6. The summer-minus-winter range of the climatological seasonal cycle of W over North America (top) and its fall-minus-spring asymmetry (bottom) from 28 models and as observed (horizontal dashed lines). The box plots give the distribution of model values.

have a maximum or minimum, or both, one month later than is observed, which is a small error given the closeness of the observed January and February values and of the observed July and August values (Fig. 4).

Beyond the asymmetry of the summer and winter W values from the annual average, there is an additional asymmetry in the climatological seasonal cycle related to differences between spring and fall; that is, the spring (MAM) and fall (SON) W values tend to resemble those of their preceding seasons (DJF and JJA, respectively) more than the following ones (Figs. 4 and 6). This asymmetry of atmospheric water vapor for the equinoctial seasons has been noted previously by Peixoto et al. (1981) over the Northern Hemisphere. The sense of this asymmetry is consistent with the thermal lag of the oceans in the Northern Hemisphere, but, because the North American W data show similar asymmetry, the phenomenon is not limited to ocean regions. A tendency for seasonal cyclone totals and their distribution over the continent to show a similar lag relationship was noted by Changnon et al. (1995). The radiosonde observations for North America show a 3.5-mm difference in W between fall and spring, which is about 23% of the summer minus winter range. As shown in Fig. 6, each model shows a positive difference as well, although typically the models underestimate this asymmetry by about 30%, which is consistent with the overly rapid moistening of the models in spring noted above.

d. Interannual variability of precipitable water

Although some climatic forcings of the AMIP decade, including the eruption of El Chichón in 1982, were not incorporated in the AMIP simulations, the models were forced by observed sea ice and sea surface temperatures, so there is reason to expect that they will have captured some of the interannual variability of the atmosphere during that decade. Even if all external climate forcings had been incorporated, we would not expect the models' interannual variations to match those of the atmosphere completely because interannual predictability is low outside the Tropics (e.g., Stern and Miyakoda 1995). Model simulations contain variability associated with randomness and a predictable component, which are impossible to separate in a single run. An ensemble of runs with different initial conditions is needed (e.g., Barnett 1995; Stern and Miyakoda 1995).

Nevertheless, swings in the Southern Oscillation, which are related to anomalies of sea surface temperature in the tropical Pacific, are associated with anomalous precipitation (Ropelewski and Halpert 1989) and temperature (Halpert and Ropelewski 1992) patterns over parts of the globe, including parts of North America. Because of the links between temperature, precipitation, and precipitable water, the Southern Oscillation index (SOI) and W might also be associated in some regions.

We find, however, that the observed continental mean W anomaly time series (Fig. 7) is not correlated at a statistically meaningful level with a time series of the SOI (Ropelewski and Jones 1987; extended), whether monthly, seasonal, or annual anomaly values are used. (In each case, the number of degrees of freedom used to calculate statistical significance was $n - 2$, where n is the number of elements in the 10-yr time series. This choice is based on the very low autocorrelation in the W anomaly time series, as discussed below.) As an aside, we note that when longer monthly time series (for 1973–93) of W (Ross and Elliott 1996a,b) and SOI are used, we find a significant but small negative correlation between them.

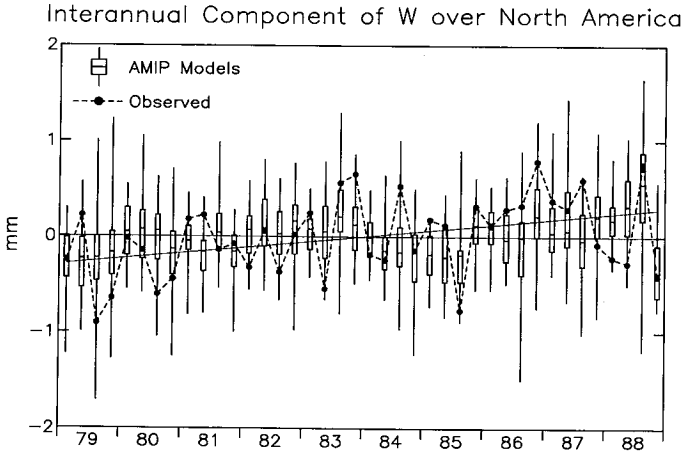

FIG. 7. Distribution of seasonal anomalies of W over North America from 28 models (box plots) and as observed (circles). The linear trend of the observed anomalies is also shown.

The observed anomaly time series is also poorly correlated with the simulated time series for the AMIP decade. As shown in Fig. 7, it is not uncommon for most individual models to have seasonal anomalies of opposite sign to the observed. For 23 of the 28 models, the correlation r between the model and observed seasonal anomaly time series is not significantly different from zero at the 95% confidence level (r exceeding about 0.31). The maximum r value is 0.48 for the UKMO model, with the time series based on the median of the 28 models obtaining the next highest r value of 0.42.

Having assessed correlations between modeled and observed monthly, annual, and individual season time series, we find that, overall, time series based on the median of the models perform considerably better than almost all models. This result indicates that a "consensus" of the models is better related to the variability in the observations than are individual models. The variance of the models' median seasonal anomaly time series is, however, only about 20% of the observed value of 0.17 mm^2, whereas all the individual model simulations have seasonal anomaly variances comparable to the observed. Such a reduction in variance is what would be expected from combining a population of 28 randomly distributed time series. These two results can be interpreted as follows: the median of the 28 model runs captures some of the predictable component of the variability of W but is missing some of the random component.

We note that the observations are marked by a trend of 0.55 mm decade^{-1} (Fig. 7), based on linear regression. This linear trend explains 15% of the total variance of the time series. [For a more thorough analysis of North American humidity trends over a longer period, see Ross and Elliott (1996a).] All but four of the models also show a positive trend in W over North America, although only 10 of the 24 positive trends are significantly different from 0, on the basis of being more than twice the standard deviation of the trend estimate. The time series based on the median anomalies has a statistically significant trend of 0.25 mm decade^{-1}.

Despite the trends, neither the observed nor the models' time series of W anomalies over North America shows substantial autocorrelation. For monthly time series, the observed lag-one autocorrelation is 0.16, which is not significant at the 95% confidence level (r exceeding about 0.19). The median lag-one autocorrelation for the models is only slightly higher: 0.30. At longer lags the autocorrelations are not significant. For the seasonal time series, the comparable lag-one autocorrelation for the observations is 0.06 and the median from the models is 0.15, neither exceeding 0.30, the 95% confidence level value.

e. Precipitable water, evaporation, and precipitation

The major source of water vapor in the troposphere is evaporation E from the surface, and its main sink is precipitation P. Although the focus of this study is water vapor, we also examined the AMIP P and E fields to see whether the differences among model W fields might be related to these other components of the hydrological cycle. Lau et al. (1995, Figs. 2 and 3) found that, globally, models with high rates of evaporation have high rates of precipitation. Because atmospheric water vapor is the link between E and P, one could hypothesize that models with high E and P also have high W.

Using rank correlation analysis, we found no significant relationships, however, between model simulations of decadal mean W over North America and either P or E fields over the continent. We also tested the association between W over North America and both P and E upstream over the North Pacific Ocean and, again, found no significant correlation. On the other hand, rank correlations between E and P are 0.75 over North America and 0.82 over the North Pacific. Thus, we find, and we infer from the results of Lau et al. (1995), that, both globally and regionally, models with high rates of evaporation tend to have high rates of precipitation. They do not, however, necessarily have high W. This result may seem counterintuitive, but we should recall that P is more directly related to relative humidity than to W, and temperature differences among models could be playing an important role in determining differences in W. Evaporation and precipitation rates are indicative of the vigor of the hydrologic cycle and, thus, the mean residence time of water vapor, not its absolute amount.

4. Humidity over the Pacific Ocean

As a counterpoint to the analysis over North America, we considered part of the Pacific basin, between 150°E and 130°W and between 60°N and 60°S, to compare the models over a homogeneous water surface. Radiosonde data are sparse over this region, but satellite-derived estimates of W from the Special Sensor Microwave/

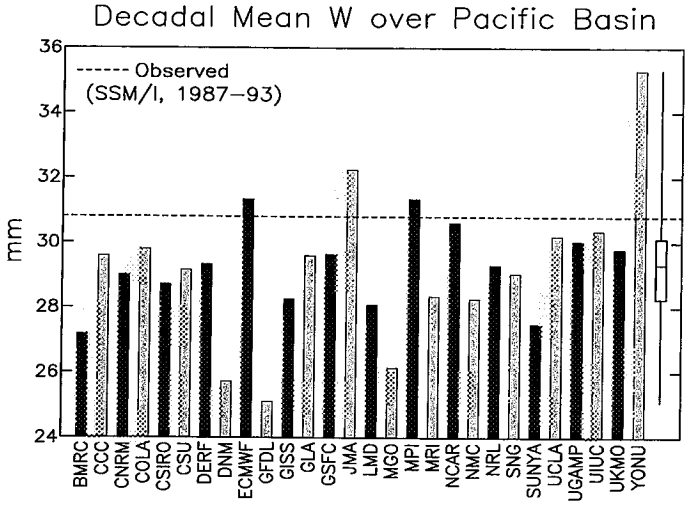

FIG. 8. Decadal mean W over the Pacific basin (60°N to 60°S, 150°E to 130°W) for each model (bars) and the distribution of the model values (box plot). The horizontal dashed line indicates the observed value for the period 1987–93 from SSM/I data.

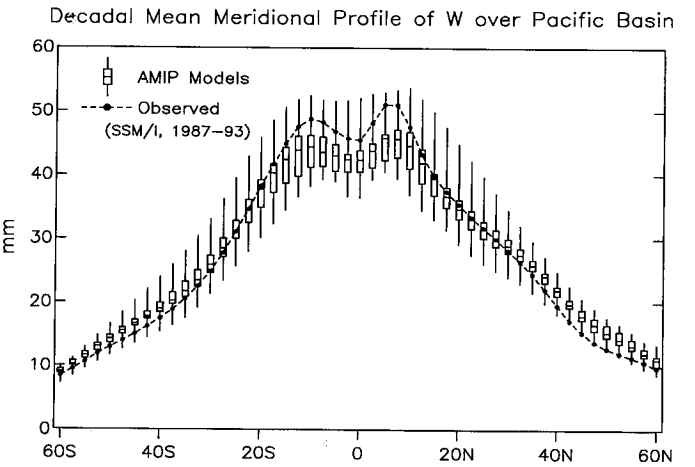

FIG. 9. Meridional profile of W over the Pacific basin as observed (circles) and modeled (box plots).

Imager (SSM/I) instrument for the period 1987–93 (Alishouse et al. 1990) provide a useful alternate estimate of the climatological W fields. Because there are only 2 yr of overlap between the SSM/I data period and the AMIP decade, we limit our discussion to the climatological fields.

Figure 8 shows the Pacific basin average, decadal mean W from each of the 28 models and as estimated from the SSM/I data. The observed and model median W values are 30.8 and 29.3 mm, respectively, a difference of 5%. For the models, the ratio of the IQR to the median is 6%, which, although smaller than the 10% value found over North America, is still notable, suggesting that the specification of sea surface temperature is not sufficient to produce identical oceanic W fields. We should not expect that W in models be a strict function of local sea surface temperatures because other variables, such as tropospheric temperature, lapse rate, and relative humidity, which are related to large-scale dynamics, influence oceanic W (Gaffen et al. 1992a; Bony and Duvel 1994). The reduced spread among the models over the sea compared with the continent might be due to model differences in resolving topography, as we discuss in the next section.

The zonal mean values of W, shown in Fig. 9, reveal that the underestimates of W over the Pacific basin are the result of underestimates between 20°S and 20°N, where the median model values are up to 10% smaller than the SSM/I observations. It is likely, moreover, that the SSM/I W retrievals used here are biased low. Jackson and Stephens (1995) found that the Alishouse et al. (1990) SSM/I W values are larger than colocated radiosonde-derived values at midlatitudes but smaller than the radiosonde values in the Tropics. The SSM/I data we are using have been adjusted to remedy this bias partially (Colton and Poe 1994), but a low bias in the Tropics probably remains (R. Ferraro 1995, personal communication). An additional bias of unknown magnitude is related to the difference between the period of the SSM/I data record (1987–93) and the AMIP decade (1979–88). Duvel et al. (1997) made a direct comparison of W from 10 AMIP models with satellite data for the period 1985–88, and they also found a dry bias in the Tropics. Thus, we conclude that the models are substantially drier than the real atmosphere over the tropical Pacific basin; however, unlike over North America, we cannot point to orography differences between models and observations as a factor contributing to the bias.

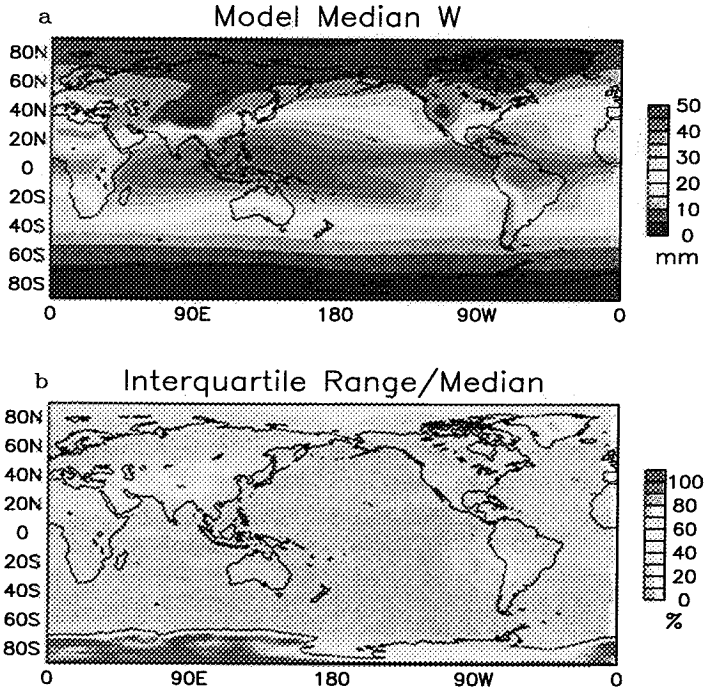

FIG. 10. (a) Median values and (b) the ratio of the interquartile range to the median of 28 model simulations of the decadal mean W over the globe.

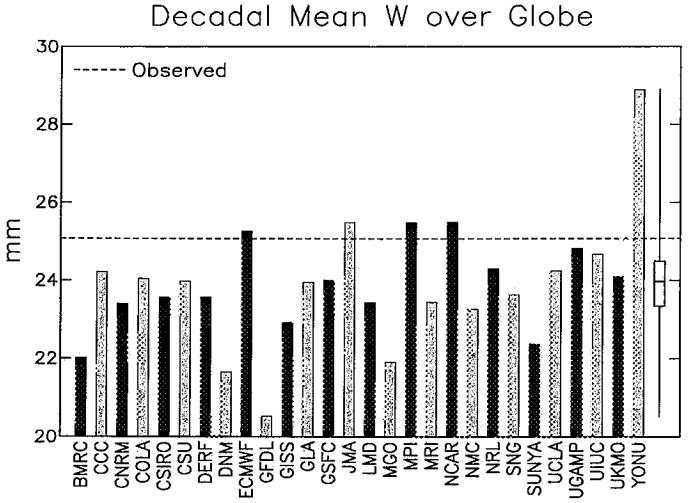

FIG. 11. Globally integrated decadal-mean W for each model (bars) and the distribution of the model values (box plot). The horizontal dashed line indicates the value observed for the same decade based on analyses of radiosonde observations by Oort (1983).

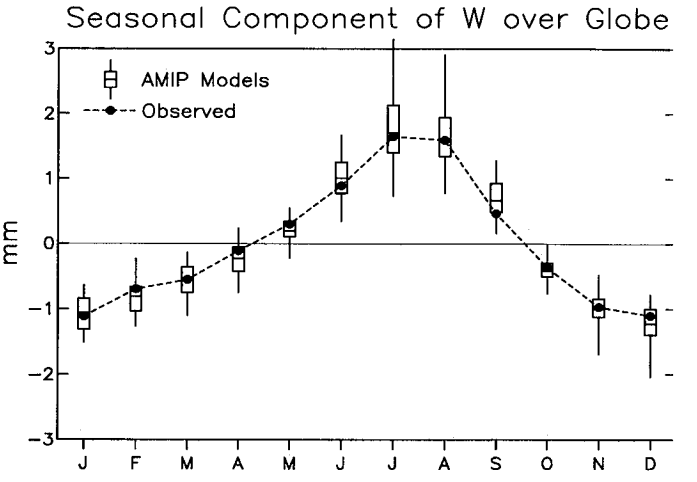

FIG. 12. Climatological seasonal component of globally integrate W as observed (circles) and the distribution of model values (bo plots).

5. Global precipitable water and meridional moisture flux

Broadening our coverage to the global scale, Fig. 10a depicts the median of the 28 AMIP models' simulations of W over the globe. The expected features of the global W climatology are evident, including the general decrease of W from the equator poleward, low W values over high terrain and known desert regions, and maximum W over the tropical Pacific warm pool.

The global map of the ratio of the IQR to the median (Fig. 10b) shows that this measure of the intermodel variability of the W simulations is between 10% and 20% over most of the world's oceans and over low elevation continental regions. Over high terrain, the ratio is generally between 40% and 80%. It appears, therefore, that the variation in how models resolve topographic features is the main source of disparity among model simulations of climatological W fields. The exceptionally large ratios, exceeding 100%, over Antarctica are also related to very low W values there (Fig. 10a).

The global- and decadal-mean values of W for each of 28 AMIP models and their distribution are shown in Fig. 11. For comparison, we also present the global- and decadal-mean W computed using gridded analyses of the 0000 and 1200 UTC radiosonde observations during 1979–88 produced by Oort (1983) and Oort and Liu (1993). Monthly mean fields of q on a 2.5° × 5° latitude–longitude grid at individual pressure levels have been integrated between the surface and 300 hPa to produce global W maps, from which global averages were calculated.

Although these analyses suffer from well-known problems associated with the irregular distribution of radiosonde stations across the globe, they nevertheless represent the most comprehensive and homogeneous source of upper-air global circulation statistics currentl available for the AMIP period. Those analyses of W based on fields from analysis-forecast systems are prob lematic because such analyses can depend considerabl on the architecture of a particular system, which, more over, typically changes with time (Trenberth and Guil lemot 1995). Atmospheric reanalyses, which are begin ning to become available (e.g., Kalnay et al. 1996), ma be useful for future studies, although differences amon reanalyses from different modeling centers will have t be reconciled.

Evident in Fig. 11 is a tendency for the model at mospheres to be drier than observed over the globe, a found over North America and the tropical Pacifi Ocean. We note, however, that estimates of the tota precipitable water over the globe, $\{W\}$, vary consid erably, although the value reported here based on th Oort analyses (25.1 mm) lies well within the range o other observations, as summarized by Wittmeyer an Vonder Haar (1994). In any case, the model median $\{W$ is some 4.4% (1.1 mm) smaller than the observed value and nearly one-fifth of the model values are more tha 10% smaller than observed.

The IQR is 4.8% of the median model value, whic is smaller than the comparable statistics over Nort America or the Pacific basin. On the other hand, th IQR is comparable to the amount by which $\{W\}$ woul increase during two decades of global warming, assum ing a warming of 0.7 K and no appreciable changes i relative humidity (Del Genio 1993). The current dis crepancy among GCMs in simulating $\{W\}$ for the AMI decade is, therefore, of consequence for interpretin GCM predictions of climate change.

Despite such difficulties in reproducing the decadal mean $\{W\}$, it is reassuring to discover (Fig. 12) that th models can produce reasonable seasonal variations i $\{W\}$, as they were observed to do over North Americ (Fig. 4). The global seasonal cycle has the signature o

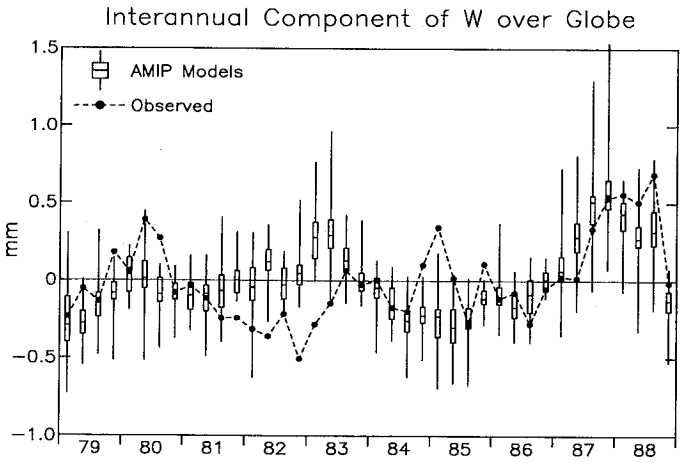

FIG. 13. Distribution of seasonal anomalies of globally integrated W from 28 models (box plots) and as observed (circles).

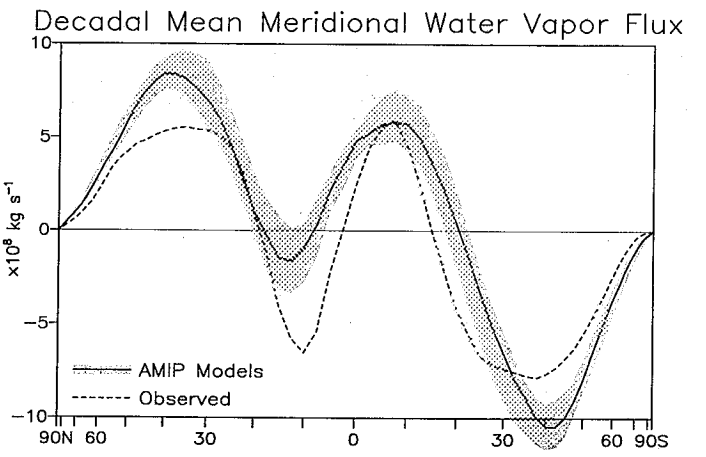

FIG. 14. The median (solid line) of the 28 model profiles of the total meridional flux of water vapor, $2\pi a \cos(\phi)\,[Q_\phi]$ (where a is the earth's radius and ϕ is latitude), as inferred from water vapor budget considerations. The shaded area indicates the interquartile range of model values. Positive values indicate northward fluxes. The observed value is also shown (dashed line).

the Northern Hemisphere where W peaks in summer. The tendency for a larger range of model values during northern summer deserves further investigation.

Interannual variations in the models' $\{W\}$ values (Fig. 13) are marked by an ENSO signal. The correlation between the median of the models' seasonal $\{W\}$ anomaly time series and seasonal values of the SOI (Ropelewski and Jones 1987; extended) is -0.42, significant at the 99% confidence level. The extension to a domain beyond North America here appears to incorporate the influence of warm sea surface temperatures in the eastern tropical Pacific on modeled $\{W\}$. The reality of this signal is difficult to confirm with the available observations, although Jackson and Stephens (1995) find an El Niño–Southern Oscillation signal in W integrated over the global oceans from SSM/I measurements during July 1987–June 1991. On the other hand, Sun and Oort (1995) and Soden and Lanzante (1996) note problems in capturing this signal properly with the radiosonde network alone because of the poor data coverage in the eastern Pacific. Perhaps as a result the correspondence between the observed and model median curves in Fig. 13 is less than ideal ($r = 0.47$), and the correlation ($r = 0.17$) between the observations and SOI values is not significant.

Because it is important to the global energy and water cycle, we consider briefly the large-scale flux of moisture over the globe. Figure 14 shows profiles of the net meridional transport of water vapor for the AMIP decade. The model profiles have been deduced from the archived AMIP standard output of evaporation, precipitation, and W; however, the observed profile of this transport has been determined directly from Oort's analyses of meridional vapor fluxes through evaluating the relationship $[Q_\Phi] = \int [qv]\, dp$ (where v is the meridional wind component, p is pressure from the surface to 300 hPa, and the square brackets denote zonal mean values). The figure reveals a clear tendency for the models to overestimate systematically the poleward flux of moisture (and latent heat) over much of the globe, although uncertainties in the observations are potentially large and need to be taken into account. Interestingly, Gleckler et al. (1995) find that the AMIP models also tend to overestimate the poleward total atmospheric energy transport; the results in Fig. 14 suggest that as much as 50% or more of this bias may be accounted for by excessive moisture fluxes.

6. Potential sources of model differences

To determine the possible reasons for the spread among the model simulations of precipitable water (and other hydrological variables), we measured the association between several aspects of the models' formulations, as summarized by Phillips (1994), and their simulations of decadal mean W, P, and E over North America and the Pacific basin and of global W. We also considered possible associations between model formulations and the net meridional moisture flux but in a much more limited fashion.

The 14 facets of model formulation considered are given in the top row of Table 2. Two of these are the models' horizontal and vertical resolution, and, as numerical quantities, they were rank correlated with the hydrological variables tested, which are summarized in the first column of Table 2.

The remaining 12 variables are dichotomous. For example, a model either does or does not contain prescribed soil moisture fields. For the characteristics described by dichotomous variables, the table shows the number of models with that characteristic. We note that only in the case of soil moisture schemes does the number of models in the three categories sum to 28. The two model characteristics associated with the planetary boundary layer are independent, as are the two asso-

TABLE 2. Relationships between aspects of GCM formulation and the tendencies in simulated precipitable water (W) and evaporation (E) and precipitation (P) rates. Statistically significant relationships are indicated according to whether the model characteristic is associated with higher or lower values of the variable in question, otherwise a dash appears. (Note that in the case of Northern Hemisphere moisture flux, only relationships with model spatial resolution were tested.)

	Spatial resolution		Planetary boundary layer		Numerics		Convective scheme				Soil moisture scheme			Reevaporation of precipitation
	Vertical	Horizontal	Prognostic PBL depth	Vertical diffusion above PBL	Finite difference	Moisture filling	Moist convective adjustment	Interactive cumulus subensembles	Moisture convergence closure	Bulk mass flux	Bucket	Prescribed	Vegetation	
Number of models	—	—	3	21	10	20	5	8	7	5	20	4	4	17
North America W	—	—	—	—	—	—	—	—	—	—	low	high	—	—
Pacific basin W	—	—	—	—	—	low	—	—	—	—	—	—	—	—
Global W	—	—	—	—	—	low	—	—	—	—	—	—	—	—
North America E	—	—	high	low	—	—	—	high	—	—	—	high	—	—
North America P	—	low	high	—	—	—	—	—	low	—	—	—	—	—
Pacific basin E	—	—	high	—	—	—	—	—	—	—	—	—	—	—
Pacific basin P	—	—	high	—	—	—	—	—	—	—	—	—	—	—
Northern Hemisphere moisture flux	—	—												

ciated with numerics. The convective schemes include the possibility of hybrid approaches (for which a model would fall into more than one category) but do not include all approaches used in the AMIP models.

We used the Student's t test to determine whether the group of models with a given characteristic have mean values of simulated hydrologic variables that are significantly different from the mean of the remaining models. The results of these tests are summarized in Table 2. If a t test shows the difference in the means to be significant at the 95% confidence level or better, or if the rank correlation is significant at that level, the table shows whether the model characteristic is associated with higher or lower values of the variable in question.

We stress that finding an explanation for the relationships revealed is not straightforward and may be impossible because of the complexity of the GCMs. Determining the effects of different model characteristics by comparing various GCMs may be impossible. Controlled experiments in which characteristics are changed one at a time may be needed to determine the sensitivity of a particular model to particular aspects of its construction.

Furthermore, the model properties we examined are interrelated. For example, models using convective schemes with interactive cumulus subensembles are often offsprings of the UCLA model and so share other traits as well. Thus, the models are not independent in a statistical sense, and a relationship among them might have nothing to do with the convective scheme but another aspect(s) of their construction.

a. *Vertical and horizontal resolution*

Model vertical resolution, measured as the total number of vertical levels, shows no significant correlation with any of the variables tested. Models with high horizontal resolution have low P over North America. We find little association between model horizontal resolution (as measured by the total number of grid points globally) and W except, as noted before, that high resolution models simulate lower W over Mexico than low resolution models. As noted above, we suspect that differences in model horizontal resolution account for the high intermodel variability noted in regions of high terrain (Fig. 10b).

Our result differs from those of Phillips et al. (1995) and Williamson et al. (1995), who found tendencies for total precipitable water in the ECMWF and NCAR models, respectively, to decrease with increasing horizontal resolution, although for the ECMWF model the effect was most pronounced in the Tropics and was not monotonic. Our result that the peak northward flux of moisture in the Northern Hemisphere is insensitive to horizontal resolution differs from that of Manabe et al. (1991), who report that this flux decreased with increasing horizontal resolution in their version of the GFDL model.

b. *Planetary boundary layer formulation*

In three of the models, the depth of the planetary boundary layer is a prognostic variable, rather than a fixed value. Because the boundary layer contains a large fraction of the total column W and because mixing of water vapor from the boundary layer to the free troposphere is limited by atmospheric stability, we would expect that the depth of the boundary layer will have a strong influence on W. The models with prognostic boundary layers tend to have high E and high P over both North America and the Pacific basin but there is no significant association with W. The use of schemes

to allow the vertical diffusion of moisture above the planetary boundary layer in 21 of the models is associated with low North American E values but with no other tendencies in the simulated moisture variables shown in Table 2.

c. Numerical approaches

The application of finite-difference numerical schemes or spectral methods to solve the governing equations has no particular impact on the variables examined. The use of moisture filling techniques to eliminate spurious negative values of humidity is associated with low W values over the Pacific basin and globally.

d. Method of parameterizing convection

To examine the relationship between the parameterization of atmospheric convection and simulated hydrological variables, we considered four broad categories of models. We caution that some models use hybrid approaches so that a model might fall into more than one category. In addition, the parameterization of atmospheric convection is a complex matter, and because each approach is sensitive to the details of implementation (e.g., Bony et al. 1995) and to other related GCM parameterizations, categorizing models in this way is an oversimplification.

Five of the 28 models employ moist convective adjustment schemes (e.g., Manabe et al. 1965), and the t tests show no significant differences between this group and the remaining 23 models. Eight models employ convective schemes with interactive cumulus subensembles (e.g., Arakawa and Schubert 1974), and they tend to have high E over North America.

Seven models parameterize convection based on moisture convergence closure (e.g., Kuo 1974), and they are associated with low P over North America. The use of bulk mass flux schemes (e.g., Tiedtke 1989) in five models has no significant association with the simulated W, E, or P examined. Direct comparison of the models using bulk mass flux and moisture convergence closure schemes showed no significant differences. This finding differs from the results of Colman and McAvaney (1995) who found that a mass flux convective scheme produced a moister troposphere in the BMRC model than did a moisture convergence convective scheme.

e. Soil moisture

Following the classification developed by Robock et al. (1995) for the treatment of soil moisture in the AMIP GCMs, we tested the association between W and use of 1) "bucket" models in 20 GCMs, 2) prescribed soil moisture in four GCMs, and 3) soil moisture schemes involving vegetation models in four GCMs.

Bucket models tend to be associated with low W over North America, and models with prescribed soil moisture tend to have high North American W and E values. The models incorporating vegetation show no particular tendencies with respect to W, E, or P.

f. Evaporation from falling precipitation

Seventeen models allow for the reevaporation of moisture from falling precipitation, which one might expect to enhance tropospheric water vapor. Our analysis shows no significant differences, however, between these 17 models and the remaining 11.

g. Can we explain model differences?

The most striking aspect of Table 2 is the large fraction of cells that are blank; the number of filled cells is not large, although it is higher than what would be expected by chance. The useful information in Table 2 is where there are consistent tendencies in different hydrological variables, such as is seen with prognostic PBL depth. Nevertheless, overall, and in agreement with the results of Weare et al. (1995), who studied AMIP total cloudiness simulations, the statistical results presented here do not point to obvious connections between specific aspects of model architecture and simulated hydrological variables.

7. Conclusions

Comparisons of observations and 28 AMIP simulations of tropospheric water vapor show the following.

1) The models tend to underestimate the decadal mean precipitable water by approximately 5% over North America and globally as compared with radiosonde observations, and over the Pacific basin as compared with satellite SSM/I observations.
2) The largest disparity among models' decadal mean W fields occurs over regions of high terrain, probably because of differences in resolving topography. Over North America, the relatively high elevation in the models compared to the radiosonde network is a partial explanation for the dry bias of the models as a group. There is no significant correlation, however, between the individual models' mean elevation and their mean W values, and topography is clearly not the source of the dry bias over the Pacific basin.
3) The mean seasonal cycles of precipitable water are reasonably well simulated but with a wide range among models.
4) The models do not capture much of the observed interannual variability in precipitable water. Overall, a consensus of the models, as defined by the median of the 28 models considered, gives a better simulation of the observed interannual variability than do individual models.
5) The models appear to overestimate the poleward flux of moisture, which probably contributes to the gen-

eral overestimate of atmospheric poleward energy flux found by other investigators.

6) There is little association between aspects of model formulation and simulated hydrological variables. A more fruitful approach would probably involve controlled experiments with individual GCMs, in which one aspect of the model is changed systematically and the impact on the simulations is assessed. Such an approach is currently under consideration as part of a successor to AMIP, AMIP II, which could also involve multiple simulations from each participating model to extract the predicted interannual signal from random noise and would better specify the boundary conditions and forcing functions for the period of simulation.

Acknowledgments. We are especially grateful to the AMIP modeling groups and the Program for Climate Model Diagnosis and Intercomparison at Lawrence Livermore National Laboratory for making the simulations available for this project. We thank Rebecca Ross of NOAA for preparing the North American radiosonde dataset used in this study and Peter Nelson of AER, Inc., for dealing with the global-scale datasets and for preparing the figures. We also thank William Elliott, Sharon LeDuc, Peter Stone, Peter Rowntree, Pedro Viterbo, and two anonymous reviewers for their helpful comments. The work at AER, Inc., was partially supported by the Climate Dynamics Program of the National Science Foundation under Grant ATM-9223164 and by the U.S. Department of Energy's National Institute for Global Environmental Change, through the NIGEC Northeast Regional Center at Harvard University (DOE Cooperative Agreement DE-FC03-90ER61010).

REFERENCES

Alishouse, J. C., S. A. Snyder, J. Vongasthorn, and R. R. Ferraro, 1990: Determination of oceanic precipitable water from the SSM/I. *IEEE Trans. Geosci. Remote Sens.,* **28,** 811–816.

Arakawa, A., and W. H. Schubert, 1974: Interaction of a cumulus cloud ensemble with the large-scale environment. Part I. *J. Atmos. Sci.,* **31,** 674–701.

Barnett, T. P., 1995: Monte Carlo climate forecasting. *J. Climate,* **8,** 1005–1022.

Bony, S., and J.-P. Duvel, 1994: Influence of the vertical structure of the atmosphere on the seasonal variation of precipitable water and greenhouse effect. *J. Geophys. Res.,* **99,** 12 963–12 980.

——, ——, and H. Le Treut, 1995: Observed dependence of the water vapor and clear-sky greenhouse effect on sea surface temperature: Comparison with climate warming experiments. *Climate Dyn.,* **11,** 307–320.

Boyle, J., 1993: Sensitivity of dynamical quantities to horizontal resolution for a climate simulation using the ECMWF (cycle 33) model. *J. Climate,* **6,** 796–815.

Changnon, D., J. J. Noel, and L. H. Maze, 1995: Determining cyclone frequencies using equal-area circles. *Mon. Wea. Rev.,* **123,** 2285–2294.

Chen, C.-T., E. Roeckner, and B. J. Soden, 1996: A comparison of satellite observations and model simulations of column-integrated moisture and upper-tropospheric humidity. *J. Climate,* **9,** 1561–1585.

Colman, R. A., and B. J. McAvaney, 1995: Sensitivity of the climate response of an atmospheric general circulation model to changes in convective parameterization and horizontal resolution. *J. Geophys. Res.,* **100,** 3155–3172.

Colton, R. A., and G. A. Poe, 1994: Shared Processing Program, Defense Meteorological Satellite Program, Special Sensor Microwave/Imager Algorithm Symposium, 8–10 June 1993. *Bull. Amer. Meteor. Soc.,* **75,** 1663–1669.

Del Genio, A., 1993: Accuracy requirements. Long-term monitoring of global climate forcings and feedbacks. NASA Conf. Publ. 3234, 91 pp. [Available from NASA Center for Aerospace Information, 800 Elkridge Landing Road, Linthicum Heights, MD 21090-2934.]

——, W. Kovari Jr., and M-S. Yao, 1994: Climatic implications of the seasonal variation of upper tropospheric water vapor. *Geophys. Res. Lett.,* **21,** 2701–2704.

Duvel, J.-P., S. Bony, and H. LeTreut, 1997: Clear-sky greenhouse effect sensitivity to sea surface temperature changes: An evaluation of AMIP simulations. *Climate Dyn.,* in press.

Elliott, W. P., and D. J. Gaffen, 1991: On the utility of radiosonde humidity archives for climate studies. *Bull. Amer. Meteor. Soc.,* **72,** 1507–1520.

Gaffen, D. J., 1993: Historical changes in radiosonde instruments and practices. WMO/TD-No. 541, Instruments and Observing Methods Rep. 50, 123 pp. [Available from World Meteorological Organization, P.O. Box 2300, CH-1211 Geneva, Switzerland.]

——, 1996: A digitized metadata set of global upper-air station histories. NOAA Tech. Memo. ERL ARL-211, 38 pp. [Available from National Technical Information Service, 5285 Port Royal Road, Springfield, VA 22061.]

——, and T. P. Barnett, 1992: A comparison of observations and model simulation of tropospheric water vapor. *J. Geophys. Res.,* **97,** 2775–2780.

——, W. P. Elliott, and A. Robock, 1992a: Relationships between tropospheric water vapor and surface temperature as observed by radiosondes. *Geophys. Res. Lett.,* **19,** 1839–1842.

——, A. Robock, and W. P. Elliott, 1992b: Annual cycles of tropospheric water vapor. *J. Geophys. Res.,* **97,** 18 185–18 193.

Gates, W. L., 1992: AMIP: The Atmospheric Model Intercomparison Project. *Bull. Amer. Meteor. Soc.,* **73,** 1962–1970.

Gleckler, P. J., and Coauthors, 1995: Cloud-radiative effects on implied oceanic energy transports as simulated by atmospheric general circulation models. *Geophys. Res. Lett.,* **22,** 791–794.

Halpert, M. S., and C. F. Ropelewski, 1992: Surface temperature patterns associated with the Southern Oscillation. *J. Climate,* **5,** 594–614.

Jackson, D. L., and G. L. Stephens, 1995: A study of SSM/I-derived columnar water vapor over the oceans. *J. Climate,* **8,** 2025–2038.

Kalnay, E., and Coauthors, 1996: The NCEP/NCAR 40-year reanalysis project. *Bull. Amer. Meteor. Soc.,* **77,** 437–471.

Kuo, H. L., 1974: Further studies of the parameterization of the influence of cumulus convection on large-scale flow. *J. Atmos. Sci.,* **31,** 1232–1240.

Lau, W. K.-M., Y. C. Sud, and J.-H. Kim, 1995: Intercomparison of hydrologic processes in global climate models. NASA Tech. Memo. 104617, 170 pp. [Available from NASA Center for Aerospace Information, 800 Elkridge Landing Road, Linthicum Heights, MD 21090-2934.]

Manabe, S., J. Smagorinsky, and R. F. Strickler, 1965: Simulated climatology of a general circulation model with a hydrologic cycle. *Mon. Wea. Rev.,* **93,** 769–798.

——, R. J. Stouffer, M. J. Spelman, and K. Bryan, 1991: Transient responses of a coupled ocean–atmosphere model to gradual changes of atmospheric CO_2. Part I: Annual mean response. *J. Climate,* **4,** 785–818.

Oort, A. H., 1983: Global Atmospheric Circulation Statistics, 1958–1973. NOAA Prof. Paper 14, 180 pp. and 47 microfiche. [Avail-

able from National Technical Information Service, 5285 Port Royal Road, Springfield, VA 22161.]

——, and H. Liu, 1993: Upper-air temperature trends over the globe, 1958–1989. *J. Climate,* **6,** 292–307.

Peixoto, J. P., D. A. Salstein, and R. D. Rosen, 1981: Intra-annual variation in large-scale moisture fields. *J. Geophys. Res.,* **86,** 1255–1264.

Phillips, T. J., 1994: A summary documentation of the AMIP models. PCMDI Rep. 18, UCRL-ID-116384, 343 pp. [Available from National Technical Information Service, U.S. Dept. of Commerce, 5285 Port Royal Rd., Springfield, VA 22161.]

——, L. C. Corsetti, and S. L. Grotch, 1995: The impact of horizontal resolution on moist processes in the ECMWF model. *Climate Dyn.,* **11,** 85–102.

Rind, D., E.-W. Chiou, W. Chu, J. Larsen, S. Oltmans, J. Lerner, M. P. McCormick, and L. McMaster, 1991: Positive water vapor feedback in climate models confirmed by satellite data. *Nature,* **349,** 500–503.

Roads, J. O., S.-C. Chen, J. Kao, D. Langley, and G. Glatzmaier, 1992: Global aspects of the Los Alamos general circulation model hydrological cycle. *J. Geophys. Res.,* **97,** 10 051–10 068.

——, S. Marshall, R. Oglesby, and S.-C. Chen, 1996: Sensitivity of the CCM1 hydrological cycle to CO_2. *J. Geophys. Res.,* **101,** 7321–7339.

Robock, A., C. A. Schlosser, K. Ya. Vinnikov, S. Liu, and N. Speranskaya, 1995: Validation of humidity, moisture fluxes, and soil moisture in GCMs: Report of AMIP diagnostic subproject 11: Part 1-Soil Moisture. *Proc. First AMIP Scientific Conference,* Monterey, CA, World Meteorological Organization, 85–90.

Ropelewski, C. F., and P. D. Jones, 1987: An extension of the Tahiti–Darwin Southern Oscillation index. *Mon. Wea. Rev.,* **115,** 2161–2165.

——, and M. S. Halpert, 1989: Precipitation patterns associated with the high index phase of the Southern Oscillation. *J. Climate,* **2,** 268–284.

Ross, R. J., and W. P. Elliott, 1996a: Tropospheric water vapor climatology trends over North America: 1973–93. *J. Climate,* **9,** 3561–3574.

——, and ——, 1996b: Tropospheric precipitable water: A radiosonde-based climatology. NOAA Tech. Memo. ERL ARL-219, 132 pp. [Available from National Technical Information Service, 5285 Port Royal Road, Springfield, VA 22061.]

Salathé, E. P., Jr., D. Chesters, and Y. C. Sud, 1995: Evaluation of the upper-tropospheric moisture climatology in a general circulation model using TOVS radiance observations. *J. Climate,* **8,** 2404–2414.

Soden, B. J., and F. P. Bretherton, 1994: Evaluation of water vapor distribution in general circulation models using satellite observations. *J. Geophys. Res.,* **99,** 1187–1210.

——, and J. R. Lanzante, 1996: Satellite and radiosonde climatologies of upper tropospheric water vapor. *J. Climate,* **9,** 1235–1250.

Srinivasan, G., M. Hulme, and C. G. Jones, 1995: An evaluation of the spatial and interannual variability of tropical precipitation as simulated by GCMs. *Geophys. Res. Lett.,* **22,** 2139–2142.

Stern, W., and K. Miyakoda, 1995: Feasibility of seasonal forecasts inferred from multiple GCM simulations. *J. Climate,* **8,** 1071–1085.

Sun, D.-Z., and A. H. Oort, 1995: Humidity–temperature relationships in the tropical troposphere. *J. Climate,* **8,** 1974–1987.

Thompson, S. L., and D. Pollard, 1995: A global climate model (GENESIS) with a land-surface transfer scheme (LSX). Part I: Present climate simulation. *J. Climate,* **8,** 732–761.

Tiedtke, M., 1989: A comprehensive mass flux scheme for cumulus parameterization in large-scale models. *Mon. Wea. Rev.,* **117,** 1779–1800.

Trenberth, K. E., and C. J. Guillemot, 1995: Evaluation of the global atmospheric moisture budget as seen from the analyses. *J. Climate,* **8,** 2255–2772.

Tukey, J. W., 1977: *Exploratory Data Analysis.* Addison-Wesley, 688 pp.

Viterbo, P., and A. C. M. Beljaars, 1995: An improved land surface parameterization in the ECMWF model and its validation. *J. Climate,* **8,** 2716–2748.

Weare, B. C., and Coauthors, 1995: Evaluation of total cloudiness and its variability in the Atmospheric Model Intercomparison Project. *J. Climate,* **8,** 2224–2238.

Wilks, D. S., 1995: *Statistical Methods in the Atmospheric Sciences.* Academic Press, 467 pp.

Williamson, D. L., J. T. Kiehl, and J. J. Hack, 1995: Climate sensitivity of the NCAR Community Climate Model (CCM2) to horizontal resolution. *Climate Dyn.,* **11,** 377–397.

Wittmeyer, I. L., and T. H. Vonder Haar, 1994: Analysis of the global ISCCP TOVS water vapor climatology. *J. Climate,* **7,** 325–333.

JOURNAL OF GEOPHYSICAL RESEARCH, VOL. 102, NO. D14, PAGES 16,423–16,438, JULY 27, 1997

Atmospheric angular momentum fluctuations during 1979-1988 simulated by global circulation models

R. Hide,[1] J. O. Dickey, and S. L. Marcus
Space Geodetic Science and Applications Group, Jet Propulsion Laboratory, California Institute of Technology, Pasadena

R. D. Rosen and D. A. Salstein
Atmospheric and Environmental Research, Inc., Cambridge, Massachusetts

Abstract. Changes in major global dynamical phenomena in the Earth's atmosphere are manifested in the time series of atmospheric angular momentum (AAM), as determined directly from meteorological observations and indirectly from geodetic observations of small fluctuations in the rotation of the solid Earth which are proportional to length of day. AAM fluctuations are intimately linked with energetic processes throughout the whole atmosphere and also with the stresses at the Earth's surface produced largely by turbulent momentum transport in the oceanic and continental boundary layers and by the action of normal pressure forces on orographic features. A stringent test of any numerical global circulation model (GCM) is therefore provided by a quantitative assessment of its ability to represent AAM fluctuations on all relevant timescales, ranging from months to several years. From monthly data provided by the Atmospheric Model Intercomparison Project (AMIP) of the World Climate Research Programme, we have investigated seasonal and interannual fluctuations and the decadal mean in the axial component of AAM in 23 AMIP GCMs over the period 1979-1988. The decadal means are generally well simulated, with the model median value (1.58×10^{26} kg m^2 s^{-1}) being only 3.5% larger than the observed mean and with 10 of the models being within 5% of the observed. The seasonal cycle is well reproduced, with the median amplitude of the models' seasonal standard deviations being only 2.4% larger than observed. Half the seasonal amplitudes lie within 15% of the observed, and the median correlation found between the observed and model seasonal cycles is 0.95. The dominant seasonal error is an underestimation of AAM during northern hemisphere winter associated with errors in the position of subtropical jets. Less robust are the modeled interannual variations, although the median correlation of 0.61 between model simulations and observed AAM is statistically significant. The two El Niño-Southern Oscillation events that occurred during the AMIP decade 1979-1988 have the expected positive AAM anomalies, although the AAM signature of the 1982-1983 event tends to be underestimated and that of the 1986-1987 event overestimated.

1. Introduction

Atmospheric winds are driven by buoyancy forces due to the action of gravity on density inhomogeneities produced and maintained by differential solar heating. Their large-scale patterns are strongly influenced by Coriolis forces associated with the Earth's comparatively rapid rotation. In accordance with the thermal wind equation, the westerly component of atmospheric flow increases in strength with height above the Earth's surface at a rate proportional to the latitudinal temperature gradient. Because the equatorial regions of the lower reaches of the highly compressible atmosphere are warmer than the polar regions, the troposphere and overlying stratosphere, which contain more than 99% of the total mass of the atmosphere, "superrotate" [see *Hide*, 1986] on average at about 7 ms^{-1} relative to the underlying planet. If the angular momentum associated with this average relative superrotation of the tropospere and stratosphere were transferred to the much more massive solid Earth, the length of the day (LOD) would decrease by about 4 parts in 100 million, roughly 3 ms.

Geodetic observations going back several decades reveal irregular LOD fluctuations of up to about 1 ms on interannual, seasonal, and intraseasonal timescales (see Figure 1), and detailed studies using modern meteorological and geodetic data have established that these fluctuations are largely of meteorological origin (for reviews, see *Hide and Dickey* [1991], *Rosen* [1993], *Dickey* [1993], *Eubanks* [1993] and references therein). Fluctuations in the equatorial components of atmospheric angular momentum (see Appendix) are associated with nonaxisymmetric features of the global atmospheric circulation and make a substantial contribution to polar motion (the observed wobble of the rotation axis of the solid Earth with respect to geographical coordinates) on subdecadal timescales. On decadal and longer timescales, the dominant forcing of Earth rotation is due to nonmeteorological agencies, including angular momentum exchange between Earth's liquid metallic core and the overlying solid mantle and "spin-orbit" coupling between Earth and Moon largely as-

[1]Also at Department of Physics (Atmospheric, Oceanic and Planetary Physics), University of Oxford, Clarendon Laboratory, Oxford.

Copyright 1997 by the American Geophysical Union.

Paper number 97JD00699.
0148-0227/97/97JD-00699$09.00

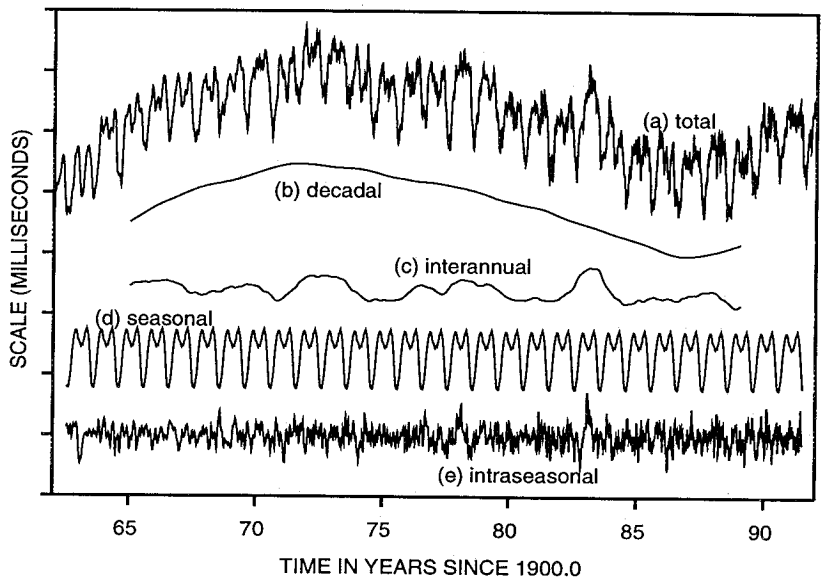

Figure 1. Time series of irregular fluctuations in the length of the day (LOD) from 1963 to 1992 (curve a) and its decadal, interannual, seasonal, and intraseasonal components (curves b, c, d, and e, respectively). The decadal (curve b) component largely reflects angular momentum exchange between the solid Earth and the underlying liquid metallic outer core produced by torques acting at the core-mantle boundary. The other components (curves c, d, and e) largely reflect angular momentum exchange between the atmosphere and the solid Earth, produced by torques (proportional to the time derivative of the LOD time series) acting directly on the solid Earth over continental regions of the Earth's surface and indirectly over oceanic regions (adapted from *Hide and Dickey* [1991]).

sociated with tidal friction in the oceans. The angular momentum of the oceans is not well determined owing to the paucity of data; however, fluctuations in magnitude in its axial component are no more than 10% of those of the axial component of atmospheric angular momentum (AAM) with which this paper is concerned.

The task of improving the performance of numerical models of the atmosphere by identifying and correcting weaknesses in their formulation requires systematic methods for testing model performance. The inclusion of diagnostics based on analyses and forecasts of AAM offers several advantages. The most obvious is the unique opportunity it provides, in principle at least, for comparing on a clear-cut physical basis the output of a global quantity from the models with observations that are completely independent of meteorological data, namely, those of short-term fluctuations in the LOD [see, e.g., *Bell et al.*, 1991]. The axial torques at the Earth's surface responsible for meteorologically induced fluctuations in the Earth's rotation are produced by (1) tangential stresses in turbulent boundary layers and (2) normal (pressure) stresses acting on irregular topography. These stresses are transmitted directly to the solid Earth over continental regions and indirectly over the oceans.

Second, considerations of AAM fluctuations bear directly on fundamental aspects of the energetics of the global atmospheric circulation and cannot be separated from them. In the absence of energy sources, the atmosphere would rotate with the solid Earth like a rigid body (i.e., no winds), for this would be a state of minimum kinetic energy of the whole system for a given total angular momentum. Differential solar heating produces atmospheric winds, the kinetic energy of which derives from the available potential energy of the atmosphere (associated with gravity acting on the density field maintained by the heating) through the action of vertical motions. Angular momentum is thereby redistributed without any change occurring in the total amount in the whole system (since solar heating produces no net torque) but with an increase in the total kinetic energy. A substantial contribution to this energy is associated with "superrotation" of the atmosphere at the average azimuthal wind speed U of about 7 ms^{-1}, namely $1/2MU^2$ if M is the total mass of the atmosphere. Observed fluctuations in AAM amount to a considerable fraction of the mean $MU\overline{R}$ in magnitude (where $\overline{R}$ is the mean radius of the solid Earth). Concomitant fluctuations in the kinetic energy associated with the superrotation amount to a considerable fraction of the mean $1/2MU^2$. By energy conservation arguments, these can only be produced by dynamical processes involving nonlinear interactions between the zonal wind field, the nonzonal wind field, and the field of available potential energy in the atmosphere. Successful models of the global circulation of the atmosphere must of course represent these interactions correctly. (For further details, see *Bell et al.* [1991].)

Thanks to the First GARP Global Experiment (FGGE) of the Global Atmospheric Research Programme (GARP) it became possible to obtain useful daily determinations of the total AAM for comparison with geodetic data on LOD variations [*Hide et al.*, 1980]. Manifold subsequent developments following this early work include practical arrangements for producing and disseminating routine daily or more frequent determinations not only of the axial component of the AAM vector but also of the equatorial components [*Barnes et al.*, 1983; *Salstein et al.*, 1993]. These determinations (see Appendix, equations A7 to A9) are now made from analysis (and in some cases also from forecast) fields by several meteorological centers, namely, the European Centre for Medium-Range Weather Forecasts (ECMWF), Japan Meteorological Agency (JMA), United Kingdom Meteorological Office (UKMO), and U.S. National Meteorological Center (NMC) (recently renamed National Centers for Environmental Prediction, NCEP). Plans are now in hand at some centers for producing routine determinations of surface torques, which will supplement the AAM data and facilitate diagnostic studies.

The ambitious Atmospheric Model Intercomparison Project (AMIP) of the World Climate Research Programme (WCRP) is one of the main activities initiated by the WCRP's Working Group on Numerical Experimentation in its efforts to refine atmospheric models and improve their ability to produce useful forecasts of changes in weather and climate [*Gates*, 1992; *Phillips*, 1994]. Thirty atmospheric modeling groups cooperate unselfishly in AMIP, together with more than 20 groups engaged in diagnostics subprojects of AMIP concerned with the thorough testing of models by means of quantitative intercomparisons of their ability to reproduce various aspects of the behavior of the atmosphere.

In the experiment analyzed here, the models performed simulations of the decade January 1979 to December 1988 using uniform, monthly data sets of observed sea surface temperature (SST) and sea ice extent as surface boundary conditions, along with specified values of the solar constant (1365 W m^{-2}) and carbon dioxide concentration (345 ppm) [*Phillips*, 1994]. Because the models were not updated with observed atmospheric conditions during the integration, they are not expected to simulate synoptic-scale variations in detail. However, intercomparisons of the models' seasonal-to-interannual response to observed SST forcing, along with their decadal mean (climatological) fields, can yield considerable insight into their ability to realistically simulate climatic processes on these longer timescales. Our efforts in the atmospheric angular momentum diagnostics subproject of AMIP bear directly on the extent to which zonal winds and the exchange of angular momentum between the atmosphere and the underlying planet are represented correctly by the models being tested.

Specific dynamical phenomena produce strong signatures in observed AAM fluctuations, and the study of the angular momentum balance of the Earth-atmosphere-ocean system is relevant to many climate dynamics issues. Earth rotation variations provide a unique and truly global measure of changes in the atmosphere, oceans, and cryosphere, on timescales ranging from days to centuries. The variation of AAM has now been convincingly linked to subdecadal changes in the length-of-day down to timescales of about a week [*Dickey et al.*, 1992a]. The axial component of the total AAM shows a characteristic seasonal variation and pronounced "broadband" intraseasonal fluctuations (Figure 1, curves d and e). Oscillations on intraseasonal timescales, including those related to the Madden-Julian oscillation, have been shown to involve AAM changes propagating within the tropics [*Anderson and Rosen*, 1983], with contributions from orographically forced oscillations in the extratropics [*Dickey et al.*, 1991; *Marcus et al.*, 1994, 1996]. The accurate characterization of the seasonal AAM cycle [*Rosen et al.*, 1991b] involves the correct simulation of the varying atmospheric temperature gradient between the tropics and extratropics, which controls the strength and positioning of the subtropical jet streams.

LOD and AAM also exhibit interannual variations, on quasi-biennial and longer timescales [*Chao*, 1984, 1988, 1989; *Dickey et al.*, 1992b, 1994; *Eubanks et al.*, 1986; *Jordi et al.*, 1994; *Rosen et al.*, 1984; *Salstein and Rosen,* 1986] (see Figure 1, curve c). Well correlated with El Niño-Southern Oscillation (ENSO) events, these are associated with large-scale zonal wind anomalies which appear to propagate from tropical to extratropical regions. Teleconnections between different latitude bands have been discovered in AAM data on these timescales, providing insights into the global structure of interannual climate variations [*Dickey et al.*, 1992b; *Marcus and Dickey*, 1994; *Black et al.*, 1996; *Mo et al.*, 1997]. Indeed, much progress has been made during the past 20 years with the investigation of AAM fluctuations on subdecadal timescales. Important new results can be expected from future studies, including numerical simulations of AAM fluctuations on decadal and longer timescales [*Rosen and Salstein*, 1996]. Such studies, in addition to their intrinsic interest in meteorology and oceanography, will indirectly facilitate investigations of angular momentum exchange between the Earth's liquid metallic outer core and overlying mantle and other nonmeteorological processes which, though evidently relatively unimportant on subdecadal timescales in the excitation of irregular fluctuations in the Earth's rotation, play dominant roles on longer timescales.

The data used and methodology employed in our study are outlined in section 2, setting the scene for the axial AAM intercomparisons of decadal means and on seasonal and interannual timescales, presented and summarized in sections 3 and 4. In future work it will be important to investigate the extent to which atmospheric models can reproduce fluctuations in the equatorial components of atmospheric angular momentum. These excite measurable movements in the Earth's pole of rotation on subdecadal timescales, including a Chandlerian free wobble with a period of 14 months (see Appendix).

2. Data and Methodology

2.1. Observed Values of Angular Momentum

The most complete series of AAM and zonal wind fields generally available for the AMIP decade (1979-1988) are those produced operationally by the NMC. Comparisons of the NMC AAM series with one from the ECMWF [*Rosen et al.*, 1987; *Rosen,* 1993; *Dickey et al.*, 1993] indicate that the differences between the two series are so small that we can confidently use either for validating the AMIP model results. Up to twice-daily values of zonal mean zonal wind $[u]$ from the NMC have been archived on a 2.5° latitude grid at standard pressure levels between 1000 and 50 mbar. We created monthly mean fields of $[u]$ by averaging all data available within each calendar month during 1979-1988. These fields were then used to create a monthly series of the relative angular momentum (M^w) of the atmosphere about the polar axis by applying equation (A13) and evaluating

$$M^w = 2\pi\bar{R}^3 g^{-1} \int_{50}^{1000} \int_{-\pi/2}^{\pi/2} [u]\cos^2\phi \, d\phi \, dp. \tag{1}$$

In addition to the global M^w values, we also computed the relative angular momentum of the atmosphere in each of 46 equal-area belts ($m_b{}^w$) over the globe to help isolate regional sources of model errors in M^w. As explained by *Rosen and Salstein* [1983], the number of belts is dictated by the 2.5° latitude resolution of the NMC analyses and the constraint that all belts should have the same area as that between the equator and 2.5°N. The latitudinal boundaries of the resulting 46 belts are listed by *Rosen and Salstein* [1983]. Within each belt, $m_b{}^w$ is given by

$$m_b{}^w = 2\pi\bar{R}^3 g^{-1} \int_b \int_{50}^{1000} [u]\cos^2\phi \, d\phi \, dp, \tag{2}$$

where ϕ runs between the southern and northern boundaries of belt b. In evaluating this expression numerically, care was taken to ensure that $\sum_{46\text{belts}} m_b^w = M^w$ is satisfied each month. Although the creation of $m_b{}^w$ values precludes consideration of variability within a vertical column, the results of *Rosen and Salstein* [1983] suggest that such variability is often more coherent than that in the

Table 1. List of AMIP Models Intercompared in This Study Together With an Indication of Their Performance

	Model Affiliation	Decadal Mean	Seasonal σ_S	Interannual σ_I
BMRC	Bureau of Meteorology Research Centre (Australia)	√	√	√
CCC	Canadian Centre for Climate Research	√	√	√
CNRM	Centre National de Recherches Météorologiques (France)	–	√	√
CSIRO	Commonwealth Scientific and Industrial Research Organization (Australia)	√	√	–
DERF	Dynamical Extended-Range Forecasting (at GFDL)	√	√	+
DNM	Department of Numerical Mathematics (of the Russian Academy of Sciences)	–	+	–
ECMWF	European Centre for Medium-Range Weather Forecasts	√	–	√
GFDL	Geophysical Fluid Dynamics Laboratory	√	+	√
GLA	Goddard Laboratory for Atmospheres, NASA	√	√	√
GSFC	Goddard Space Flight Center, NASA	√	√	–
JMA	Japan Meteorological Agency	√	+	√
MGO	Main Geophysical Observatory, Russia	√	+	√
MPI	Max-Planck-Institut für Meteorologie, Germany	√	–	+
MRI	Meteorological Research Institute, Japan	√	√	–
NCAR	National Center for Atmospheric Research	+	+	–
NMC	National Meteorological Center (now NCEP)	–	–	√
NRL	Naval Research Laboratory, Monterey	√	–	+
RPN	Recherche en Prévision Numérique, Canada	√	–	–
SNG	State University of New York at Albany/NCAR	√	+	–
SUNYA	State University of New York at Albany	√	√	–
UCLA	University of California at Los Angeles	+	–	–
UGAMP	The United Kingdom Universities' Global Atmospheric Modelling Programme	√	√	√
UKMO	United Kingdom Meteorological Office	√	+	+

Check indicates that the model gives a value within 15% of that observed; minus sign, a value more than 15% lower than observed; and plus sign, more than 15% higher.

meridional direction. To maintain a manageably sized regional dataset, therefore, we feel it sufficient to limit the bulk of our intraglobal analyses here to $m_b{}^w$.

2.2. Model Values of Angular Momentum

Monthly mean values of $[u]$ were available from 29 global circulation models (GCMs) at the time of writing as part of the standard output archived by AMIP [*Gates*, 1992]. All but five of the GCMs include pressure levels up to 50 mbar, and these five models were eliminated from further consideration to maintain consistency with the depth of the atmosphere in the NMC observations. (Output from Goddard Institute for Space Studies was also disregarded, because of its unusual vertical distribution.) By the same token, levels above 50 mbar that may have been available for an AMIP model are disregarded here. The model values of $[u]$ are given on two-dimensional latitude-pressure grids whose resolutions vary from model to model. To simplify computations, however, we interpolated all model output to the same 2.5° latitude grid as the NMC observations, although we retained each model's archived distribution of pressure levels when computing M^w and $m_b{}^w$.

Model results shown here are identified by the acronyms defined by *Gates* [1992], as updated by *Phillips* [1994] (see Table 1). (An exception is the SUNYA/NCAR model, which we abbreviate as SNG.) The latter report summarizes the major characteristics of each AMIP model, and no attempt to reproduce that information in any detail is made here. It is clear from this documentation, however, that the set of AMIP models is heterogeneous, embodying a wide range of choices in resolution and physical parameterizations; hence an assumption that the relatively small sample of M^w values available to us is drawn from a statistically normal population is not justified. We therefore avoid using the mean and standard deviation as measures of central tendency and spread, respectively, of the distribution of model M^w values. Instead, we use the median and the interquartile range (IQR) described by *Lanzante* [1996] for these statistics. The IQR is simply the difference defined by the upper quartile minus the lower quartile of values in the distribution; that is, it measures the distance spanned by the middle half of the distribution. An advantage of the IQR is that it is relatively resistant to the presence of large outliers, unlike the standard deviation. For a Gaussian distribution, however, the two statistics are related: in this case the IQR is 1.349 times the standard deviation [*Lanzante*, 1996].

2.3. Temporal Decomposition

Rosen et al. [1991b] and *Hide and Dickey* [1991] illustrate that the temporal variability in the Earth-atmosphere system can be usefully separated into three frequency bands: intraseasonal, seasonal, and interannual. A decomposition for LOD, which also experiences substantial decadal variability due to core-mantle interaction, is shown in Figure 1. The seasonal cycle is by far the dominant subdecadal signal, being ~1 ms in peak to peak amplitude and typically explaining more than 75% of the variance in the total series (see Figure 1, curves c, d and e). Hence our inability to consider intraseasonal variations in M^w here because of the

monthly mean resolution of the AMIP standard output is not overly limiting. To define the seasonal component of each of the modeled and observed M^w series, we first removed their decadal means, that is, the average of the 120 monthly values for 1979-1988, and then averaged the 10 values for each calendar month. An interannual component, which is considerably smaller than the seasonal signature, is formed by averaging the monthly values in each of the 40 "seasons" during the decade, beginning with January-March 1979, and subtracting from this series the decadal mean seasonal cycle. Although this "interannual" component includes some higher (nonseasonal) frequency variability, we will see that the bulk of its variance is from timescales longer than a year. Hence the term "interannual" is appropriate for this component.

In the next section, we compare the decadal mean, seasonal, and interannual components of the 23 model M^w series with the observed components obtained from the NMC analyses. As noted above, the accuracy of the NMC analyses is not a significant issue here; the differences found among the model M^w series are typically much larger than the uncertainty in the observed series.

3. Results

Time series of M^w for each of the 23 AMIP models are shown in Figure 2 (heavy solid lines) and are contrasted with M^w determined from the operational NMC analysis (light solid lines) and that inferred from geodetic data (dotted lines). The observed AAM and LOD track each other with a high degree of fidelity, although

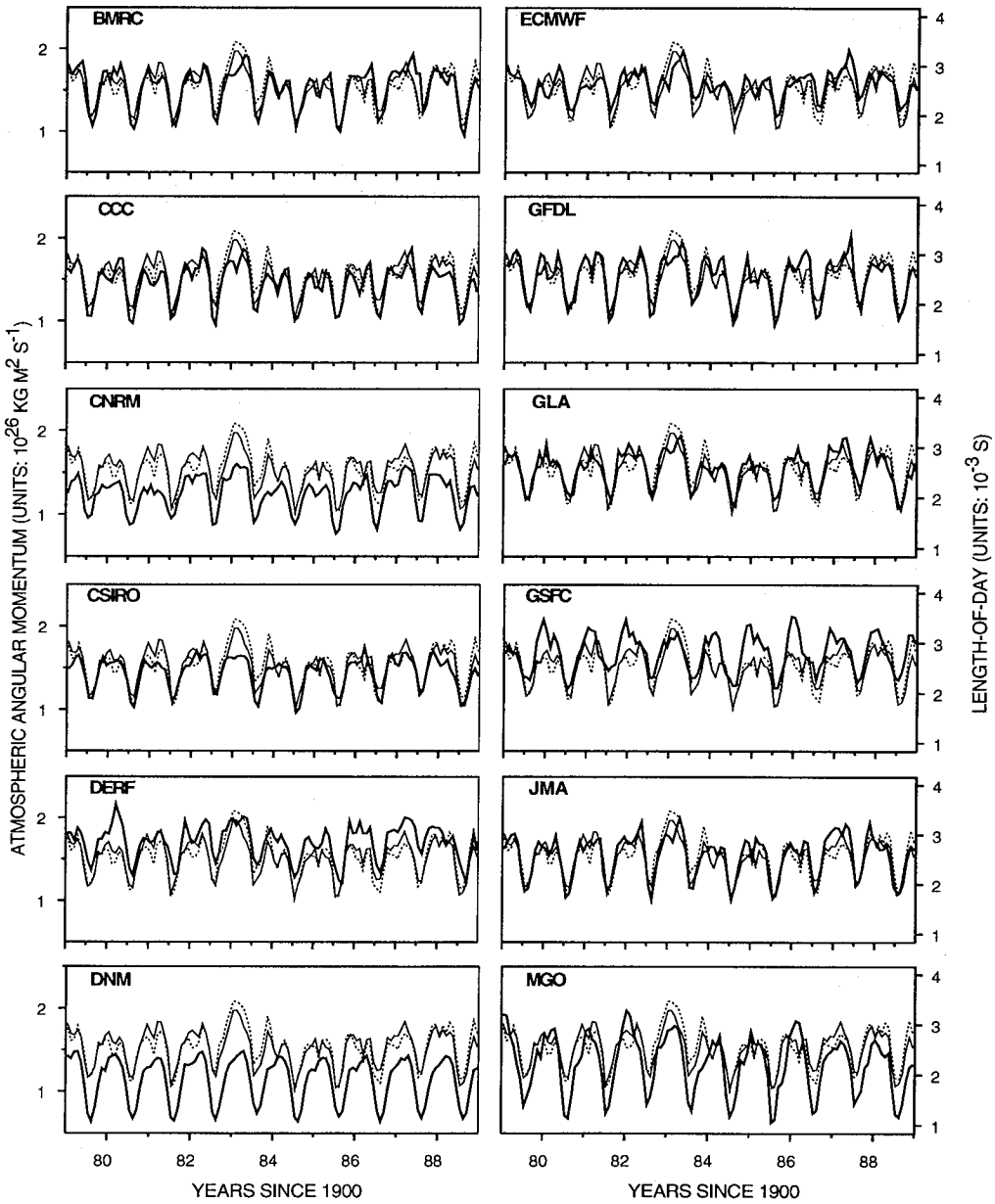

Figure 2. The axial component of atmospheric angular momentum (M^w) determined from the monthly standard output for 23 AMIP models that extend up to the 50 mbar level (heavy solid lines). The light solid and dotted lines (repeated in each panel) show M^wdetermined from the operational NMC analysis for the AMIP decade and global angular momentum fluctuations inferred from geodetic data, respectively (a quadratic offset has been removed from the geodetic LOD determinations to account for core-mantle effects). One equivalent millisecond unit (emsu) of axial angular momentum corresponds to 0.67×10^{26} kg m^2 s^{-1}. Model abbreviations are listed in Table 1.

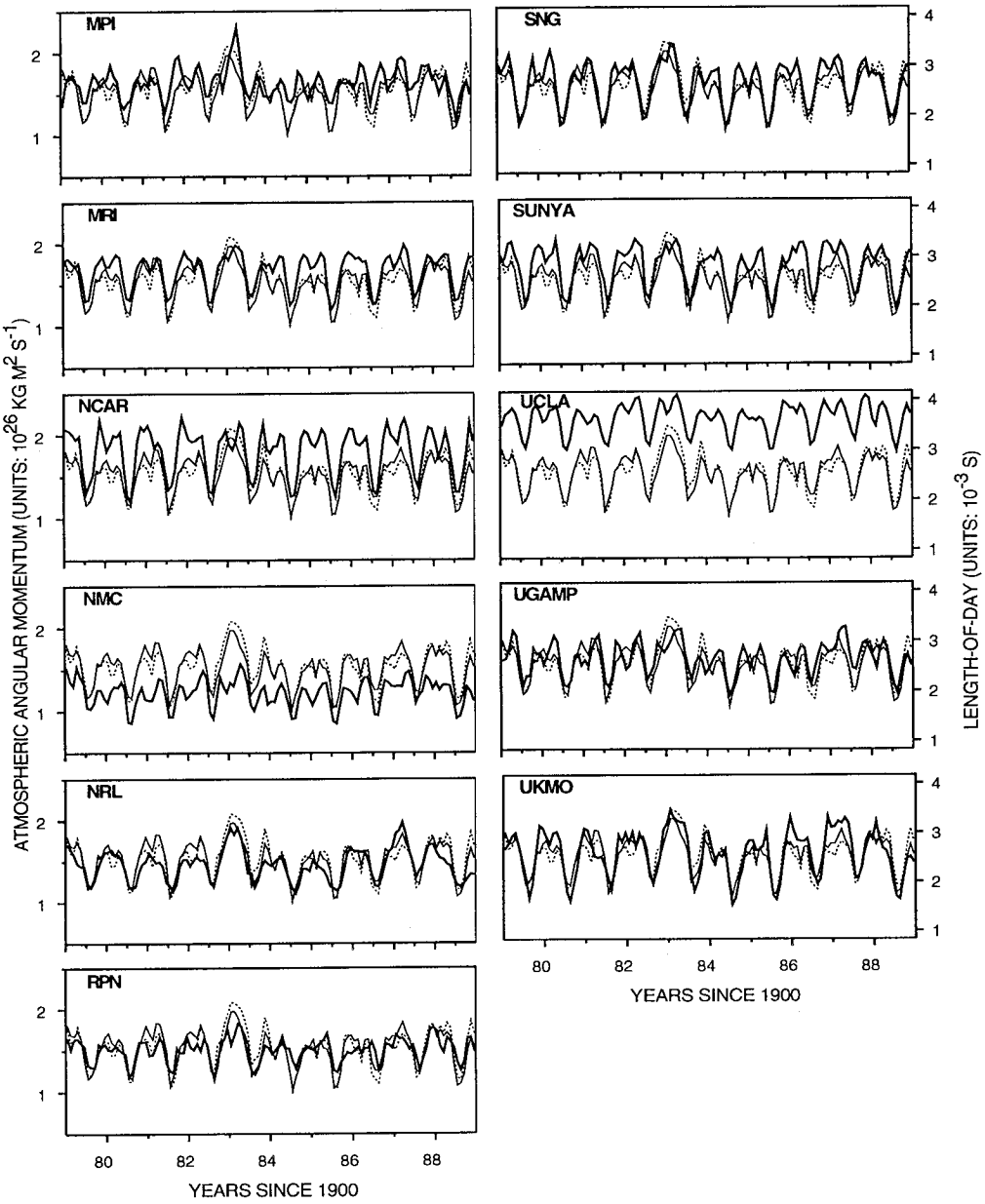

Figure 2. (continued)

the amplitude of the annual and interannual components of the observed AAM are somewhat underestimated relative to the LOD, partly because of neglect of the atmosphere above 50 mbar [*Rosen and Salstein,* 1985; *Dickey et al.*, 1994]. The overall agreement between the simulated and observed results is fairly good, but significant biases are found in some cases, with several models showing values that are consistently higher or lower than the observed AAM (note that LOD cannot be used to infer the time-averaged value of AAM, because its definition includes an arbitrary reference level). The dominance of the seasonal cycle is evident in all data sets, with amplitudes significantly less than the observed value visible for several of the models, while greater amplitudes are obtained for others. On interannual timescales, the large signature of the 1982-1983 ENSO is clearly seen in both the AAM and LOD time series. This signal is well captured by several of the models, but not by others. These broad findings are evident in the following detailed intercomparisons of the decadal mean AAM and AAM fluctuations on seasonal and interannual timescales as given by the AMIP models and by operational NMC analyses.

3.1. Decadal Mean

The global atmosphere's superrotation is its most striking dynamic, long-term feature. During the AMIP decade 1979-1988, the observed mean value is 1.51×10^{26} kg m^2 s^{-1} which, if transferred to the underlying solid Earth would, if the solid Earth were perfectly rigid, reduce the length of the day by 2.5 ms (see equations A7, A9, A10, and A11). Values yielded by each of the AMIP models are plotted in Figure 3, along with the median and IQR of the model values. The model median M^w is only 3.5% larger than the observed value with 10 of the 23 model values within ± 5% of the observed. More significant departures from the observed value are found in other models, five of which give values differing by more than 15% from the observed. Included in

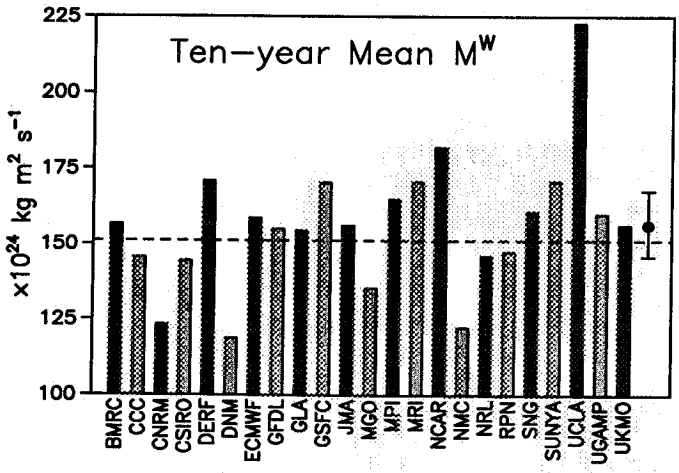

Figure 3. Mean value of the relative angular momentum of the atmosphere between 1000 and 50 mbar during the decade 1979-1988 for each of 23 models. Right-most element indicates the median and the upper and lower quartiles of the distribution of model values, with the length of the vertical line connecting the last two depicting the interquartile range. The dashed line indicates the value observed for the same decade based on NMC operational analyses. Model abbreviations are listed in Table 1.

this group of poorer results is that from the NMC; because versions of the NMC model were at the heart of the four-dimensional data assimilation system that created the validation values used here, the NMC model's lack of success in Figures 2 and 3 suggests that observations are indeed capable of modifying a model's initial guess field in modern data assimilation schemes.

Figures 2 and 3 suggest that biases in GCM simulations of the zonal wind field are not uniform, and the identification of the causes of the observed discrepancies may not be straightforward. The difficulties involved are evident from Figure 4, in which the decadal mean observed $[u]$ and the errors in $[u]$ are shown for those models that yield the two largest and the two smallest values of M^w in Figure 3, respectively. Remarkably, the meridional distribution of the bias in $[u]$ shows wide variations, even within each class of model errors in M^w. Thus the main source of the large value for the decadal mean of M^w seen in the UCLA model is excess values of $[u]$ above 200 mbar from 60°N to 60°S, whereas the erroneously large NCAR value of M^w arises primarily from $[u]$ errors below 200 mbar. The low value of the mean M^w seen in the NMC model results arises from systematically low values of $[u]$ throughout the tropics, particularly in the upper troposphere and lower stratosphere, whereas the very low value of the mean M^w from the DNM model has its source in extratropical regions, with the tropics contributing a positive but smaller bias.

For comparison, Figure 5 gives the $[u]$-bias field for the GLA model, whose decadal mean M^w lies closest to that observed for 1979-1988. It appears that success in reproducing the global mean value of M^w need not imply similar success with the decadal mean $[u]$ field, for the magnitude of the $[u]$ biases evident in Figure 5 is of the same order as those shown in Figure 4 for the outlier M^w simulations. Evidently, for the GLA model at least, the good performance for decadal mean M^w arises from the cancellation among regional biases in $[u]$ of opposite sign, biases which in many locations are comparable to the observed value of $[u]$ there (compare Figure 4a). The (area-weighted) mean absolute error in $[u]$ for the GLA field in Figure 5 is 2.3 ms^{-1}. At 1.9 ms^{-1} (IQR = 2.3–1.7 ms^{-1}), the median value of this statistic is smaller than the observed mean absolute value of $[u]$ in Figure 4a, 8.5 ms^{-1}, but not by so much that we can be sanguine about this aspect of the performance of the models.

Despite the differences shown in Figure 4 for $[u]$ among an outlier subset of AMIP models, it remains of interest to quantify the similarity in model biases among the general population of AMIP models. To this end, we have performed an empirical orthogonal function (EOF) analysis of the biases present in the set of $m_b{}^w$ values in the 46 belts for the 23 models. EOF analysis provides a convenient means to identify those independent patterns that most efficiently explain the variability in a data set

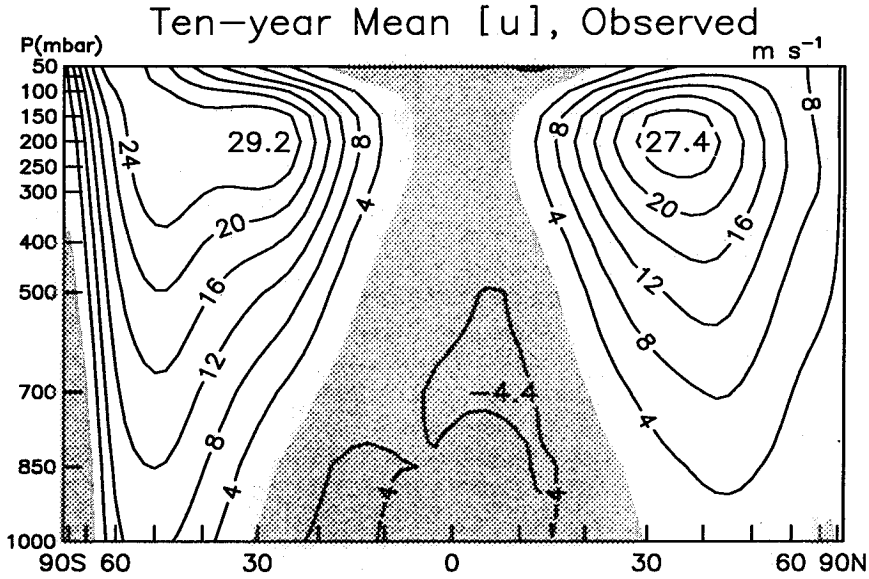

Figure 4a. Meridional cross section of the average value of the zonal mean zonal wind observed during the decade 1979-1988 based on NMC operational analyses. Standard pressure levels marked along the ordinate correspond to the vertical distribution of the archived analyses. Shaded values are negative (easterlies). The global mean value of the $[u]$ field shown here is 6.8 ms^{-1}.

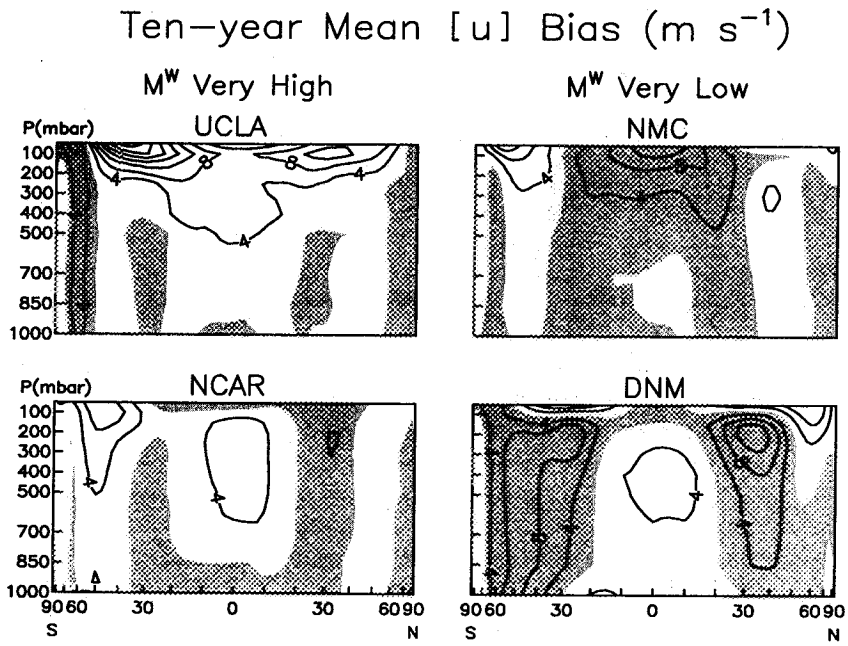

Figure 4b. Meridional cross sections of the average value of the zonal mean zonal wind during the decade 1979-1988 for four selected models minus the observed value from Figure 4a. (Left) Models with the two largest values of M^w in Figure 3; (Right) models with the two smallest values of M^w in Figure 3. Negative values are shaded. Model abbreviations are listed in Table 1.

[*Preisendorfer*, 1988]. Three significant modes of common variability in the belt momentum error distribution emerge (Figure 6) which together explain more than 87% of the variance in the full ensemble of m_b^w biases.

Mode 1, involving errors primarily in northern and southern mid-to-high latitudes with a tendency for smaller, compensating errors in the subtropics, is notable in that the weights for 19 of the models in its principal component are of the same sign. Recognizing that errors for a particular model are often spread across all three modes, the commonality of behavior expressed by mode 1's principal component nevertheless suggests the existence of a shared, underlying difficulty in modeling the climatological, regional distribution of angular momentum. Mode 2 reveals a pattern in which biases in the tropics and in northern midlatitudes are in opposition, and mode 3 emphasizes behavior in the southern extratropics.

3.2. Seasonal Cycle

The seasonal cycle in AAM derives from the asymmetry in the land-ocean distributions of the northern and southern hemispheres and the resulting difference in the seasonality of the two hemi-

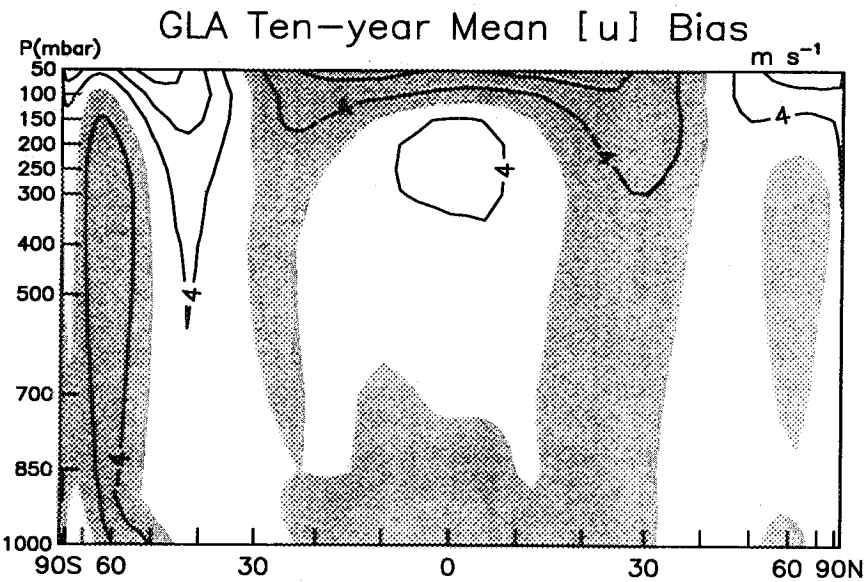

Figure 5. Meridional cross section of the average value of the zonal mean zonal wind during the decade 1979-1988 for the GLA model minus the observed value from Figure 4a. Negative values are shaded.

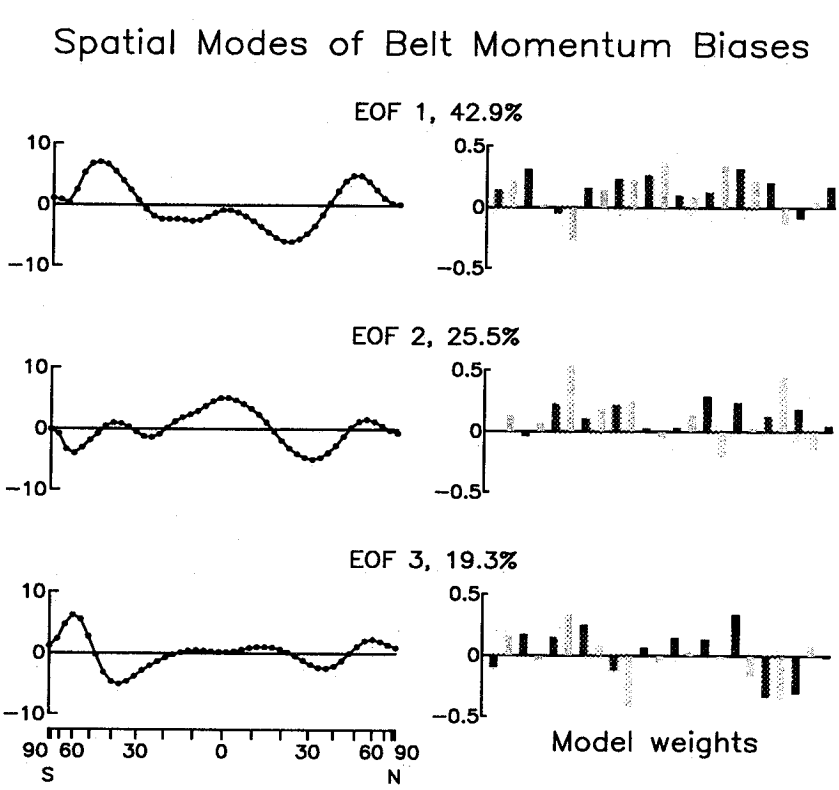

Figure 6. The three leading empirical orthogonal functions (EOFs) of the covariance matrix formed from the 23 model time series of the difference between the decadal mean model value of the relative angular momentum in each of 46 equal-area belts (m_b^w) and the observed value. (Left) The eigenvector is plotted in units of 10^{24} kg m^2 s^{-1}. (Right) The weight contributed by each model to each of the EOFs is given in nondimensional, normalized units; the models are shown in the same sequence as in Figure 3. The percent of the variance in all the model's belt momentum biases explained by each EOF is also shown.

spheres' subtropical jets [*Rosen et al.*, 1991b]. Because the seasonal cycle represents the largest mode of variability in the AAM time series, it is important that GCMs be able to replicate this signal well. It is encouraging therefore to see in Figure 7 that the AMIP models do tend to reproduce the behavior observed in the climatological monthly mean progression of M^w values. It is worth noting, however, that the models also exhibit a general tendency to underestimate the maximum values observed in December–February. Indeed, in some models this deficiency is quite pronounced, leading to seasonal cycles with distinct maxima around April and November instead of the observed single broad maximum across December through April.

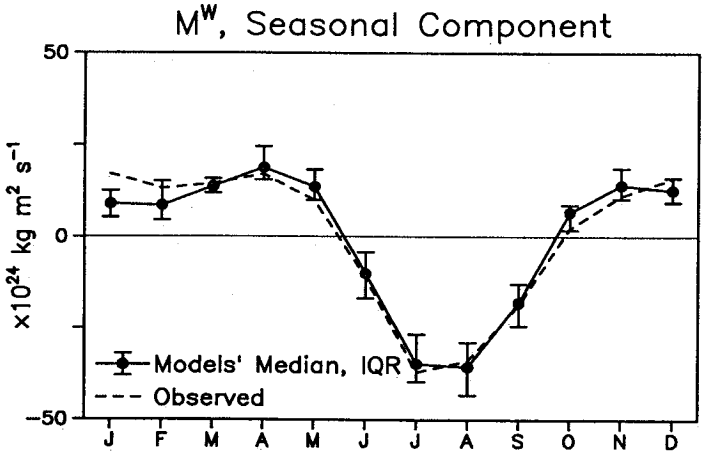

Figure 7. The median among the 23 model values of the relative angular momentum of the atmosphere between 1000 and 50 mbar for each composite calendar month of 1979-1988 (solid line), along with the upper and lower quartiles of the distribution of model values for each composite month. The dashed line indicates the observed composite monthly values, based on NMC operational analyses. The decadal mean of the series for each model and for the observations has been removed prior to generating these results. IQR denotes interquartile range.

The degree to which the models share common problems in reproducing the observed shape of the seasonal cycle in M^w is revealed by an EOF analysis of the models' composite monthly errors (Figure 8). The tendency of the models to underestimate M^w during northern winter is apparent in both of the first two modes of this analysis by the preponderance of positive model weights multiplying negative anomalies in the modes' time series then. The first mode in Figure 8 captures errors in the models' estimates of the annual component of M^w, whereas the second mode captures errors in their semiannual component. (The semiannual component of M^w is normally observed to peak in early May, and its amplitude is about 80% of that of the annual component, which peaks in early February [*Rosen*, 1993].) The general shortcoming of the models in December-February appears to project onto a proclivity toward underestimating the annual, while overestimating the semiannual, component of the observed seasonality in M^w.

Figure 9 displays a measure of the amplitude of the seasonal cycle, namely, the standard deviation (σ_s) of the twelve composite calendar-month means of M^w, for each AMIP model and the observed series. The median σ_s value is only some 2.4% larger than the observed σ_s, with nearly half of the model values lying within about 15% of the observed. Nevertheless, notable outliers also ex-

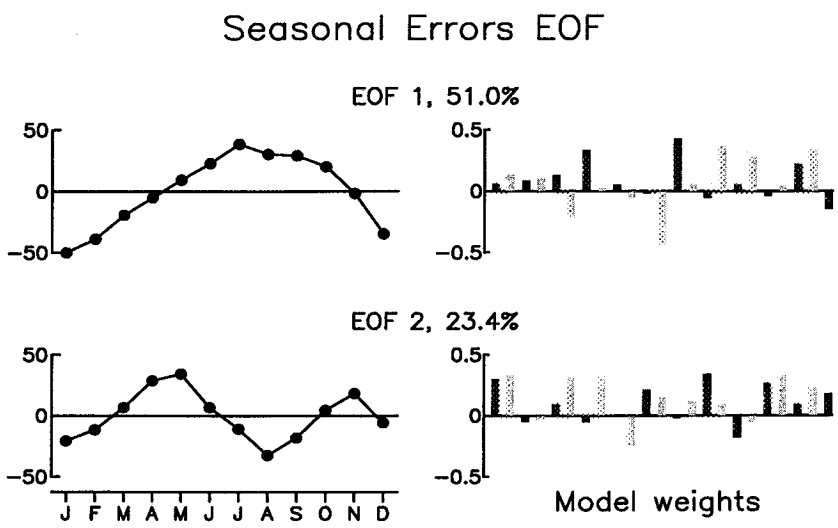

Figure 8. The first two empirical orthogonal functions (EOFs) of the covariance matrix formed from the 23 models' time series of their composite monthly values of M^w minus the observed value. (Left) The eigenvector is plotted in units of 10^{24} kg $m^2 s^{-1}$. (Right) The weight contributed by each model to each of the modes is given in nondimensional, normalized units; the models are shown in the same sequence as in Figure 3. The percent of the variance in all the models' seasonal errors explained by each mode is also shown.

ist in Figure 9, so that the range in values for σ_s exceeds a factor of 2. There does not appear to be any relationship between errors in a model's seasonal cycle and in its decadal mean bias, with high values of σ_s being equally likely to be associated with either high or low values of decadal mean M^w in Figure 3 (and similarly for low values of σ_s). On the other hand, according to Table 1, four of the five models with decadal means that do not lie within 15% of the observed mean have seasonal variations that do not lie within 15% of the observed value, suggesting that there may be some linkage between poor model performance on decadal mean and seasonal timescales. Also shown in Figure 9 is the correlation coefficient (r_s) between each model's series of composite monthly M^w values and the observed series. In conjunction with σ_s, the r_s statistic helps provide a more complete analysis of the fidelity of a model's simulation. Not surprisingly, in light of Figure 7, r_s is generally quite large (median = 0.95; IQR = 0.97 - 0.92).

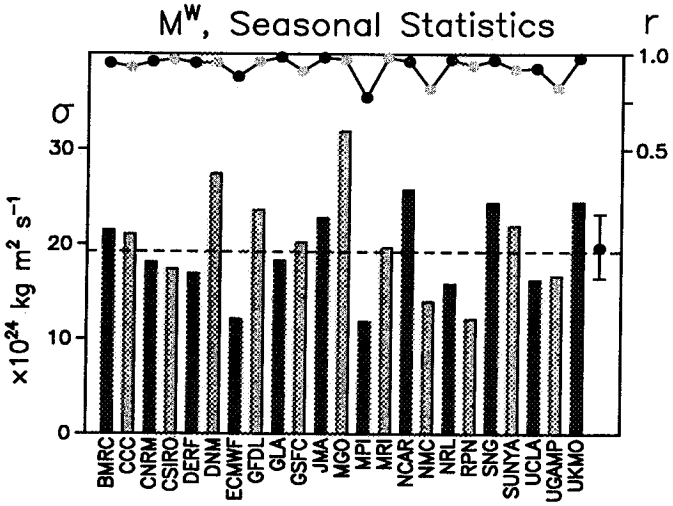

Figure 9. (Bottom) Standard deviation of the 12 composite calendar month means during 1979-1988 of the relative angular momentum of the atmosphere between 1000 and 50 mbar (M^w) for each of 23 models (abbreviations given in Table 1). To the right on the same scale are plotted the median and the upper and lower quartiles of the distribution of model values. The dashed line indicates the value observed for the same decade based on NMC operational analyses. (Top) Correlation coefficient (scale on right) between each model's series of composite monthly M^w values and the observed series.

Although the bulk of the observed seasonal variability in $m_b{}^w$ occurs in connection with the subtropical jets of each hemisphere (Figure 10a), this need not imply that the errors present in Figure 9 originate mostly there. Therefore to isolate regionally the source of seasonal model errors in M^w, we have calculated for each model: (1) the variance in the difference between the composite monthly mean values of its belt series $m_b{}^w$ and the observed $m_b{}^w$ values, and (2) the covariance between these seasonal errors in the model belt values and the seasonal errors in global M^w, normalized by the variance in the latter. Because the sum of the covariance in calculation (2) over all 46 belts is equal to the variance in a model's seasonal errors in global M^w, the sum of these 46 values for a particular model is unity. Hence the covariance provides a convenient measure for quantifying the contribution made by seasonal errors in various regions to the global error, as was done by *Rosen et al.* [1991a] in connection with medium-range forecast model errors.

Errors in the models' simulations of $m_b{}^w$ seasonal cycles are less spatially focused than is the profile of the observed $m_b{}^w$ variance in Figure 10a. Indeed, a plot of the variances in calculation (1) as a function of latitude for the 23 models is too noisy to be useful, so Figure 10b attempts to summarize this result by presenting a profile of the median in each belt of all the models' seasonal belt error variances, along with the IQR of these 23 numbers. The large values of the IQR in the figure, especially in the extratropics, attest to the strikingly wide range of model behavior. (Note that the median values plotted in Figure 10 are determined individually for each belt; the profile does not represent the behavior of a single, "median" model.) The largest model errors in simulating the observed seasonal cycles in $m_b{}^w$ tend to flank both sides of the two maxima in Figure 10a,

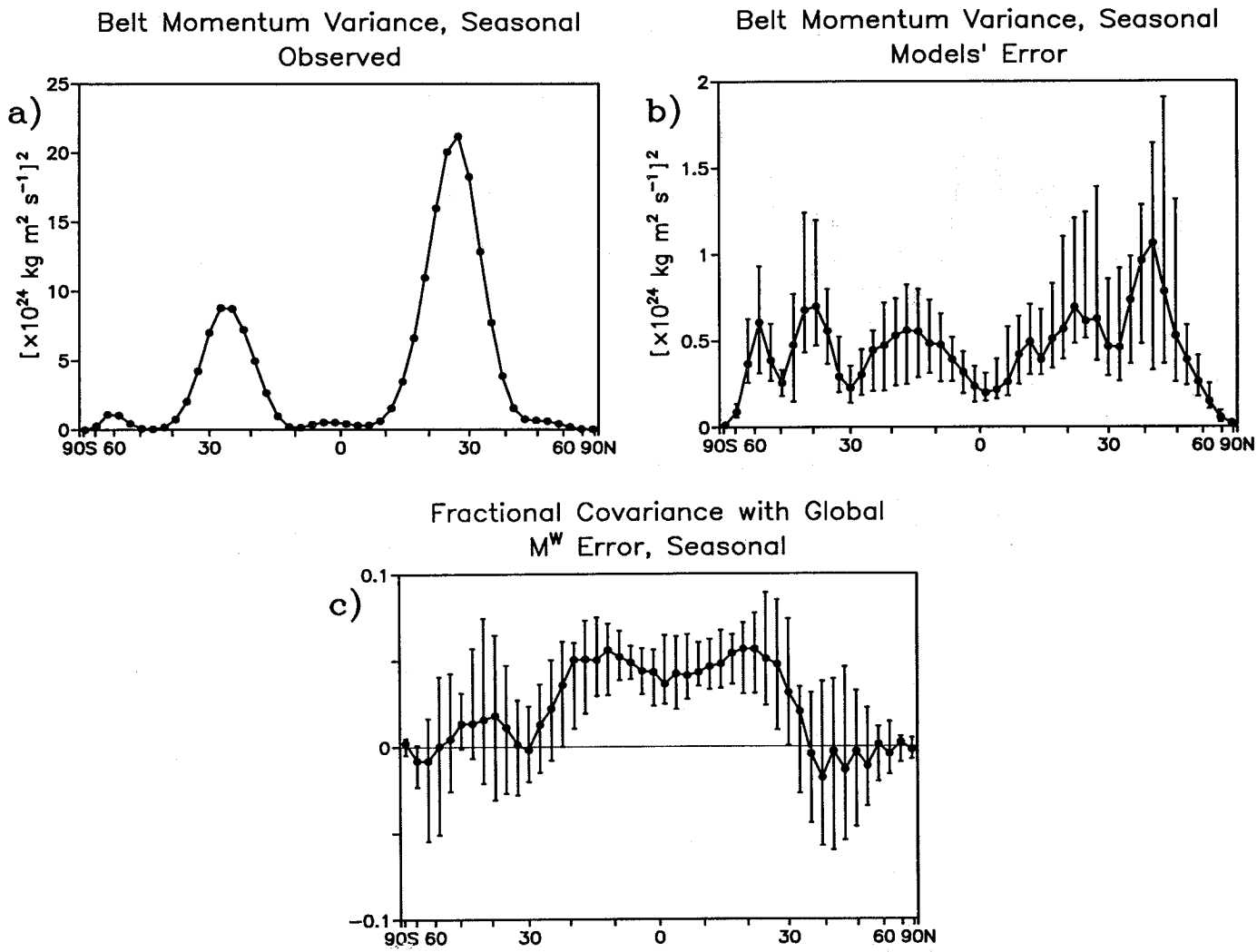

Figure 10. (a) The variance observed in the composite calendar month values of the relative angular momentum in each of 46 equal-area belts ($m_b{}^w$), based on NMC operational analyses for 1979-1988. (b) The median among the 23 model values of the variance in a model's seasonal errors in $m_b{}^w$ (i.e., the difference between a model's composite monthly mean series of $m_b{}^w$ and the observed $m_b{}^w$ series), along with the upper and lower quartiles of the distribution of the 23 model values of this error variance for each belt. (c) The median among the 23 model values of the covariance between the seasonal errors in a model's series of $m_b{}^w$ and the seasonal errors in its series of M^w, divided by the variance in the seasonal errors in the model's series of M^w. Also plotted are the upper and lower quartiles of the distribution of the 23 model values of this fractional error covariance for each belt.

suggesting that errors in positioning the subtropical jets properly are a factor. On the other hand, the amplitude of the largest median errors in Figure 10b is considerably smaller than that of the observed variance peaks in Figure 10a, suggesting that the models do a credible job in reproducing the seasonal change in the strength of the subtropical jets.

The fractional covariance between seasonal belt and global momentum errors plotted in Figure 10c indicates that, on average, the model errors that contribute most to failures in reproducing the observed seasonal cycle in M^w originate in the equatormost pair of peaks in Figure 10b, near 20°N and 15°S. The large local errors in northern midlatitudes shown in Figure 10b tend not to be so important for the globally integrated error. Note again, however, the very large spread in model behavior outside the tropics depicted by the IQR values; for a number of models, errors poleward of the observed positions of the subtropical jets are indeed a major reason for problems with simulating the seasonality in M^w.

3.3. Interannual Variations

The AMIP decade encompassed two ENSO events, those of 1982-1983 and 1986-1987. The former is possibly the strongest such event on record, and the notable positive anomaly in AAM and LOD associated with it led to a resurgence of interest in low-frequency variations in the planetary angular momentum budget. (For recent results and references, see *Ponte et al.* [1994] and *Dickey et al.* [1994].) The signature of the two ENSO events during the 1979-1988 AMIP period is apparent in the observed interannual M^w anomaly series in Figure 11 as a sharp peak in early 1983 and a broader, less intense maximum from late 1986 through 1987. On average, the AMIP models reproduce the observed interannual anomaly series fairly well, though less successfully than in the case of the seasonal cycle (Figure 7). It is noteworthy that the models, as a group, tend to underestimate the amplitude of the 1982-1983 ENSO signal in AAM but overestimate the 1986-1987

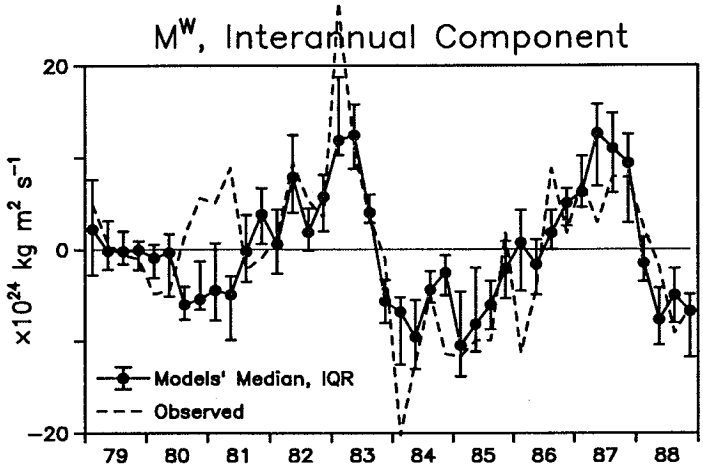

Figure 11. As in Figure 7, but for the interannual component of the relative angular momentum of the atmosphere between 1000 and 50 mbar (M^w) formed by averaging monthly values of M^w in each of 40 seasons during 1979-1988 and subtracting from this series the decadal mean seasonal cycle.

signal. The models also miss the intensity of the negative anomaly observed in 1984, although they do capture the rate of decline in M^w during 1983 fairly well. Notably, though, the models miss even the sign of the anomaly observed during mid-1980 through mid-1981, which according to the NMC observations results mainly from positive wind anomalies in the southern hemisphere tropics (not shown).

Figure 12 gives the interannual standard deviation (σ_I) for each model separately, along with the correlation coefficient (r_I) between each model's time series of 40 seasonal anomalies and the observed. The median value of σ_I is quite close to the observed, and, as in the case of the seasonal cycle, almost half of the model σ_I values lie within about 15% of the observed, although in the interannual case there is a notable skewness in the distribution toward low values. No relationship between individual σ_I and σ_s

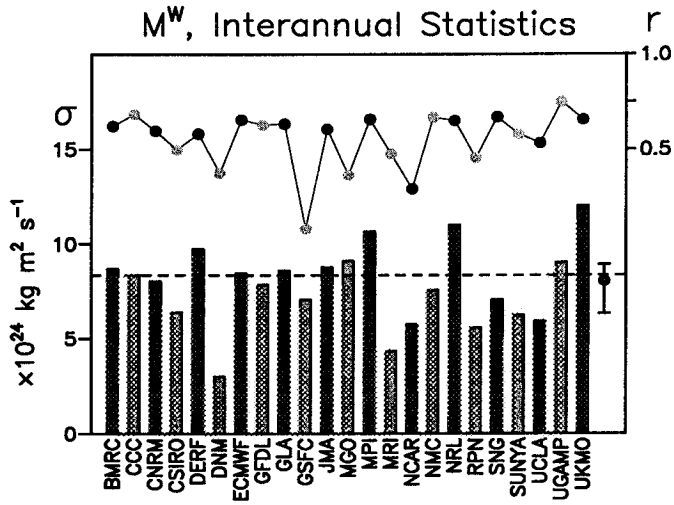

Figure 12. As in Figure 9, but for the interannual component of the relative angular momentum of the atmosphere between 1000 and 50 mbar (M^w) formed by averaging monthly values of M^w in each of 40 seasons during 1979-1988 and subtracting from this series the decadal mean seasonal cycle. Model abbreviations are listed in Table 1.

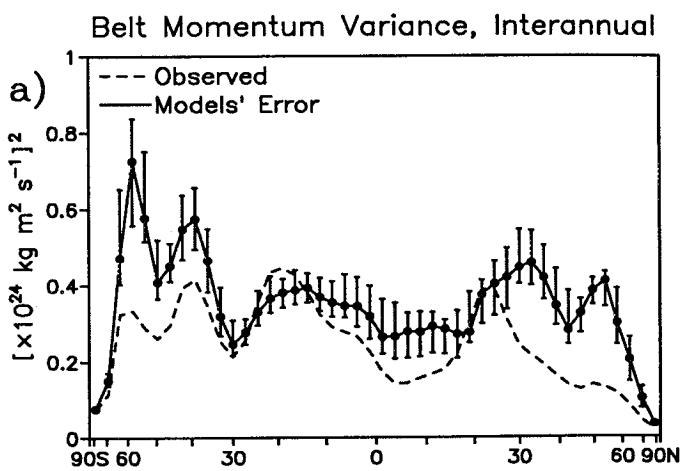

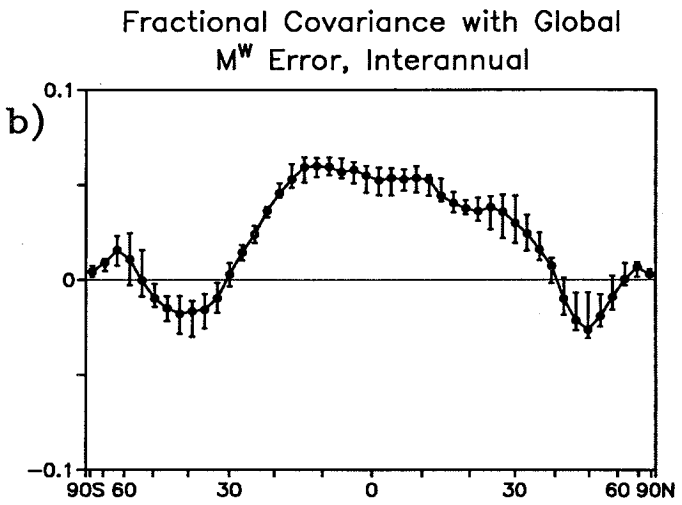

Figure 13. (a) As in Figures 10a and 10b, but for the interannual component of the relative angular momentum in each of 46 equal-area belts ($m_b{}^w$) formed by averaging monthly values of $m_b{}^w$ in each of 40 seasons during 1979-1988 and subtracting from this series the decadal mean seasonal cycle. (b) As in Figure 10c, but for the interannual component.

values is evident in the data; the performance of each model on one timescale seems to be independent of its performance on the other (see Table 1). A striking difference between overall model performances on seasonal and interannual timescales is that r_I is notably smaller than r_s. The median of r_I is 0.61 with 0.66-0.49 as the corresponding IQR value. On the basis of calculations of the autocorrelation present in the observed and modeled anomaly series, we estimate that in each series the number of degrees of freedom is about 12, implying that a value of r_I greater than about 0.5 is to be regarded as being statistically significant. Sixteen of the models (nearly 70%) exceed this criterion.

Calculations similar to those reported in Figure 10 for the seasonal cycle in $m_b{}^w$ have also been performed for interannual variability in $m_b{}^w$, and these are reproduced in Figure 13. The meridional profile of median model errors in the $m_b{}^w$ interannual component tends to be spatially correlated with the profile of the observed interannual variance in $m_b{}^w$ (Figure 13a). Unlike the case for the seasonal cycle, local errors in the interannual $m_b{}^w$ component are typically of the same order as the observed signals across the entire profile. Indeed, interannual errors in $m_b{}^w$ are not much smaller than seasonal errors in $m_b{}^w$ despite the disparity in

the amplitude observed for the two timescales. According to Figure 13b, errors in $m_b{}^w$ within 20° of the equator account for most of the interannual errors in M^w. In light of the relatively small values of IQR also plotted in Figure 13b, this result is rather robust across the suite of 23 AMIP models.

4. Discussion and Summary of Results

Here we have presented results of a study comparing atmospheric angular momentum (AAM) simulations by a variety of AMIP models (Table 1) with the NMC observed values and those inferred from geodetic data. Results from 23 AMIP model runs were considered on three distinct timescales: decadal mean, the seasonal cycle, and interannual variation. Of the 23 models (Table 1), 4 scored well (being within ±15% of that observed) on all three timescales, 10 on two out of three, 6 on one of the three, and 3 performed poorly on all three timescales. It should be stressed that the GCM results presented here represent "snapshots" (ca. early 1990s) of model evolution that is ongoing at the participating centers. For example, a new gravity wave drag parameterization has recently been developed at UCLA [*Kim and Arakawa*, 1995], which shows considerable promise for reducing the westerly bias present in the UCLA GCM in conjunction with envelope orography [*Kim*, 1996].

The decadal mean values of AAM were generally well simulated, with the model median value (1.58×10^{26} kg m^2 s^{-1}) being only 3.5% larger than the observed. Ten of the 23 models produced values that are within 5% of the observed mean; however, 5 of the 23 models are more than 15% away from the observed (Table 1). Examination of the decadal mean $[u]$ bias with respect to observed winds as a function of latitude and height indicates that contributing errors may be very different in models that show the same characteristic global anomaly (Figure 4). Furthermore, good agreement with the observed decadal mean cannot be taken to infer similar agreement with the observed $[u]$ fields (Figure 5), as cancellation among regional differences may combine to produce a low global bias. An EOF analysis performed on angular momentum values in the 46 belts for the 23 models produced three dominant modes explaining 87% of the variance. Both mode 1 (involving errors in the northern and southern mid-to-high latitudes with smaller partially canceling errors in the subtropics) and mode 2 (bias in the tropics with compensating bias in the northern midlatitudes) are common to the majority of the models, indicating shared problems in modeling the latitudinal distribution of mean angular momentum.

The seasonal cycle results from asymmetry of the land-ocean distribution of the northern and southern hemispheres, and is generally well simulated in the AMIP models. The median seasonal standard deviation (σ_s) value is 2.4% larger than observed, with 10 of the models being within 15% of the observed amplitude (Figure 9 and Table 1). The correlation between observed and model seasonal cycles is quite high, with a median value of r_s = 0.95 (IQR = 0.97–0.92). An EOF analysis provides insight into common seasonal errors; the first mode shows a tendency for most models to underestimate the annual cycle, while the second mode largely reflects overestimates of the semiannual cycle (Figure 8), both consistent with the models' tendency to underestimate global AAM during northern hemisphere winter. The observed seasonal cycle in AAM is dominated by contributions from the subtropical jets from each hemisphere (Figure 10a), whose strength is generally well reproduced by the models. The largest regional model errors, whose seasonal variance is about an order of magnitude smaller than the observed variance (Figure 10b), tend to border on both sides of the two hemispheric maxima, indicating that errors in positioning the subtropical jets are an issue. Further, examination of the fractional covariance between the regional and global momentum errors (Figure 10c) indicates that most of the seasonal M^w errors originate equatorward of the subtropical jets.

The models' interannual AAM variability is fairly realistic, with the median value of σ_I being quite close to the observed value and 10 of the model σ_I values lying within 15% of the observed. Although less robust than the seasonal cycle, the correlation between the observed and model interannual series has a statistically significant median value of 0.61. The two ENSO events during the AMIP decade are clearly evident; however, accurate simulation of intensities of the AAM signatures of individual episodes is generally lacking, as the 1982-1983 event is underestimated and the 1986-1987 event is overestimated by the model consensus (Figure 11). Examination of the latitudinal error covariance structure shows that errors within 20° of the equator account for most of the interannual mismodeling of M^w (Figure 13b). No relationship is evident between errors on interannual and seasonal timescales in a given model (see Table 1).

The principal objective of AMIP is to identify deficiencies in numerical models so that they can be removed. Except near the equator, the thermal wind relationship based on quasi-geostrophic balance in the horizontal and hydrostatic balance in the vertical relates the vertical rate of change of horizontal wind to the local horizontal gradient of potential density, which depends on temperature, pressure, and moisture content. In using this relationship to obtain a good leading approximation to the wind itself at a general point in the atmosphere, there is a horizontal function of integration which can be evaluated from the surface winds. It follows that any model that satisfactorily represents both (1) surface winds and (2) horizontal variations of temperature and moisture content should score well on the angular momentum assessment carried out in this paper, and conversely. It is possible, of course, that models that represent angular momentum fluctuations well might, owing to compensating errors, be doing so for the wrong reasons. For example, many of the models participating in the AMIP campaign show cold biases in both the tropics and extratropics [*Fiorino*, 1995]; the matching signs of these temperature biases serve to minimize errors in the meridional temperature gradient, which in turn helps many of the models to achieve realistic values for the decadal mean AAM.

In any event, it is obvious that any modeling groups exploiting the results presented in this paper should in the first instance examine those features of the model that determine the pattern of surface winds and the distribution of temperature and moisture within the atmosphere. Of particular importance will be parameterization schemes for representing oceanic and continental boundary layers, mechanical interactions of the atmosphere with orography, including drag due to the excitation of gravity waves, and the role of moist convection and radiative processes in the atmosphere, where the presence of clouds introduces serious complications now being studied intensively in various meteorological research centers.

These remarks might facilitate the use of atmospheric angular momentum "skill scores" in the important and by no means straightforward task of identifying deficiencies in parameterization schemes used in numerical models, with a view to improving the schemes. Much careful work will be needed, however, for a cursory inspection of skill scores reveals no striking correlations with any of the manifold characteristics (see above paragraphs) of the various models used by groups participating in AMIP [*Phillips*, 1994]. In fact, no discretionary characteristics are shared

by the four models that are successful on all three timescales. The continuing Atmospheric Model Intercomparison Project will provide opportunities to pursue the necessary investigations.

Appendix: Atmospheric Excitation of Earth Rotation Variations

The absolute angular momentum of the atmosphere, a three-dimensional vector $M_i = M_i(t)$ (where t denotes time), can be written as the sum of two terms

$$M_i \equiv M_i^P + M_i^W \tag{A1}$$

where

$$M_i^P \equiv \iiint \rho \varepsilon_{ijk} x_j \varepsilon_{klm} \omega_l x_m d\tau \tag{A2a}$$

$$M_i^W \equiv \iiint \rho \varepsilon_{ijk} x_j u_k d\tau, \tag{A2b}$$

the "matter" (or pressure) and the "wind" contributions to M_i, respectively. Here $\rho(x_i,t)$ and $u_k(x_i,t)$ denote the mass density and wind velocity, respectively, at a general point, x_i, $i=1, 2, 3$ within the atmosphere, and $d\tau$ is a volume element of the atmosphere, over the whole of which the volume integral is taken. The usual summation convention is used for repeated suffixes, and ε_{ijk} is the alternating tensor with values 0 or $\pm$ 1. The frame of reference used has its origin at the center of mass of the whole Earth (solid inner core, liquid outer core, "solid Earth," hydrosphere, atmosphere) and is aligned with the principal axes of inertia of the "solid Earth" (mantle, crust, and cryosphere). With respect to an inertial frame, the rotation of the solid Earth has angular velocity $\omega_i(t)$, $i = 1, 2, 3$.

All components of M_i vary with time as a consequence of dynamical interactions between the atmosphere and the underlying planet, which produce measurable fluctuations in ω_i. It is customary to write

$$\omega_i(t) \equiv \big(\omega_1(t),\omega_2(t),\omega_3(t)\big) \equiv \Omega\big(m_1(t),m_2(t),1+m_3(t)\big), \tag{A3}$$

where $\Omega = 7.292115 \times 10^{-5}$ rad s^{-1} is the mean angular speed of sidereal rotation of the solid Earth in recent times. Over timescales that are short compared with those of geological processes, the magnitudes of the dimensionless quantities $m_1(t)$, $m_2(t)$ and $m_3(t)$ are all very much less than unity, so that for the purpose of determining M_i from meteorological data using (A2), it is sufficient to set $m_i = 0$, so that $\omega_i = (0, 0, \Omega)$.

The nonzero meteorological contributions to $m_i(t)$ are, of course, important in the study of fluctuations in the Earth's rotation. If L_i ($i = 1, 2, 3$) is the net torque acting on the Earth's atmosphere then

$$L_i = dM_i/dt = \dot{M}_i + \varepsilon_{ijk}\omega_j M_k, \tag{A4}$$

where dM_i/dt and $\dot{M}_i$ are the time rates of change of M_i in an inertial frame and in the rotating frame, respectively. When $\omega_i = (0, 0, \Omega)$, we have

$$L_1 = \dot{M}_1 - \Omega M_2,\ L_2 = \dot{M}_2 - \Omega M_3,\ L_3 = \dot{M}_3. \tag{A5}$$

It is well known that L_i cannot be determined as accurately as M_i from surface drag and pressure force determinations, owing to limited measurements, parameterization difficulties, and the high degree of cancellation involved. But efforts at doing so are now being undertaken with the aid of output from modern data assimilation systems and the numerical models at their core [*White*, 1991, 1993; *Salstein and Rosen*, 1994]. Through the action of L_i, angular momentum is exchanged back and forth between the atmosphere and the underlying planet, the surface of which is subjected by the atmosphere to an applied torque equal to $-L_i$. Most of the angular momentum exchanged, which in magnitude can be a considerable fraction of that of M_i^W, goes into the massive solid Earth, whose moment of inertia is some 10^6 times that of the atmosphere. This process produces (1) tiny but measurable changes in the length of the day

$$\Lambda(t) = \Lambda_0/\big(1+m_3(t)\big),\ \Lambda_0 \equiv 2\pi/\Omega, \tag{A6a}$$

as well as (2) movements of the poles of the instantaneous axis of rotation of the solid Earth relative to its axis of figure, as specified by the quantity

$$\boldsymbol{m}(t) \equiv m_1(t) + i\, m_2(t) \tag{A6b}$$

(where $i \equiv \sqrt{-1}$; see (A3)). Indeed, the strongest torques acting on the solid Earth are generated by atmospheric motions, which produce easily detectable changes in Λ of up to about 1 ms in magnitude (corresponding to change in $|m_3|$ of about 10^{-8}) and displacements of the pole of rotation of several meters (corresponding to changes in $|\boldsymbol{m}|$ of about 10^{-6}).

The torque $-L_i$ produced by atmospheric motions on the underlying planet is due to (1) tangential stresses in the turbulent boundary layers over the continents and oceans, and (2) normal stresses acting on orography and the Earth's equatorial bulge. Owing to the rigidity (albeit slightly imperfect) of the solid Earth, all three components of the "continental" part of $-L_i$ are transmitted to the solid Earth directly and fully. The oceanic part of $-L_i$ gives rise to a dynamical response in the oceans which requires further investigation, but the case when the whole of the applied torque is assumed to be passed on by the oceans to the solid Earth virtually instantaneously can be taken as realistic for most practical purposes, particularly when dealing with the axial component of $-L_i$ and the changes in Λ that it produces [*Ponte*, 1990]. Thus the oceans act as an intermediary in the angular momentum exchange process, by transmitting the applied stresses in the atmospheric boundary layer over the oceans to the continental margins and ocean bottom. It is a convenient circumstance that, owing to the slowness and scales of ocean currents in comparison with atmospheric winds, in the budget of angular momentum between the solid Earth and its overlying fluid layers, the hydrosphere (in spite of its much greater moment of inertia than that of the atmosphere, by a factor of about 300) produces effects which can be neglected to a first approximation.

In the theory of the interactions between the atmosphere and underlying planet that give rise to fluctuations in M_i, the analysis is facilitated by using in place of M_i the dimensionless AAM functions χ_i, $i = 1, 2, 3$ [see *Barnes et al.*, 1983]. They can be defined as follows:

$$\chi_i \equiv \chi_i^P + \chi_i^W = \int_{-\pi/2}^{\pi/2} \xi(\phi,t)\, d\phi = \int_{-\pi/2}^{\pi/2} [\xi_i^P(\phi,t) + \xi_i^W(\phi,t)]\, d\phi, \tag{A7}$$

where

$$\left(\xi_1^P, \xi_2^P\right) \equiv \frac{-1.098\overline{R}^4}{g(C-A)} \int_0^{2\pi} p_s \cos^2\phi \sin\phi (\cos\lambda, \sin\lambda)\, d\lambda, \tag{A8a}$$

$$\left(\xi_{S1}^{w},\xi_{S2}^{w}\right)\equiv\frac{-1.5913\overline{R}^{3}}{g(C-A)\Omega}\int_{0}^{p_s}\int_{0}^{2\pi}\cos\phi\left\{u\sin\phi\left(\cos\lambda,\sin\lambda\right)-v\left(\sin\lambda,-\cos\lambda\right)\right\}d\lambda dp, \tag{A8b}$$

$$\left(\xi_{S3}^{P},\xi_{S3}^{w}\right)=\left(\frac{0.753\overline{R}^{4}}{gC_m}\int_{0}^{2\pi}p_s\cos^{3}\phi\,d\lambda,\frac{0.998\overline{R}^{3}}{gC_m\Omega}\int_{0}^{p_s}\int_{0}^{2\pi}u\cos^{2}\phi\,d\lambda dp\right). \tag{A9}$$

In these expressions, (ϕ, λ) denote latitude and longitude, respectively, $p_S(\phi, \lambda, t)$ is the surface pressure, and u (ϕ, λ, p, t) and v (ϕ, λ, p, t) are the eastward and northward components, respectively, of the wind velocity at pressure level p. We take $\overline{R} = 6.3674\times10^{6} m$ for the mean radius of the solid Earth, Ω = 7.292115 × 10^{-5} rad s^{-1} for its mean rotation rate, g = 9.810 m s^{-2} for the mean acceleration due to gravity, C = 8.0376 × 10^{37} kg m^2 for the polar moment of inertia of the whole Earth, (C–A) = 2.610 x 10^{35} kg m^2 where A is the corresponding equatorial moment of inertia, and C_m = 7.1236 × 10^{37} kg m^2 is the polar moment of inertia of the Earth's mantle and crust. The coefficients 1.098, 1.5913, 0.753, and 0.998 incorporate the so-called Love number corrections, which allow for concomitant meteorologically-induced tiny but dynamically significant changes in the inertia tensor of the slightly deformable solid Earth, using the most up-to-date geophysical data [see *Eubanks*, 1993]. The dimensionless pseudovector χ_i is related to the AAM vector M_i, with the equatorial components (χ_1, χ_2) and (M_1, M_2) scaled differently from the axial components χ_3 and M_3. Routine determinations of χ_i have been made for several years at several meteorological centers (using older values of the "Love number" corrections, namely, 1.00, 1.43, 0.70 and 1.00, respectively, in place of 1.098, 1.5913, 0.753, and 0.998, C_m in place of C, and A_m in place of A in A8).

Any change in M_3 is accompanied by an equal and opposite change in the axial component of the angular momentum of the solid Earth (since the fluctuations in the azimuthal motion of the underlying liquid core of moment of inertia ~0.1C are effectively decoupled from those of the solid Earth on the short timescales with which we are concerned here). In terms of the dimensionless quantities m_3 and χ_3 this can be expressed as

$$\dot{m}_3+\dot{\chi}_3=0 \tag{A10}$$

with solution

$$m_3(t)+\chi_3(t)=m_3(t_0)+\chi_3(t_0), \tag{A11}$$

where $m_3(t_0)$ and $\chi_3(t_0)$ are constants of integration equal to m_3 and χ_3 at some initial instant $t = t_0$, respectively. The dominant contribution to fluctuations in χ_3 comes from the "wind" term χ_3^{W}, which depends on the distribution in the meridional plane of the average with respect to longitude λ of the eastward (westerly) wind speed. If one considers only the wind contribution, (A7) for the axial component simplifies to

$$\chi_3^{w}=\frac{0.998(2\pi)\overline{R}^{3}}{gC_m\Omega}\int_{0}^{p_s}\int_{-\pi/2}^{\pi/2}[u]\cos^{2}\phi\,d\phi\,dp, \tag{A12}$$

in which case M_3, the axial atmospheric angular momentum, reduces to

$$M_3^{w}=2\pi g^{-1}\overline{R}^{3}\int_{0}^{p_s}\int_{-\pi/2}^{\pi/2}[u]\cos^{2}\phi\,d\phi\,dp, \tag{A13}$$

Acknowledgments. We thank the members of the modeling groups who sent results to the Atmospheric Model Intercomparison Project (AMIP) of the World Climate Research Programme (WCRP), and we especially wish to thank W. L. Gates and his colleagues at the Lawrence Livermore Laboratory, who coordinated the AMIP effort. We acknowledge interesting discussions with C. R. Mechoso, K. Sperber, G. H. White, and the constructive comments of two anonymous reviewers. The work of J. O. Dickey and S. L. Marcus was carried out at the Jet Propulsion Laboratory, California Institute of Technology, under contract with the National Aeronautics and Space Administration. Programming assistance at AER was provided by P. Nelson. The work of R. D. Rosen and D. A. Salstein was supported in part by the National Science Foundation Climate Dynamics Program under grants ATM-9223164 and ATM-9632559, and NASA's Mission to Planet Earth Program under contract NAS5-32861 and grant NAGW-2615.

References

Anderson, J. D., and R. D. Rosen, The latitude-height structure of 40-50 day variations in atmospheric angular momentum, *J. Atmos. Sci.*, *40*, 1584-1591, 1983.

Barnes, R. T. H., R. Hide, A. A. White, and C. A. Wilson, Atmospheric angular momentum fluctuations, length of day changes and polar motion, *Proc. R. Soc. London A*, *387*, 31-73, 1983.

Bell, M. J., R. Hide, and G. Sakellarides, Atmospheric angular momentum forecasts as novel tests of global numerical prediction models, *Philos. Trans. R. Soc. London, Ser. A*, *334*, 55-92, 1991.

Black, R. X., D. A. Salstein, and R. D. Rosen, Interannual modes of variability in atmospheric angular momentum, *J. Clim.*, *9*, 2834-2849, 1996.

Chao, B. F., Interannual length of day variations with relation to the Southern Oscillation/El Niño, *Geophys. Res. Lett.*, *11*, 541-544, 1984.

Chao, B. F., Correlation of interannual length-of-day variation with El Niño/Southern Oscillation, 1972-1986, *J. Geophys. Res.*, *93*, 7709-7715, 1988.

Chao, B. F., Length-of-day variations caused by El Niño/Southern Oscillation and the quasi-biennial oscillation, *Science*, *243*, 923-925, 1989.

Dickey, J. O., Atmospheric excitation of the Earth's rotation: Progress and prospects via space geodesy, in *Contributions of Space Geodesy to Geodynamics—Earth Dynamics*, vol. 24, Geodyn. Ser., edited by D. E. Smith and D. L. Turcotte, pp. 55-70, AGU, Washington, D. C., 1993.

Dickey, J. O., M. Ghil, and S. L. Marcus, Extratropical aspects of the 40-50 day oscillation in length of day and atmospheric angular momentum, *J. Geophys. Res.*, *96*, 22,643-22,658, 1991.

Dickey, J. O., S. L. Marcus, J. A. Steppe, and R. Hide, The Earth's angular momentum budget on subseasonal time scales, *Science*, *225*, 321-324, 1992a.

Dickey, J. O., S. L. Marcus, and R. Hide, Global propagation of interannual fluctuations in atmospheric angular momentum, *Nature*, *357*, 484-488, 1992b.

Dickey, J. O., S. L. Marcus, T. M. Eubanks, and R. Hide, Climate studies via space geodesy: Relationships between ENSO and interannual length-of-day variations, in *Interactions Between Global Climate Subsystems, The Legacy of Hann, Geophys. Monogr. Ser.*, vol. 75, edited by G. McBean and M. Hantel, pp. 141-155, AGU, Washington, D. C., 1993.

Dickey, J. O., S. L. Marcus, R. Hide, T. M. Eubanks, and D. H. Boggs, Angular momentum exchange among the solid Earth, atmosphere, and oceans: A case study of the 1982-1983 El Niño event, *J. Geophys. Res.*, *99*, 23,921-23,937, 1994.

Eubanks, T. M., Variations in the orientation of the Earth, in *Contributions of Space Geodesy to Geodynamics—Earth Dynamics, Geodyn. Ser.*, vol. 24, edited by D. E. Smith and D. L. Turcotte, pp. 1-54, AGU, Washington, D. C., 1993.

Eubanks, T. M., J. A. Steppe, and J. O. Dickey, The El Niño, the Southern Oscillation and the Earth's rotation, in *Earth Rotation; Solved and Unsolved Problems, NATO Ad. Inst. Ser. C: Mathematical and Physical Sciences*, vol. 187, edited by A. Cazenave, 163-186, D. Reidel, Hingham, Mass., 1986.

Fiorino, M., AMIP overview—An analysis of the base state, in *Proceedings of the First International AMIP Scientific Conference, 15-19 May, 1995, Monterey, CA, Rep. World Climate Research Programme-92, World Meteorological Organization, technical document 732*, p. 531, Geneva, Switzerland, 1995.

Gates, W. L., AMIP: The Atmospheric Model Intercomparison Project, *Bull. Am. Meteorol. Soc.*, *73*, 1962-1970, 1992.

Hide, R., Presidential address: The Earth's differential rotation, *Q. J. R. Astron. Soc., 27*, 3-20, 1986.

Hide, R., and J. O. Dickey, Earth's variable rotation, *Science, 253*, 629-637, 1991.

Hide, R., N. T. Birch, L. V. Morrison, D. J. Shea, and A. A. White, Atmospheric angular momentum fluctuations and changes in the length of the day, *Nature, 286*, 114-117, 1980.

Jordi, C., L. V. Morrison, R. D. Rosen, D. A. Salstein, and G. Rossello, Fluctuations in the Earth's rotation since 1830 from high resolution astronomical data, *Geophys. J. Int., 117*, 811-818, 1994.

Kim, Y.-J., Representation of subgrid-scale orographic effects in a general circulation model: Impact on the dynamics of simulated January climate, *J. Clim., 9*, 2698-2717, 1996.

Kim, Y.-J., and A. Arakawa, Improvement of orographic gravity-wave parameterization using a mesoscale gravity-wave model, *J. Atmos. Sci., 52*, 1875-1902, 1995.

Lanzante, J. R., Resistant, robust and nonparametric techniques for the analysis of climate data: Theory and examples, including applications to historical radiosonde station data, *Int. J. Climatol., 16*, 1197-1266, 1996.

Marcus, S. L., and J. O. Dickey, Coupled poleward propagation of sea surface temperature and atmospheric angular momentum anomalies: Results from AMIP, in *Sixth Conference on Climate Variations*, pp. 70-74, Amer. Meteorol. Soc., Boston, Mass., 1994.

Marcus, S. L., M. Ghil, and J. O. Dickey, The extratropical 40-day oscillation in the UCLA general circulation model, I, Atmospheric angular momentum, *J. Atmos. Sci., 51*, 1431-1466, 1994.

Marcus, S. L., M. Ghil, and J. O. Dickey, The extratropical 40-day oscillation in the UCLA general circulation model, II, Spatial structure, *J. Atmos. Sci., 53*, 1993-2014, 1996.

Mo, K. C., J. O. Dickey, and S. L. Marcus, Interannual fluctuations in atmospheric angular momentum simulated by the NCEP MRF model, *J. Geophys. Res., 102*, 6703-6713, 1997.

Phillips, T. J., A summary documentation of the AMIP models, *PCMDI Rep. 18*, 343 pp., Program for Clim. Model Diagnosis and Intercomparison, Lawrence Livermore Natl. Lab., Livermore, Calif., 1994.

Ponte, R. M., Barotropic motions and the exchange of angular momentum between the oceans and solid Earth, *J. Geophys. Res., 95*, 11,369-11, 374, 1990.

Ponte, R. M., R. D. Rosen, and G. J. Boer, Angular momentum and torques in a simulation of the atmosphere's response to the 1982-83 El Niño, *J. Clim., 7*, 538-550, 1994.

Preisendorfer, R. W., *Principal Component Analysis in Meteorology and Oceanography*, 425 pp., Elsevier, New York, 1988.

Rosen, R. D., The axial momentum balance of Earth and its fluid envelope, *Surv. Geophys., 14*, 1-29, 1993.

Rosen, R. D., and D. A. Salstein, Variations in atmospheric angular momentum on global and regional scales and the length of day, *J. Geophys. Res., 88*, 5451-5470, 1983.

Rosen, R. D., and D. A. Salstein, Contribution of stratospheric winds to annual and semi-annual fluctuations in atmospheric angular momentum and the length of day, *J. Geophys. Res., 90*, 8033-8041, 1985.

Rosen, R. D., and D. A. Salstein, Atmospheric angular momentum signals during the 20th century, in *Proceedings, 21st Climate Diagnostics and Prediction Workshop*, Climate Prediction Center/NCEP/NOAA, in press, 1997.

Rosen, R. D., D. A. Salstein, T. M. Eubanks, J. O. Dickey, and J. A. Steppe, An El Niño signal in atmospheric angular momentum and Earth rotation, *Science, 225*, 411-414, 1984.

Rosen, R. D., D. A. Salstein, A. J. Miller, and K. Arpe, Accuracy of atmospheric angular momentum estimates from operational analyses, *Mon. Weather Rev., 115*, 1627-1639, 1987.

Rosen, R. D., D. A. Salstein, and T. Nehrkorn, Predictions of zonal wind and angular momentum by the NMC Medium-Range Forecast Model during 1985-89, *Mon. Weather Rev., 119*, 208-217, 1991a.

Rosen, R. D., D. A. Salstein, and T. M. Wood, Zonal contributions to global momentum variations on intraseasonal through interannual timescales, *J. Geophys. Res., 96*, 5145-5151, 1991b.

Salstein, D. A., and R. D. Rosen, Earth rotation as a proxy for interannual variability in atmospheric circulation, 1860-present, *J. Clim. Appl. Meteorol., 25*, 1870-1877, 1986.

Salstein, D. A., and R. D. Rosen, Topographic forcing of the atmosphere and a rapid change in the length-of-day, *Science, 264*, 407-409, 1994.

Salstein, D. A., D. M. Kann, A. J. Miller, and R. D. Rosen, The Sub-Bureau for Atmospheric Angular Momentum of the International Earth Rotation Service (IERS): A meteorological data center with geodetic applications, *Bull. Am. Meteorol. Soc., 74*, 67-80, 1993.

White, G. H., Mountain and surface stress torques in NMC analyses, in *Proceedings of the AGU Chapman Conference on Geodetic VLBI: Monitoring Global Change, NOAA Tech. Rep. NOS 137 NGS 49*, pp. 262-269, U.S. Dep. of Comm., Silver Spring, Md., 1991.

White, G. H., Mountain and surface stress torques in NMC analyses, in *Research Activities in Atmospheric and Oceanic Modeling, CAS/JSC Work. Group Numer. Exp. Rep. 18*, pp. 2.3-2.4, *World Meteorol. Org.*, Geneva, 1993.

J. O. Dickey and S. L. Marcus, Space Geodetic Science and Applications Group, Jet Propulsion Laboratory, California Institute of Technology, 4800 Oak Grove Drive, MS 238-332, Pasadena, CA 91109-8099. (e-mail: jod@logos.jpl.nasa.gov; slm@logos.jpl.nasa.gov)

R. Hide, Department of Physics, University of Oxford, Clarendon Laboratory, Parks Road, Oxford OX1 3PU, England. (e-mail: raymond.hide@jesus.ox.ac.uk)

R. D. Rosen and D. A. Salstein, Atmospheric and Environmental Research, Inc., 840 Memorial Drive, Cambridge, MA 02139. (e-mail: rdrosen@aer.com; salstein@aer.com)

(Received May 2, 1996; revised February 18, 1997; accepted March 3, 1997.)

Regional Sources of Mountain Torque Variability and High-Frequency Fluctuations in Atmospheric Angular Momentum

Haig Iskenderian and David A. Salstein

Atmospheric and Environmental Research, Inc.
Cambridge, Massachusetts

In press,
Submitted to *Monthly Weather Review*

Corresponding Author Address:

Dr. Haig Iskenderian

Atmospheric and Environmental Research, Inc.
840 Memorial Drive
Cambridge, MA 02139

phone: 617-547-6207
FAX: 617-661-6479

email: haig@aer.com

October 3, 1997

Regional sources of mountain torque variability and high-frequency fluctuations in atmospheric angular momentum

Haig Iskenderian and David A. Salstein

Atmospheric and Environmental Research, Inc.

840 Memorial Drive

Cambridge, MA 02139

ABSTRACT

The sources of high-frequency ($\leq$ 14 day) fluctuations in global atmospheric angular momentum (AAM) are investigated using several years of surface torque and AAM data. The midlatitude mountain torque associated with the Rockies, Himalayas, and Andes is found to be responsible for much of the high-frequency fluctuations in AAM, whereas the mountain torque in the Tropics and polar regions as well as the friction torque play a much lesser role on these time scales. A maximum in the high-frequency mountain torque variance occurs during the cool season of each hemisphere, though the Northern Hemisphere maximum substantially exceeds that of the Southern. This relationship indicates the seasonal role played by each hemisphere in the high-frequency fluctuations of global AAM.

A case study reveals that surface pressure changes near the Rockies and Himalayas produced by mobile synoptic-scale systems as they traversed these mountains contributed to a large fluctuation in mountain torque and a notable high-frequency change in global AAM in mid-March 1996. This event was also marked by a rapid fluctuation in length of day (l.o.d.), independently verifying the direct transfer of angular momentum from the atmosphere to solid Earth below. A composite study of the surface pressure patterns present during episodes of high-frequency

fluctuations in AAM reveals considerable meridional elongation of the surface pressure systems along the mountain ranges, thus establishing an extensive cross-mountain surface pressure gradient and producing a large torque. The considerable along-mountain extent of these surface pressure systems may help to explain the ability of individual synoptic-scale systems to affect the global AAM. Furthermore, midlatitude synoptic-scale systems tend to be most frequent in the cool season of each hemisphere, consistent with the contemporary maximum in hemispheric high-frequency mountain torque variance.

1. Introduction

Because of its conservative properties, atmospheric angular momentum (AAM) is often used to study the variations of the general circulation on time scales of days to years. Starr (1948) noted that the exchange of angular momentum across the atmosphere's lower interface is achieved by two independent mechanisms: friction torque and mountain torque. The friction torque is a result of the tangential stress placed upon the Earth's surface by the horizontal wind. The mountain torque arises from differences in surface pressure across the eastern and western faces of topographic features.

Several earlier studies of the mountain torque considered its contributions to variations in AAM from the time-averaged or zonally-averaged perspective. White (1949) computed the mountain torque in 5° latitude bands in the Northern Hemisphere for a single month and noted that, averaged over the one-month period, the mountain torque was of the same order of magnitude as the friction torque, and therefore the mountain torque could not be neglected in the angular momentum budget of the Earth-atmosphere system. White further found that the Northern Hemisphere mountain torque during this month was dominated by surface pressure differences across the Rockies and Himalayas. Newton (1971) studied the mountain torque in both hemispheres and noted that on the seasonal time scale the mountain torque, while weaker than the friction torque, played a significant role in the angular momentum budget.

On synoptic to sub-monthly time scales, the mountain torque is typically much larger than its monthly or seasonal average. Wei and Schaack (1984) demonstrated, using First GARP Global Experiment (FGGE) data from 1979, that such differences can be nearly one order of magnitude. Swinbank (1985) noted that there was a close connection between these high-frequency fluctuations in mountain torque and the changes in AAM during the FGGE period, which led him to suggest that on time scales of about a week, the mountain torque dominated the angular

momentum exchange. On the basis of such studies, Rosen (1993) concluded that the friction torque typically dominates the changes in AAM on time scales of months, whereas on time scales shorter than several weeks the mountain torque is the dominant mechanism.

Some case studies have isolated particular instances in which momentum exchange was affected by mountain torque on sub-monthly time scales. Rosen et al. (1984) noted a rapid increase in global AAM during January 1983, a period that coincided with the height of the 1982-83 El Niño-Southern Oscillation (ENSO) episode, and speculated that the changes in AAM were due to the mountain torque. Wolf and Smith (1987) followed by studying AAM changes during that strong ENSO event, suggesting that the mountain torque was produced by an eastward surface pressure gradient across the Rockies established by a mid-continent high pressure center to the east of the Rockies and a sequence of eastern Pacific cyclones to the west of the mountains. Salstein and Rosen (1994) investigated a six-day period in July and August 1992 during which there was a rapid oscillation in global AAM. They found that the mountain torque in the Southern Hemisphere was largely responsible for the rapid fluctuation in AAM, in association with a change in the zonal pressure gradient across the Andes due to a strong winter anticyclone that traversed the mountains. Recently, Czarnetzki (1997) identified mountain torque fluctuations with several cyclones in the lee of the Rockies.

These earlier case studies indicate that on synoptic time scales, surface pressure systems in the vicinity of major mountain ranges may alter the global AAM through the mountain torque. These studies also suggest that specific geographic locations such as the Rockies, Himalayas, and the Andes may be particularly influential as regions of AAM transfer. By using a longer time series of surface torque and AAM data than previously available, we will attempt to generalize these results by determining the regional sources of the mountain torque that typically lead to high-frequency AAM fluctuations. Then the features in the general circulation that are responsible for these fluctuations will be identified. Thus it is hoped that this study will help advance a more

complete picture of the angular momentum balance of the Earth-atmosphere system on high frequencies.

2. Definitions and data sources

The global atmospheric angular momentum about the Earth's axis can be expressed as

$$AAM = M_r + M_\Omega \tag{1}$$

where:

$$M_r = \frac{a^3}{g}\int\int\int u\cos^2\phi d\phi d\lambda dp \tag{2}$$

is the entire atmosphere's angular momentum associated with its motion relative to the rotating solid Earth, a is the Earth's radius, g acceleration due to gravity, u zonal wind, and the integral is performed over all latitudes, ϕ, longitudes, λ, and pressures, p.

The angular momentum associated with the rotation of the atmosphere's mass is:

$$M_\Omega = \frac{a^4\Omega}{g}\int\int p_s\cos^3\phi d\phi d\lambda \tag{3}$$

where Ω is the mean rotation rate of the Earth, and p_s the surface pressure (Rosen 1993).

The conservation of angular momentum states that changes in AAM are related to the surface torque by the relationship:

$$\frac{d}{dt} AAM = T_m + T_f \tag{4}$$

where the mountain torque (T_m) and friction torque (T_f) are defined through the following relationships (White 1991):

$$T_m = -a^2 \int\int p_s \frac{\partial H}{\partial \lambda} \cos\phi d\phi d\lambda \tag{5}$$

$$T_f = a^3 \int\int \tau \cos^2 \phi d\phi d\lambda . \tag{6}$$

Here, τ is surface stress and H indicates the height of the sloping topography.

The sense of the mountain torque is such that lower surface pressure on the western side of a north-south oriented mountain range relative to the eastern side (i.e., an eastward surface pressure gradient across the mountains) results in a positive torque on the atmosphere. Therefore, lower pressure on the western slopes relative to the eastern slopes of a mountain range tends to increase AAM through the mountain torque. In the case of the friction torque, an easterly surface wind will be indicated by $\tau > 0$ and a positive friction torque tending to increase AAM.

The torque and AAM data in this study were prepared by White (1991) using the National Centers for Environmental Prediction (NCEP) operational analysis system (Kanamitsu 1989). The calculations were based upon the initialized analysis on sigma levels, where the highest sigma level is at about 20 hPa. Calculations of mountain torque in (5) rely upon the product of analysis values of surface pressure and the zonal gradient of surface topography whereas friction torque in (6) relies on model-based surface stresses. This study used global integrals of torque and AAM, both of which were produced four times daily (00, 06, 12, and 18 UTC) for the period of February 1992 to November 1996. Torque data on a 1° x 1° grid used to compute the global integrals were

also available four times daily but were limited to the period April 1993-November 1996. To focus on regional patterns, we also used 1° x 1° gridded surface pressure data, available for the period April 1994-November 1996. The gridded fields and global integrals were daily averaged for this study and centered upon 09 UTC, the mean time of the four synoptic hours for a given calendar date. Because the mountain torque is an instantaneous value and the friction torque is a six-hour average, slightly different averaging techniques were used for the two torques to maintain the 09 UTC central time.

In section 3c, we identify a case of a pronounced high-frequency fluctuation in global AAM. To relate this fluctuation in global AAM to synoptic-scale surface and upper-air features, sea level pressure and 700 hPa geopotential height fields produced by the NCEP operational analysis system for the period of March 1996 were obtained from the National Center for Atmospheric Research (NCAR). These were available twice daily on a 2.5° x 2.5° grid. The length of day (l.o.d.) time series used was the Jet Propulsion Laboratory's (JPL) Kalman-filtered time series (after Gross 1996), which combines Earth rotation estimates from several space-geodetic techniques. These l.o.d. data are available once-daily at 00 UTC from September 1978 to February 1997.

3. Sources of high-frequency mountain torque variance

The overall quality of the NCEP data set can be judged in part by its ability to relate the sum of the globally-integrated surface torques to the AAM tendency, or equivalently, to satisfy (4). Figure 1 shows daily values of this balance for a 1-year subset of the global torque and AAM tendency time series, both of which are in reasonably good agreement on all time scales considered here. A low-frequency oscillation is apparent in both the torque and AAM tendency, with minima in January and July. Such a prolonged minimum in January is somewhat unusual, with the negative torque leading to a profound decrease in AAM around that time (not shown).

Superimposed upon the low-frequency signal are sub-monthly fluctuations in AAM tendency, and these are also well captured by the sum of the two torques. In fact, for the entire time period (February 1992 to November 1996) the correlation between the series is 0.86, indicating that this balance is well represented in the NCEP data set. The lack of complete agreement arises because mountain torque is calculated from the surface pressure and topography fields, whereas friction torque is calculated from physical parameterizations of the forecast model (Salstein and Rosen 1994). To place the rapid fluctuations in perspective, such surface torques typically produce an angular momentum change equivalent to about 10% of the mean value of M_r, as deduced from Fig. 2 of Rosen and Salstein (1983).

To assess the relative importance of mountain and friction torques to the high-frequency changes in AAM, a power spectrum of the terms in the global AAM budget (Eq. 4) was computed. To do so we calculated the power spectral density of the angular momentum tendency and torque terms at a bandwidth of 0.0036 day^{-1} during the interval February 1992 to November 1996. It is clear from the resulting spectrum in Fig. 2 that although the level in the power in the mountain and friction torques are generally comparable on time scales longer than about a 15 days, mountain torque substantially dominates friction torque on shorter time scales. At these highest frequencies, the power in the mountain torque is nearly equivalent to that in the global angular momentum tendency, a fact that is also evident from examination of a series in the time domain, such as Fig. 1 of Salstein et al. (1996). Furthermore, this strong dominance of the mountain torque is consistent with the results of Madden and Speth (1995), who found that on time scales of 5-20 days, it is more closely related to changes in AAM than is the friction torque. Thus, for purposes of studying rapid fluctuations in AAM shorter than two weeks, we will focus upon the characteristics of mountain torque alone and we can safely neglect further consideration of the friction torque.

The presence of known major spectral peaks in Fig. 2, though at lower frequencies than is our present focus, gives us additional confidence in the general utility of the NCEP torque series

used here. For example, there are spectral peaks in the current series in both mountain and friction torque at about 360, 180, and 33 days These peaks have been previously identified in AAM by Eubanks et al. (1985) and others. The peaks near 360 and 180 days are a result of the strong annual and semiannual oscillation of AAM, respectively (Rosen and Salstein 1985) and that at 33 days is likely related to the mechanism identified by Madden and Julian (1971). Although it is a tropical oscillation often identified with fluctuations across the Pacific Ocean, this Madden-Julian oscillation is also associated with changes in AAM (Anderson and Rosen 1983; Weickmann et al. 1997).

a. Zonally-integrated mountain torque variance

As a first step towards isolating the regions responsible for the high-frequency fluctuations in global AAM, we determine which latitude bands contain the most mountain torque variance at frequencies shorter than two weeks. To do so, we integrated the gridded mountain torque fields around a belt of constant latitude using the relationship:

$$\langle T_m \rangle = -\frac{a^2 \pi}{180} \cos\phi \int_0^{2\pi} p_s \frac{\partial H}{\partial \lambda} d\lambda \qquad (7)$$

which yields the zonally-integrated mountain torque per degree latitude. Then the temporal variance of $\langle T_m \rangle$ was computed in 14-day moving windows centered on every day in the period April 1993 to April 1996. This calculation effectively provided a time series of high-frequency mountain torque variance in each latitude band without the need to digitally filter the series first. (The variance was also computed using data that was first high-pass filtered, and the results were quantitatively similar, giving us confidence in the ability of the 14-day moving window to remove lower frequency oscillations). The calendar dates for the three-year period were then averaged to yield a time average of the zonally-integrated mountain torque variance in each latitude band. The mean annual cycle at different latitudes is shown in a Hovmöller diagram in Fig. 3. The high-

frequency variance displays maxima in the midlatitudes of the Northern and Southern Hemispheres along 40°N and 25°S respectively. Further, each hemisphere has a relative maximum in its cool season, with the maximum in the Northern exceeding that of the Southern Hemisphere. The polar regions contain significantly less variance, although they do have peaks during their respective cool seasons near such high features as the Antarctic and the lands bordering the Arctic Ocean. The high-frequency variance in the Tropics is negligible.

The latitude bands that contain the largest variance at high frequencies contain several major mountain ranges, and we wish to assess the relative contribution of the continental regions containing these individual ranges to the total torque variance in the latitude band. For simplicity we divided the latitude bands into two regions (A and B), so that, for example, the contribution from the two regions to the total variance in that band is given by the relationship:

$$\mathrm{cov}(A, A+B) + \mathrm{cov}(B, A+B) = \mathrm{var}(A+B). \tag{8}$$

To define the boundaries of the regions, we selected two regions in each midlatitude band that broadly contained the major mountain ranges of the midlatitudes (Fig. 4a). The northern and southern boundaries of the regions were chosen to contain the main areas of variance shown in Fig. 3. The eastern and western boundaries were chosen to separate the major mountain ranges such as the Rockies, Himalayas, Andes, and the mountains of southern Africa. For convenience, we have included Australia and Africa within the same Southern Hemisphere region. Furthermore, it was desirable that the eastern and western boundaries lie at sea level to yield a more accurate computation of the area-averaged mountain torque (Wei and Schaack 1984).

Next, the gridded mountain torque was summed within the areas of each of the four regions of the two midlatitude bands. Then the three terms in (8) were computed in 14-day moving windows for the two latitude bands (20°N to 60°N and 10°S to 40°S). The contributions

from the four broad continental regions to the total mountain torque variance in each band are illustrated in Fig. 4b. Eurasia and North America contribute about equally to the total variance in the Northern Hemisphere midlatitude band. At times an individual region dominates the total in the band; a striking example of this behavior occurred over Eurasia in February 1996. In the Southern Hemisphere, the Andes are primarily responsible for the high-frequency fluctuations in that hemisphere's mountain torque, with less contribution from Africa. The variance in the Southern Hemisphere is generally of less magnitude than in the Northern, as previously noted in Fig. 3, and the largest such variance occurs in each hemisphere's cool season.

Fig. 4b also shows that the period of January to March 1996 exhibited considerable variance in Northern Hemisphere mountain torque. The fluctuations during this period significantly exceeded the two earlier Northern Hemisphere cool seasons. In particular, there was a significant event of a large mountain torque fluctuation in each of the three calendar months. The time series of the mountain torque in the two Northern Hemisphere midlatitude regions for the period 1 January 1996 to 31 March 1996 (Fig. 5) reveals the details of the three notable events. In early January 1996, both regions experienced a significant increase and then decrease in mountain torque. Second, during mid-February, the mountain torque across Eurasia decreased greatly, then increased sharply, but was partly offset by a weaker fluctuation in the opposite sense in the North America region. Third, in mid-March, both regions experienced a decrease and then a sharp increase in mountain torque at about the same time.

The combined effect of the North America and Eurasia mountain torque in the midlatitudes demonstrates the important contributions of these regions to the global AAM tendency during early 1996 (Fig. 6a). Throughout this period, the AAM tendency was well represented by the sum of the mountain torque in the two regions of the Northern Hemisphere midlatitudes, with this regional mountain torque correlating with global AAM tendency at r=0.74, and therefore explaining more than half (55%) of the variance in the global AAM tendency during this period. Mountain torque in

these regions do not fully explain the global AAM tendency because the friction torque and mountain torque produced elsewhere of course need to be considered. Throughout the period, the global friction torque was significantly weaker than the mountain torque even during the mid-March case when a lower amplitude fluctuation of the friction torque occurred (not shown), similar in phase to the Northern Hemisphere midlatitude mountain torque, but with amplitude of about one-third. The mountain torque from the other regions was also less than the mountain torque in the Northern Hemisphere midlatitude region by about a factor of three.

Although global high-frequency AAM fluctuations may be affected by the mountain torques in a single midlatitude region (Fig. 5), such as the 8-16 February Eurasian episode, when the sense of the torque over Eurasia and North America is similar, such as during 3-10 January and 8-20 March 1996, the impact upon the global AAM tendency is dramatic. For the entire time series, however, the mountain torque in these two regions is poorly correlated, suggesting that the spectacular events of large fluctuations in AAM tendency brought about by coincident events are not the rule.

Since the angular momentum of the Earth-atmosphere system is conserved on the time scales considered here, but for minor interactions with the ocean (Ponte 1990), AAM fluctuations are often associated with small but measurable changes in the rotation rate of the solid Earth reckoned as changes in the l.o.d. (Rosen and Salstein 1983), as follows:

$$\Delta \text{l.o.d.} = k \bullet \Delta AAM^{*} \qquad (9)$$

where $AAM^{*} = M_r + 0.7M_{\Omega}$ (Barnes et al. 1983) incorporates a small adjustment on the M_{Ω} contribution to account for the response of the non-rigid solid Earth to changes in the mass of the overlying atmosphere. Here, $k = 1.68 \times 10^{-29}$, Δ l.o.d. is in units of seconds, AAM^{*} is in

kg m^2 s^{-1}, and the changes are relative to a reference state appropriate for each quantity. Alternatively, we can relate daily changes of AAM^* to daily changes in l.o.d. through

$$\frac{d}{dt} AAM^* = k^{-1} \frac{d}{dt} \text{l.o.d.} \tag{10}$$

which states that an increase in AAM leads to an increase in l.o.d., and a decrease in AAM results in a shorter day.

We wish to investigate the extent to which the high-frequency fluctuations in AAM tendency shown here are reflected in l.o.d. tendency, given the limits of data set inaccuracy. Relationship (10) is generally valid for early 1996 (Fig. 6b), and is particularly good during the early January and mid-March events. Given the strong relationship between the global AAM tendency and the Northern Hemisphere mountain torque shown in Fig. 6a, this result suggests that this torque was largely responsible for the rapid fluctuations in l.o.d. as a result of the exchange of angular momentum between the atmosphere and solid Earth. This connection between the mountain torque and l.o.d. is especially good during events of large high frequency mountain torque variance.

b. A case study of a strong mountain torque fluctuation

The rapid fluctuations in the Northern Hemisphere midlatitude mountain torque shown in Fig. 6a are, by definition of the mountain torque (Eq. 5), a result of changes in surface pressure on the eastern and western sides of the sloping topography. A case study is presented to establish the relevant synoptics which produce the high-frequency fluctuations mountain torque and global AAM tendency in the dramatic event of mid-March 1996. We have chosen the 700 hPa geopotential fields as representative of the flow aloft and relate the synoptic-scale upper air features

to the surface pressure changes in the vicinity of the mountains. Findings from the early January and mid-February cases were broadly consistent with those presented for the March case.

For the oscillation during mid-March 1996, Fig. 6a shows that relative maxima in Northern Hemisphere mountain torque occur on 8 March and 20 March, and a relative minimum occurs on 15 March. Figure 7 displays the 700 hPa geopotential height field at these three times. On 12 UTC 8 March (Fig. 7a), there is a high pressure ridge along the Rockies with a low pressure trough over the eastern Pacific. Over the Himalayas, a ridge along 100°E extends northward from a center at 30°N to 70°N into Siberia. A trough extends southward along 60°E from a center near 70°N. On 12 UTC 15 March (Fig. 7b), the ridge previously positioned over the Rockies has now been replaced by a trough that extends southwestward from the central United States to over extreme northwestern Mexico, and a second trough is located over British Columbia. A ridge is now present over the eastern Pacific. The ridge previously positioned over the Himalayas at 100°E has now been replaced by a trough that extends from 60°N into eastern China, and a ridge centered at 60°N, 50°E extends southward to 40°N, a region previously occupied by a trough. Thus the midlatitude upper air pattern around the two mountain ranges has reversed during the seven-day period. Inspection of the 700 hPa charts during intermediate times (not shown) reveals that these troughs and ridges can be traced back to the west several days prior, and hence they represent mobile synoptic-scale disturbances in the westerlies. On 12 UTC 20 March (Fig. 7c), a ridge is once again positioned over the Rockies, and a trough is now over the eastern Pacific, largely repeating the synoptic-scale pattern of 12 days earlier (Fig. 7a). Over Eurasia, both the trough over eastern China and the ridge to the west of the Himalayas have weakened considerably during the five-day period.

Figure 8 shows the reflections of the upper air troughs and ridges in the sea level pressure field, a measure of synoptic activity near the surface. On 8 March (Fig. 8a), there is a strong high pressure system to the east of the Rockies that extends from about 60°N to 20°N, located slightly

downstream of the upper ridge in Fig. 7a. Low pressure is situated to the west of the Rockies over the eastern Pacific beneath the trough aloft. Over Eurasia, there is high pressure over northern China that extends from 70°N to 20°N into the East China Sea and positioned just downstream of the upper ridge, and a low pressure trough to the west of the Himalayas along 60°E extends from 80°N to 40°N, and is located beneath the upper trough. These sea level pressure systems show considerable meridional elongation, particularly the high pressure on the eastern sides of the Rockies and Himalayas.

On 15 March (Fig. 8b), the sea level pressure patterns across the Rockies and Himalayas have reversed from the prior time (Fig. 8a). Over North America, there is a low pressure center over the Rockies at 55°N, 110°W, and a low pressure trough extends into eastern Mexico. High pressure is located over the eastern Pacific. Both the high and low pressure systems are positioned slightly downstream of their associated upper level ridge and trough, respectively. Low pressure is positioned over eastern China near 35°N, 105°E, with a strong high pressure system to the west centered near 60°N, 50°E, positioned beneath an upper trough and ridge, respectively. On 20 March (Fig. 8c), a high pressure system once again extends along the eastern slopes of the Rockies all the way equatorward into Central America, which, combined with the low pressure over the eastern Pacific, yields a sea level pressure pattern across the Rockies similar to 8 March (Fig. 8a). Over Eurasia, the pressures directly to the west of the Himalayas have risen slightly as the high previously positioned at 60°N has moved south, while those to the east have risen substantially as the low previously situated over eastern China has tracked away from the region.

The changes in surface pressure in the vicinity of the mountains, which is directly responsible for the mountain torque fluctuations, are shown in Fig. 9. For the period of decreasing Northern Hemisphere mountain torque (and global AAM tendency) between 12 UTC 8 March and 12 UTC 15 March previously shown in Fig. 6a, Fig. 9a illustrates that there are substantial surface pressure rises on the western sides of the mountains and falls on the eastern

sides. This succession increases the westward surface pressure gradient across both mountain ranges, and decreases the mountain torque in both midlatitude regions (Fig. 5) which helps to produce a significant decrease in global AAM tendency (Fig. 6a). During the increase in mountain torque between 15 March to 20 March, there are surface pressure rises on the eastern side of the Rockies and falls on the western side (Fig. 9b). Over Eurasia, the surface pressure rises more on the eastern side of the Himalayas relative to the western side. This sequence of surface pressure changes increases the eastward pressure gradient across the both mountain ranges, increases the local mountain torque (Fig. 5), and helps increase the global AAM tendency (Fig. 6a). Thus the spectacular oscillation of global AAM tendency of mid-March 1996 appears to be responding to the mountain torque in the Northern Hemisphere produced by the substantial simultaneous local surface pressure changes in the vicinity of both the Rockies and Himalayas associated with synoptic-scale features of the general circulation.

c. Composite pressure patterns that produce large AAM changes

The case study illustrated the strong relationship between surface pressure gradients produced by mobile synoptic-scale systems, the mountain torque they produce, and the high-frequency fluctuations in global AAM. We now wish to determine if the pressure patterns responsible for the rapid changes in mountain torque and AAM shown in that strong case were characteristic of those associated with other high-frequency changes in AAM. We also wish to determine the pressure patterns associated with mountain torque fluctuations in other regions of the globe.

To focus on high-frequency fluctuations in AAM, the time series of global AAM tendency was now first high pass filtered using a Lanczos filter (Duchon 1979) containing 43 weights and a half-power point of 14 days. The response function of this reasonably sharp filter is shown in Fig. 10. We next prepared composites of surface pressure based upon phases of the high-pass

filtered AAM tendency. The first sample was defined by days when the global high-pass AAM tendency $\left(\dot{AAM}\right)$ was greater than or equal to +1.5 standard deviations (σ) from the mean, and the second by days when $\dot{AAM} \leq -1.5\sigma$. We then created a composite of surface pressure for these days, called here times when AAM was strongly increasing and strongly decreasing, and the difference in the composite pressure fields of the two samples provides a good indication of the surface pressure patterns present during opposite phases of high-frequency fluctuations in AAM tendency. Given the seasonality of high-frequency mountain torque variance (Figs. 3, 4), composites were formed separately for all months, for the Northern Hemisphere cool season (November to April), and for the Southern Hemisphere cool season (May to October). The composites span the period of April 1994-November 1996.

Figure 11a shows the difference in composite surface pressure between days when AAM is strongly increasing and AAM is strongly decreasing. There are 65 and 72 days in these increasing AAM and decreasing AAM composites, respectively. The surface pressure patterns during the opposite extremes of the AAM tendency have a considerable cross-mountain component near the Rockies, Himalayas, and Andes which indicates the importance of these mountain ranges to high-frequency fluctuations in global $\dot{AAM}$ through the mountain torque. Lesser surface pressure gradients exist across Greenland, the Alps, and southern Africa. The net effect of these surface pressure patterns is to create an eastward directed pressure gradient across the mountains which, through Eq. 5, is consistent with the production of a positive mountain torque and positive AAM tendency.

The composite difference in surface pressure for strongly increasing AAM and strongly decreasing AAM days for the Northern Hemisphere cool season is shown in Fig. 11b. There are 32 and 35 days in these composites, respectively. The patterns have stronger centers in the Northern Hemisphere than in the Southern Hemisphere. Most pronounced are the eastward surface pressure gradients across the Rockies and Himalayas, although there is also an eastward

pressure gradient across Greenland and an indication of an eastward pressure gradient across the Alps. The high pressure to the east of the Rockies is centered in the midwestern United States, and extends the large distance from southern Canada to Central America. The low pressure to the west of the Rockies is centered off the coast of British Columbia, and it extends poleward to Alaska and equatorward to northern Mexico. In the Eurasia region, there is relatively high pressure over eastern China and low pressure to the west of the Himalayas. The high pressure extends well poleward into the northeastern portion of the Asian continent. Such a pressure pattern resembles that responsible for the rapid increase in mountain torque and AAM tendency during the case study of mid-March 1996 discussed above (Fig. 9b). In the Southern Hemisphere, relatively high pressure exists on the eastern side of the Andes and across southern Africa.

A similar composite is shown for the Southern Hemisphere cool season (May to October) in Fig. 11c. There are 33 and 37 days in the strongly increasing AAM and strongly decreasing AAM composites, respectively. The pressure differences across the Northern Hemisphere mountains are greatly diminished while the pressure differences across the Southern Hemisphere mountains are better defined, in agreement with our previous results regarding the seasonal nature of the contributions from the two hemispheres to the high-frequency mountain torque variance. The most notable pattern is situated across the Andes with relatively high pressure centered over Argentina, extending poleward and equatorward along the eastern slopes of the Andes, similar to the configuration of the anticyclone discussed in a case study of a rapid fluctuation in AAM by Salstein and Rosen (1994). Low pressure is situated on the western side of the Andes, creating a significant eastward pressure gradient across the mountains. As in Fig. 11b, there is high pressure to the east of southern Africa and low pressure to the west.

Two other features in the composites are worth mentioning. First, the composite pressure systems have significant meridional elongation along the eastern slopes of all three major mountain ranges, particularly during the cool seasons. This meridional elongation in the lee of the mountains

was previously noted in the case study (Fig. 8) and creates a zonal pressure gradient across the topography of considerable north-south extent. The result is a significant local contribution to the global mountain torque. Additionally, the equatorward extension of the surface pressure features may be important because for a given topography, a larger mountain torque is produced from a fixed pressure gradient at a lower compared to a higher latitude due to the influence of the distance to the Earth's axis of rotation upon the torque (Eq. 5). Thus, these synoptic-scale meridionally elongated pressure systems appear to have a significant impact upon the changes in global AAM on time scales of less than two weeks.

Second, the locations of the centers of surface pressure differences in Fig. 11 are relatively invariant with respect to season. There is some poleward movement of the surface pressure centers from the cool season to the warm season, but for the most part the cool season patterns are simply amplifications of those during the warm season. This relationship indicates that the regions responsible for the high-frequency fluctuations in AAM tendency are nearly invariant, being tied to the Earth's topography, and that only their relative importance changes with season. This result also suggests that by knowing the surface pressure in localized regions, one can obtain considerable information about high-frequency changes in the regional mountain torque and global AAM.

The localized nature of the results in Fig. 11 suggest that a meaningful index of regional mountain torque and high-frequency changes in global AAM can be derived from only a small subset of surface pressure data. For example, two stations were chosen, Wichita, Kansas (ICT, 37.7°N, 97.4°W) and Portland, Oregon (PDX, 45.6°N,122.6°W) that lie near the centers of the surface pressure differences in Fig. 11a that straddle the Rockies. The sea level pressure observations from synoptic hours (00, 06, 12, and 18 UTC) were daily-averaged to be centered at 09 UTC in the same manner as the torque data. The difference in daily-averaged pressure between the two stations is plotted along with the mountain torque in the North America region for the

period of January to March 1996 (Fig. 12a). The two time series correlate very well (r=0.81), indicating that the pressure difference between these two points is a very good indicator of the sense of the mountain torque across the entire North America region.

The sea level pressure difference between these two stations is now plotted with the global AAM tendency in Fig 12b. Changes in sea level pressure difference between these two stations coincide fairly well with the global AAM tendency (r=0.67), and thus a considerable amount of information regarding the global AAM tendency during this three-month period can be gathered simply by knowing the sea level pressure difference between these two North American stations. Future work will focus upon testing the robustness of this relationship between local pressure differences and global AAM for a longer time series and for other regions of the globe, such as in the vicinity of the Himalayas and Andes.

4. Discussion

This study has shown that high-frequency fluctuations in global AAM result primarily from the mountain torque in the midlatitudes of both hemispheres due to changes in surface pressure across the major mountain ranges (Rockies, Himalayas, and Andes) accompanying synoptic-scale systems. A case study was presented to provide an example of the relevant synoptics associated with a rapid modulation of local mountain torque and global AAM. Our results have also indicated that each hemisphere has a maximum in high-frequency mountain torque variance in its cool season.

It is likely, then, that the seasonal dependence of high-frequency mountain torque variance is directly related to the frequency of occurrence of midlatitude synoptic-scale cyclones and anticyclones near the Rockies, Himalayas, and Andes. In support of this conjecture, synoptic climatology studies indicate that in the Northern Hemisphere, there is a cool season maximum in

the frequency of midlatitude cyclones and anticyclones in the vicinity of the Rockies and Himalayas (Petterssen 1956; Whittaker and Horn 1984; Zishka and Smith 1980). In the Southern Hemisphere, Sinclair (1994; 1996) found a cool season maximum of both anticyclone and cyclone frequency in the region of South Africa. To the east of the Andes, there is a maximum of anticyclones frequency in cool season, while cyclones in the vicinity of the Andes are prevalent year-round (Jones and Simmonds 1994; Sinclair 1996; Taljaard 1967). The decrease in cyclone and anticyclone activity from the cool to the warm season is a result of a weakening of the tropospheric meridional temperature gradient and a poleward shift of the upper level storm track. Thus the seasonal changes in high-frequency mountain torque variance found here are consistent with the alteration in synoptic-scale activity from the cool to the warm season of both hemispheres.

The case study and composite study also show considerable meridional elongation of the surface pressure patterns that are associated with strong high-frequency fluctuations in AAM, and this elongation is particularly evident on the lee side of the mountain ranges. For high pressure systems, the meridional elongation is characteristic of synoptic-scale events called 'cold surges' which are associated with marked equatorward penetration of cold air. Cold surges are observed most often during the cool season in the lee of the Rockies (DiMego et al. 1976; Henry 1979), Himalayas (Murakami and Nakamura 1983), and Andes (Hamilton and Tarifa 1978). The equatorward progression of the cold surges is believed to be a result of the interaction between the synoptic-scale flow and the sloping topography (Colle and Mass 1995). In the case of low pressure, westerly airflow over topography often leads to meridionally-elongated surface troughs in the lee of the topographic barrier (Hess and Wagner 1948; Newton 1956). Thus the meridionally-elongated structure of the pressure systems observed in this study is consistent with those synoptic-scale features observed in the vicinity of the mountains. These synoptic-scale features may, by virtue of their meridionally extensive cross-mountain pressure gradient, result in considerable high-frequency fluctuations of mountain torque and therefore AAM tendency.

It is also suggested in this study that the large fluctuations in global AAM tendency during early 1996 were reflected in the measurements of changes in the length of day, and that the mountain torque is the primary mechanism by which angular momentum is exchanged between the atmosphere and solid Earth on these short time scales. Previous studies (Rosen et al. 1984; Salstein and Rosen 1994; Wolf and Smith 1987) also identify this relationship between AAM and l.o.d. for isolated cases of high-frequency fluctuations in AAM. When viewed over a longer time series, however, high-frequency fluctuations in l.o.d. are poorly related to fluctuations in AAM (Rosen et al. 1990), and the lack of agreement is attributed to declining signal-to-measurement noise ratios of both data types (Dickey et al. 1992). It is also possible that the poor relationship is produced by the inclusion of many smaller, poorly measured events while large-amplitude episodes of AAM fluctuations are indeed detectable.

To test this hypothesis, we return to the time series of high-pass filtered AAM tendency and we calculate a number of correlation coefficients between daily changes in l.o.d and AAM, based on the strength of the daily AAM changes. For the entire time series, such a correlation is 0.39. If we select only those days when $|A\dot{A}M| \geq 1.5\sigma$ the correlation increases to 0.59, and for days when $|A\dot{A}M| \geq 2.0\sigma$, the correlation grows further to 0.71. These results indicate that for the cases of sufficiently strong high-frequency fluctuations in AAM, the exchange in angular momentum between the solid Earth and atmosphere through the mountain torque is reasonable well-captured by the current analysis systems and l.o.d. observing networks.

5. Conclusions

This study sought to identify the relative role of the mountain vs. friction torque to the high-frequency ($\leq$ 14 day) fluctuations in global AAM tendency, isolate the regions responsible for these fluctuations, and suggest a mechanism in the global circulation responsible for the high-frequency fluctuations. We find that the mountain torque is much more important than the friction

torque in the global balance of atmospheric angular momentum on high frequencies. On time scales greater than about three weeks, however, the friction torque begins to play a more significant role. The midlatitudes of both hemispheres are primarily responsible for the high-frequency fluctuations in mountain torque and global AAM.

To identify the mechanism responsible for the high-frequency fluctuations, first a case study was performed during an extraordinary fluctuation in mountain torque and AAM tendency in mid-March 1996. The case study revealed that the mountain torque fluctuations were a result of changes in the surface pressure gradient across a wide north-south extent of both the Rockies and Himalayas, brought about by migratory synoptic-scale weather systems as they traversed these mountain ranges. The resulting regional mountain torque then impacted the global AAM on synoptic time scales, and caused a coincident fluctuation in l.o.d. This result is consistent with those of previous case studies involving high-frequency fluctuations in AAM.

A composite study using a time series of global AAM tendencies and gridded surface pressure showed that the surface pressure gradients in the vicinity of the Rockies, Himalayas, and Andes, and to a lesser extent southern Africa, were routinely associated with significant high-frequency fluctuations in AAM tendency. The pressure differences across the Rockies and Himalayas of the Northern Hemisphere play a major role in the high-frequency fluctuations in AAM tendency during the Northern Hemisphere cool season (November to April), whereas the Andes in the Southern Hemisphere were most important in the Southern Hemisphere cool season (May to October). Further, the composites suggest that as in the case study, the surface pressure systems responsible for the most notable high-frequency fluctuations in global AAM tendency exhibit considerable meridional elongation, particularly on the eastern sides of the topography, which is characteristic of synoptic-scale systems in the lee of mountains. This meridional elongation results in a zonal pressure gradient across the mountains spanning many latitudes, and helps to produce significant local mountain torque fluctuations and hence global AAM fluctuations

on synoptic time scales. These relatively large amplitude mountain torque fluctuations were able to produce changes in l.o.d. consistent with an exchange of momentum between the solid Earth and atmosphere through the mountain torque.

Lastly, it was suggested that the sea level pressure differences at a limited set of stations can yield considerable information about the mountain torque over a broad continental region and, to a lesser extent, the global AAM tendency. Future work will attempt to more precisely isolate the regions responsible for high-frequency mountain torque variations through the development of a mountain torque index based upon sea level pressure differences from station data. The development of such an index based upon the historical record of sea level pressures may allow for the study of mountain torque and AAM fluctuations over a longer period than is possible from an analysis system alone. Further, in light of the connection between synoptic-scale pressure changes at the surface and disturbances aloft, the dependence of mountain torque variance upon midlatitude flow regimes and upper-level storm track position will be investigated.

Acknowledgments:

We wish to thank Glenn White at NCEP who provided us with the torque and AAM data used in this study, Richard Gross at JPL for the l.o.d. data, and Karen Cady-Pereira and Peter Nelson for archiving the data at AER and providing software support. Gratitude is also expressed to Richard Rosen for his thoughtful review of the manuscript, and Klaus Weickmann for his comments on the work. Helpful suggestions were also provided by Lance Bosart and Ed Bracken. Our use of the NCAR data archive is acknowledged. Support for this project was provided by NASA Mission to Planet Earth awards NAGW-2615 and NAS5-32861 and by the NOAA Climate and Global Change Program under award NA46GP01212E.

References:

Anderson, J.D., and R.D. Rosen, 1983: The latitude-height structure of 40-50 day variations in atmospheric angular momentum. *J. Atmos. Sci.*, **40**, 1584-1591.

Barnes, R.T., H.R. Hide, A.A. White, and C.A. Wilson, 1983: Atmospheric angular momentum fluctuations, length-of-day changes and polar motion. *Proc. Roy. Soc. London, Ser. A.*, **387**, 31-73.

Colle, B.A., and C.F. Mass, 1995: The structure and evolution of cold surges east of the Rocky mountains. *Mon. Wea. Rev.*, **123**, 2577-2610.

Czarnetzki, A.C., 1997: Regional mountain torque estimates over the Rocky mountains in lee cyclones. *J. Atmos. Sci.*, **54**, 1986-1997.

Dickey, J.O., S.L. Marcus, J.A. Steppe, and R. Hide, 1992: The Earth's angular momentum budget on subseasonal time scales. *Science*, **255**, 321-255.

DiMego, G.J., L.F. Bosart, and G.W. Endersen, 1976: An examination of the frequency and mean conditions surrounding frontal incursions into the Gulf of Mexico and Caribbean Sea. *Mon. Wea. Rev.*, **104**, 709-718.

Duchon, C.E., 1979: Lanczos filtering in one and two dimensions. *J. Appl. Meteor.*, **18**, 1016-1022.

Eubanks, T.M., J.A. Steppe, J.O. Dickey, and P.S. Callahan, 1985: A spectral analysis of the earth's angular momentum budget. *J. Geophys. Res.*, **90**, 5385-5404.

Gross, R.S., 1996: Combinations of Earth orientation measurements: SPACE94, COMB94, and POLE94. *J. Geophys. Res.*, **101**, 8729-8740.

Hamilton, M.G., and J.R. Tarifa, 1978: Synoptic aspects of a polar outbreak leading to frost in tropical Brazil, July 1972. *Mon. Wea. Rev.*, **106**, 1545-1556.

Henry, W.K., 1979: Some aspects of the fate of cold fronts in the Gulf of Mexico. *Mon. Wea. Rev.*, **107**, 1078-1082.

Hess, S.L., and H. Wagner, 1948: Atmospheric waves in the northwestern United States. *J. Meteor.*, **5**, 1-19.

Jones, D.A., and I. Simmonds, 1994: A climatology of Southern Hemisphere anticyclones. *Climate Dyn.*, **10**, 333-348.

Kanamitsu, M., 1989: Description of the NMC global data assimilation and forecast system. *Wea. Forecasting*, **4**, 335-342.

Madden, R.A., and P.R. Julian, 1971: Detection of a 40-50 day oscillation in the zonal wind in the tropical Pacific. *J. Atmos. Sci.*, **28**, 702-708.

Madden, R.A., and P. Speth, 1995: Estimates of atmospheric angular momentum, friction, and mountain torques during 1987-1988. *J. Atmos. Sci.*, **52**, 3681-3694.

Murakami, T., and H. Nakamura, 1983: Orographic effects on cold surges and lee-cyclogenesis as revealed by a numerical experiment. *J. Meteor. Soc. Japan*, **61**, 547-566.

Newton, C.W., 1956: Mechanisms of circulation change during a lee cyclogenesis. *J. Meteor.*, **13**, 528-539.

Newton, C.W., 1971: Mountain torques in the global angular momentum balance. *J. Atmos. Sci.*, **28**, 623-628.

Petterssen, S., 1956: *Weather Analysis and Forecasting*. McGraw-Hill, 422 pp.

Ponte, R.M., 1990: Barotropic motions and the exchange of angular momentum between the oceans and solid Earth. *J. Geophys. Res.*, **95**, 11369-11374.

Rosen, R.D., 1993: The axial momentum balance of earth and its fluid envelope. *Surveys in Geophysics*, **14**, 1-29.

Rosen, R.D., and D.A. Salstein, 1983: Variations in atmospheric angular momentum on global and regional scales and the length of day. *J. Geophys. Res.*, **88**, 5451-5470.

Rosen, R.D., and D.A. Salstein, 1985: Contribution of the stratospheric winds to annual and semiannual fluctuation in atmospheric angular momentum. *J. Geophys. Res.*, **90**, 8033-8041.

Rosen, R.D., D.A. Salstein, T.M. Eubanks, J.O. Dickey, and J.A. Steppe, 1984: An El Niño signal in atmospheric angular momentum and earth rotation. *Science*, **225**, 411-414.

Rosen, R.D., D.A. Salstein, and T.M. Wood, 1990: Discrepancies in the Earth-Atmosphere angular momentum budget. *J. Geophys. Res.*, **95**, 265-279.

Salstein, D.A., K. Cady-Pereira, C.-K. Shum, and J. Xu, 1996: ERS-1 scatterometer observations of ocean surface winds as applied to the study of the earth's momentum balance. *8th Conf. on Satellite Meteorology and Oceanography*, Atlanta, GA, Amer. Meteor. Soc., p. 439-442.

Salstein, D.A., and R.D. Rosen, 1994: Topographic forcing of the atmosphere and a rapid change in the length of day. *Science*, **264**, 407-409.

Sinclair, M.R., 1994: An objective cyclone climatology for the Southern Hemisphere. *Mon. Wea. Rev.*, **122**, 2239-2256.

Sinclair, M.R., 1996: A climatology of anticyclones and blocking for the Southern Hemisphere. *Mon. Wea. Rev.*, **124**, 245-263.

Starr, V.P., 1948: An essay on the general circulation of the earth's atmosphere. *J. Meteor.*, **5**, 39-43.

Swinbank, R., 1985: The global atmospheric angular momentum balance inferred from analyses made during the FGGE. *Quart. J. Roy. Meteor. Soc.*, **111**, 977-992.

Taljaard, J.J., 1967: Development, distribution and movement of cyclones and anticyclones in the Southern Hemisphere during the IGY. *J. Appl. Meteor.*, **6**, 973-987.

Wei, M.-Y., and T.K. Schaack, 1984: Seasonal distributions of mountain torques during FGGE. *J. Atmos. Sci.*, **41**, 3032-3039.

Weickmann, K.M., G.N. Kiladis, and P.D. Sardeshmukh, 1997: The dynamics of intraseasonal atmospheric angular momentum oscillations. *J. Atmos. Sci.*, **54**, 1445-1461.

White, G.H., 1991: Mountain and surface stress torques in NMC analyses. *Proceedings of the AGU Chapman conference on geodetic VLBI: Monitoring global change*, Washington, D.C., National Geodetic Information Branch, NOS/NOAA, p. 262-269.

White, R.M., 1949: The role of mountains in the angular-momentum balance of the atmosphere. *J. Meteor.*, **6**, 353-355.

Whittaker, L.M., and L.H. Horn, 1984: Northern Hemisphere extratropical cyclone activity for four mid-season months. *J. Climatol.*, **4**, 297-310.

Wolf, W.L., and R.B. Smith, 1987: Length-of-day changes and mountain torque during El Niño. *J. Atmos. Sci.*, **44**, 3656-3660.

Zishka, K.M., and P.J. Smith, 1980: The climatology of cyclones and anticyclones over North America and surrounding ocean environs for January and July, 1950-77. *Mon. Wea. Rev.*, **108**, 387-401.

Figure captions:

Figure 1. Daily time series of the global AAM tendency (dotted) and the sum of the global friction and mountain torque (solid) for the period 1 November 1995 to 1 November 1996. Units are X 10^{19} kg m^2 s^{-2}.

Figure 2. Log-log power spectrum with period of global angular momentum tendency (solid), global mountain torque (dotted), and global friction torque (dash-dot) based upon data for the period February 1992 to November 1996. Units are (X 10^{18} kg m^2 $s^{-2})^2$•day. The periodogram is smoothed using a 5-point moving average in frequency.

Figure 3. Three year mean variance of zonally-integrated mountain torque in 14-day moving windows shown as a function of latitude and time. Units are (X 10^{18} kg m^2 $s^{-2})^2$ per degree latitude. Contours are drawn every 0.2, and values $\geq$ 0.6 are shaded.

Figure 4. a) Boxes defining four midlatitude domains used in the study to compute the regional mountain torque. The Eurasia box and North America boxes are bounded by latitudes 20°N and 60°N, and separated by longitudes 20°W and180°. The Africa and South America boxes are bounded by latitudes 10°S and 40°S, and separated by longitudes 0° and 180°. Shading indicates elevation $\geq$1000 m from the Rand 1° x 1° topography grid. b) Contribution to the total variance in a latitude band by the two continental regions in that band, as well as total band variance. Units are (X 10^{19} kg m^2 $s^{-2})^2$.

Figure 5. Daily time series of the mountain torque in the Eurasia region (solid) and North America region (dotted) for the period 1 January 1996 to 31 March 1996. Units are X 10^{19} kg m^2 s^{-2}. The bars beneath the time series highlight the three episodes mentioned in the text.

Figure 6. a) Daily time series of the sum of the mountain torque in the North America and Eurasia regions (solid) and the global atmospheric angular momentum tendency (dotted) for the period 1 January 1996 to 31 March 1996. b) Daily time series of global atmospheric angular momentum tendency from NCEP analysis (dash-dot) and inferred from measurements of l.o.d. (solid). Units are X 10^{19} kg m^2 s^{-2}.

Figure 7. Geopotential height of the 700 hPa level at 12 UTC for a) 8 March, b) 15 March, and c) 20 March 1996. Contours are every 6 dam. Highs and lows discussed in the text are indicated by the letters 'H' and 'L'.

Figure 8. Sea level pressure at 12 UTC for a) 8 March, b) 15 March, and c) 20 March 1996. Contours are every 6 hPa. Highs and lows discussed in the text are indicated by the letters 'H' and 'L'.

Figure 9. a) Difference in surface pressure between 12 UTC 15 March and 12 UTC 8 March 1996 (every 4 hPa contoured, zero line omitted). Positive contours are solid and negative dashed. b) Same as a) except between 12 UTC 20 March and 12 UTC 15 March. Shading indicates surface elevation $\geq$ 1000 m.

Figure 10. Response function of the high pass filter used in the study, plotted linearly in frequency but marked in period. The filter contains 43 weights, and a half-power point of 14 days.

Figure 11. The difference in surface pressure (contoured every 1 hPa) for days when the global high pass AAM tendency is $\geq$ +1.5 standard deviations and days when the global high pass AAM tendency $\leq$ -1.5 standard deviations from the mean for a) all months, b) November to April and c)

May to October. Shading indicated regions of statistical significance at the 95% confidence level as estimated by a Student's-t test. Positive values are solid and negative values are dashed.

Figure 12. Daily time series of the difference in sea level pressure (solid, units hPa) between Wichita, Kansas (ICT, 37.7°N, 97.4°W) and Portland, Oregon (PDX, 45.6°N, 122.6°W) plotted with a) mountain torque over North America (dotted, units X 10^{18} kg m^2 s^{-2}) and b) global atmospheric angular momentum tendency (dotted, units X 10^{18} kg m^2 s^{-2}) for the period 1 January to 31 March 1996. Note that the curves are plotted with two different scales.

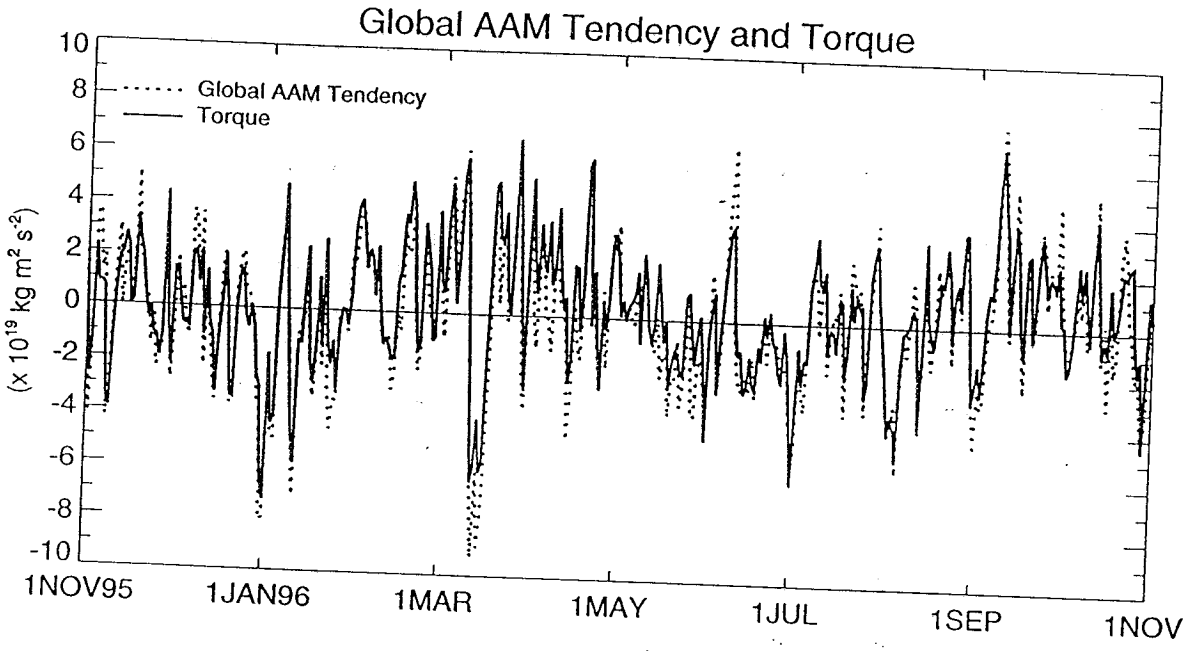
Global AAM Tendency and Torque
Global AAM Tendency
Torque
(x 10^19 kg m^2 s^-2)
10
8
6
4
2
0
-2
-4
-6
-8
-10
1NOV95
1JAN96
1MAR
1MAY
1JUL
1SEP
1NOV

FIG. 1

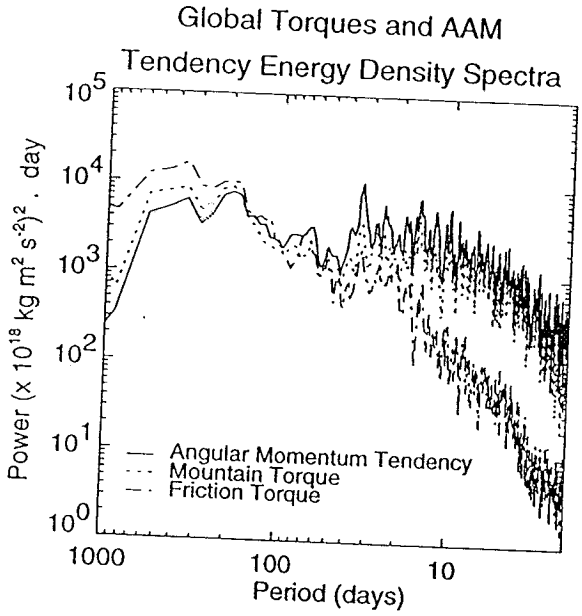
Global Torques and AAM
Tendency Energy Density Spectra
Power (x 10^18 kg m^2 s^-2)^2 . day
10^5
10^4
10^3
10^2
10^1
10^0
1000
100
10
Period (days)
Angular Momentum Tendency
Mountain Torque
Friction Torque

FIG 2.

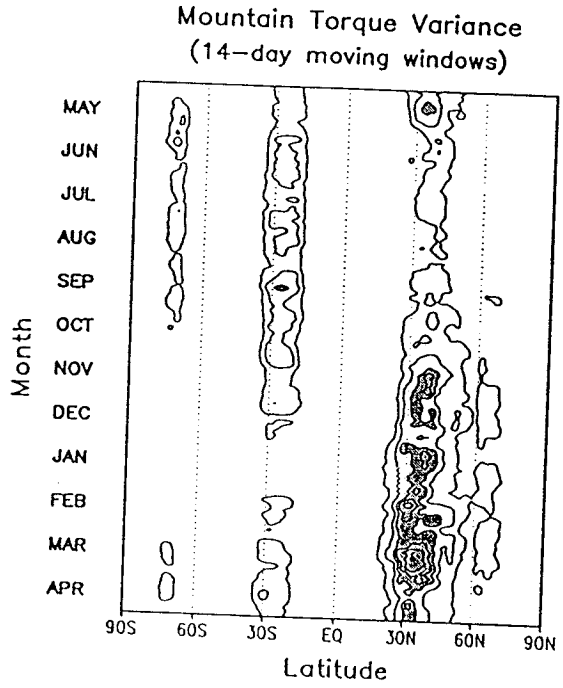
Mountain Torque Variance
(14–day moving windows)
MAY
JUN
JUL
AUG
SEP
OCT
NOV
DEC
JAN
FEB
MAR
APR
Month
90S
60S
30S
EQ
30N
60N
90N
Latitude

FIG. 3

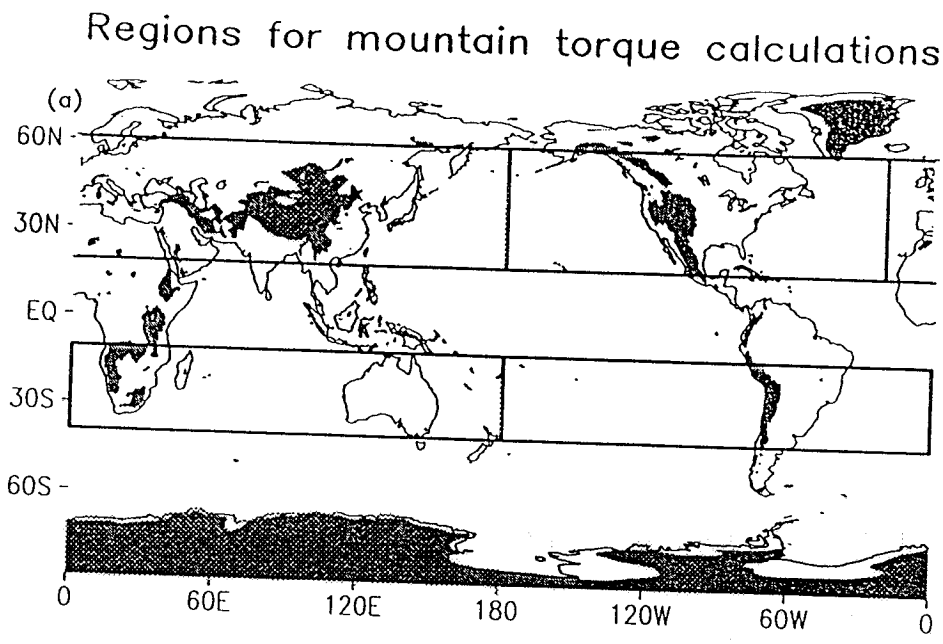
Regions for mountain torque calculations
(a)
60N
30N
EQ
30S
60S
0
60E
120E
180
120W
60W
0

FIG. 4a.

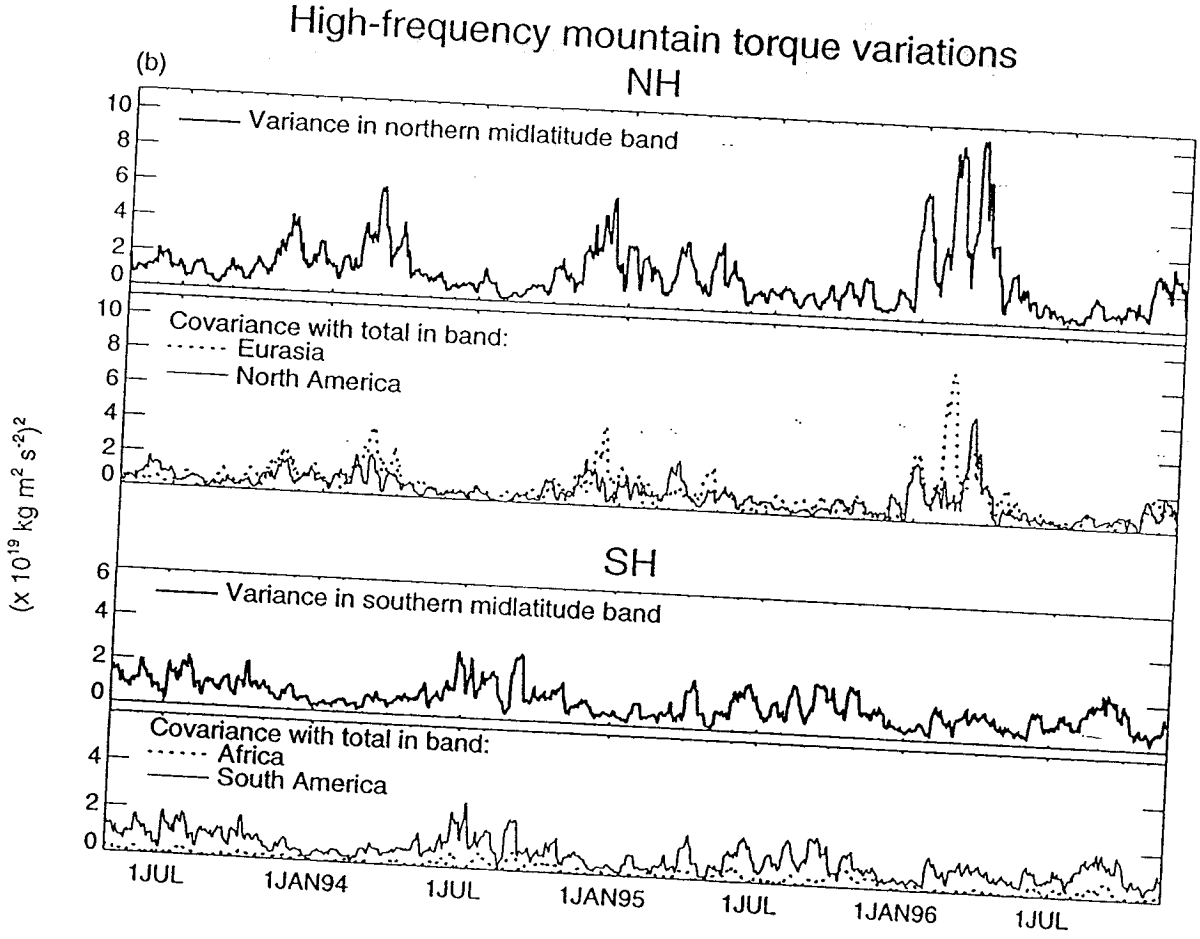
High-frequency mountain torque variations
(b)
NH
Variance in northern midlatitude band
Covariance with total in band:
Eurasia
North America
SH
Variance in southern midlatitude band
Covariance with total in band:
Africa
South America
(x 10^19 kg m^2 s^-2)^2
1JUL
1JAN94
1JUL
1JAN95
1JUL
1JAN96
1JUL

FIG. 4b

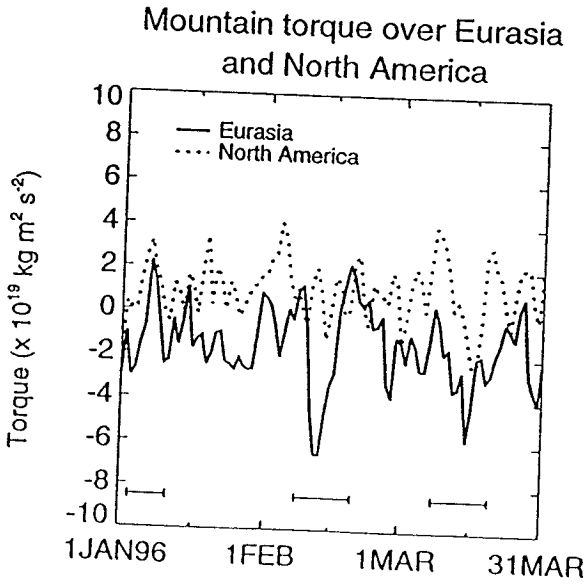
Mountain torque over Eurasia
and North America
Eurasia
North America
Torque (x 10^19 kg m^2 s^-2)
10
8
6
4
2
0
-2
-4
-6
-8
-10
1JAN96
1FEB
1MAR
31MAR

FIG. 5

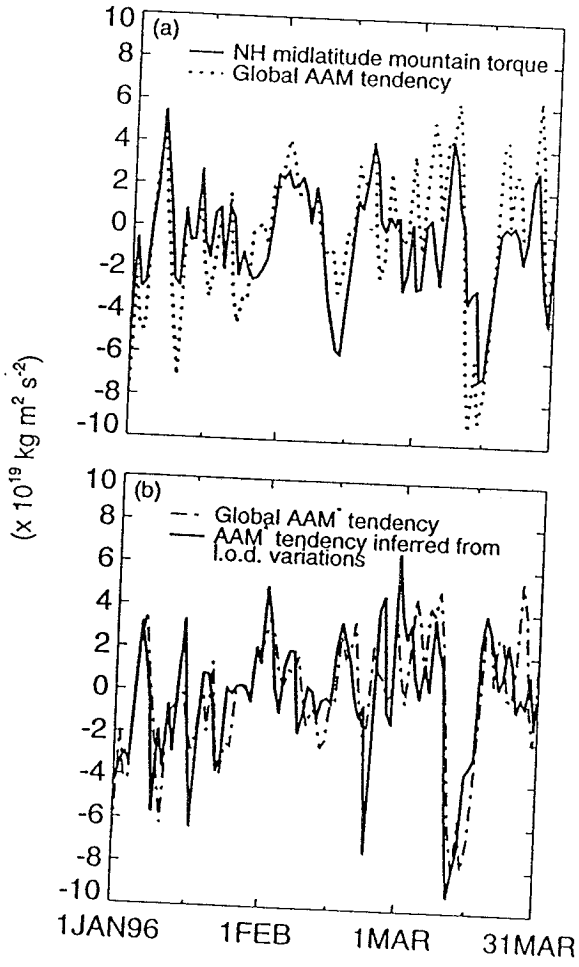
(a)
NH midlatitude mountain torque
Global AAM tendency
(b)
Global AAM tendency
AAM tendency inferred from l.o.d. variations
(x 10^19 kg m^2 s^-2)
10
8
6
4
2
0
-2
-4
-6
-8
-10
1JAN96
1FEB
1MAR
31MAR

FIG. 6

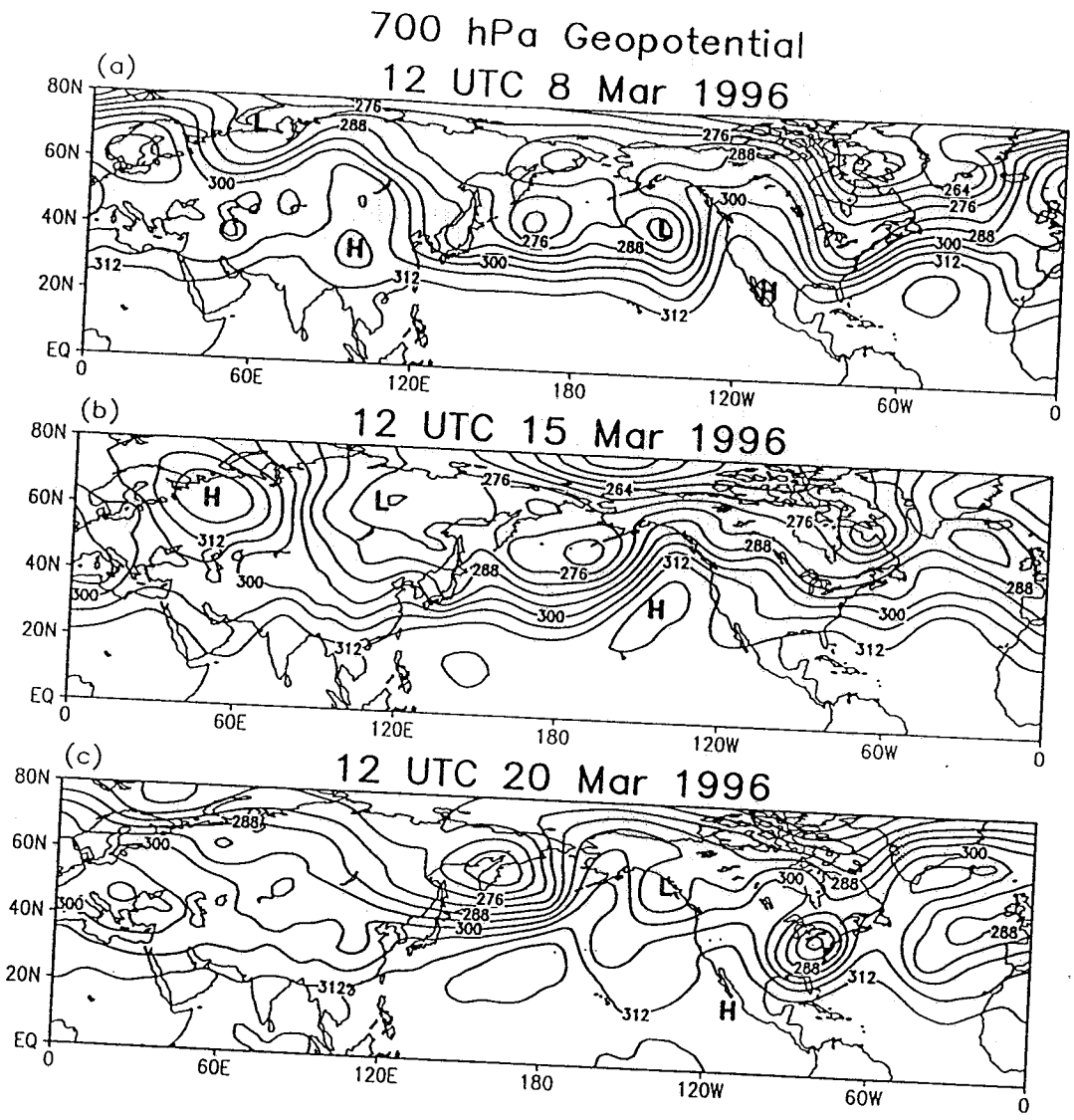
700 hPa Geopotential
(a)
12 UTC 8 Mar 1996
(b)
12 UTC 15 Mar 1996
(c)
12 UTC 20 Mar 1996
80N
60N
40N
20N
EQ
0
60E
120E
180
120W
60W
H
L
276
288
300
312
264

FIG. 7.

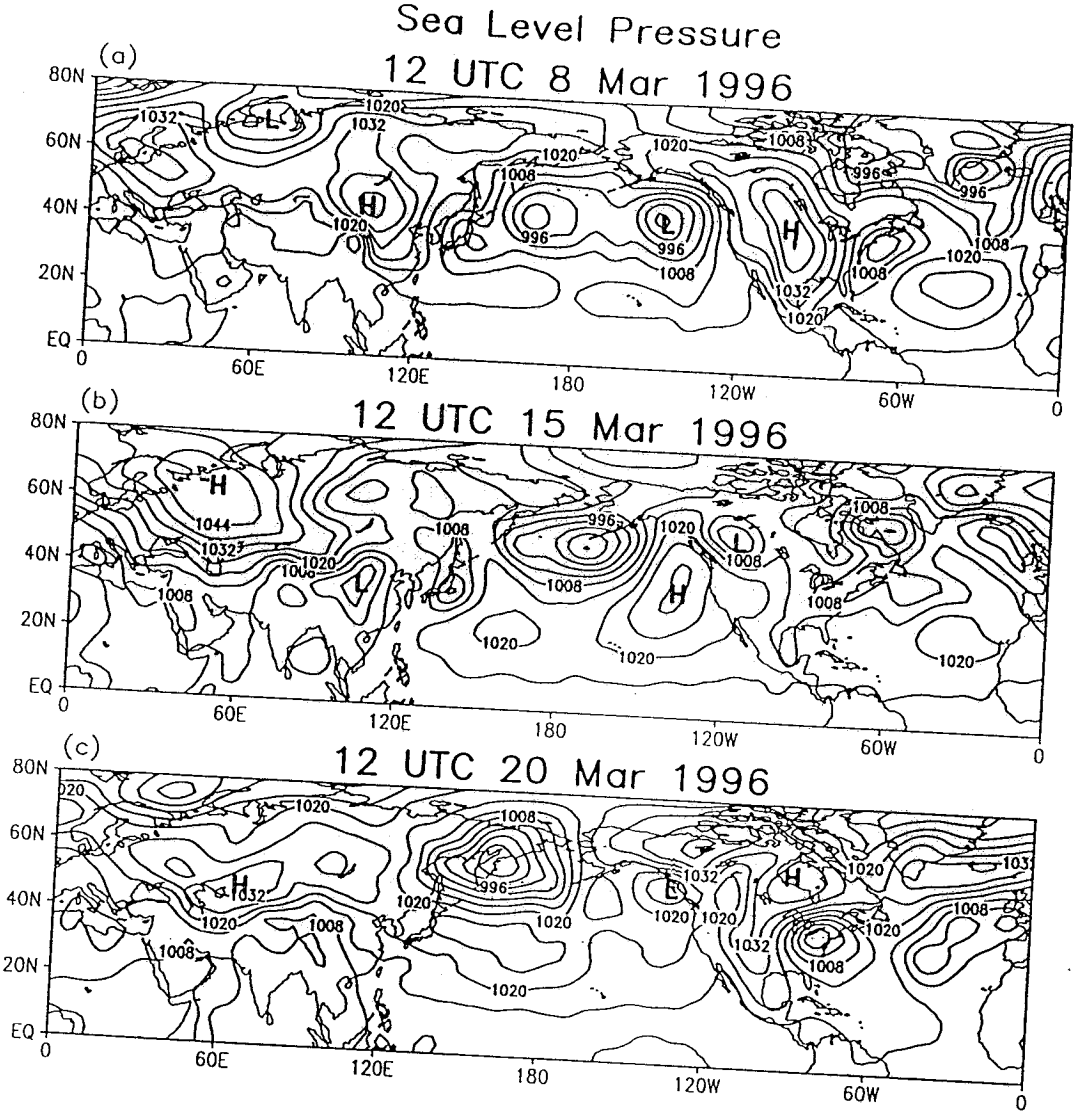
Sea Level Pressure
(a)
12 UTC 8 Mar 1996
(b)
12 UTC 15 Mar 1996
(c)
12 UTC 20 Mar 1996
80N
60N
40N
20N
EQ
0
60E
120E
180
120W
60W
0

FIG. 8

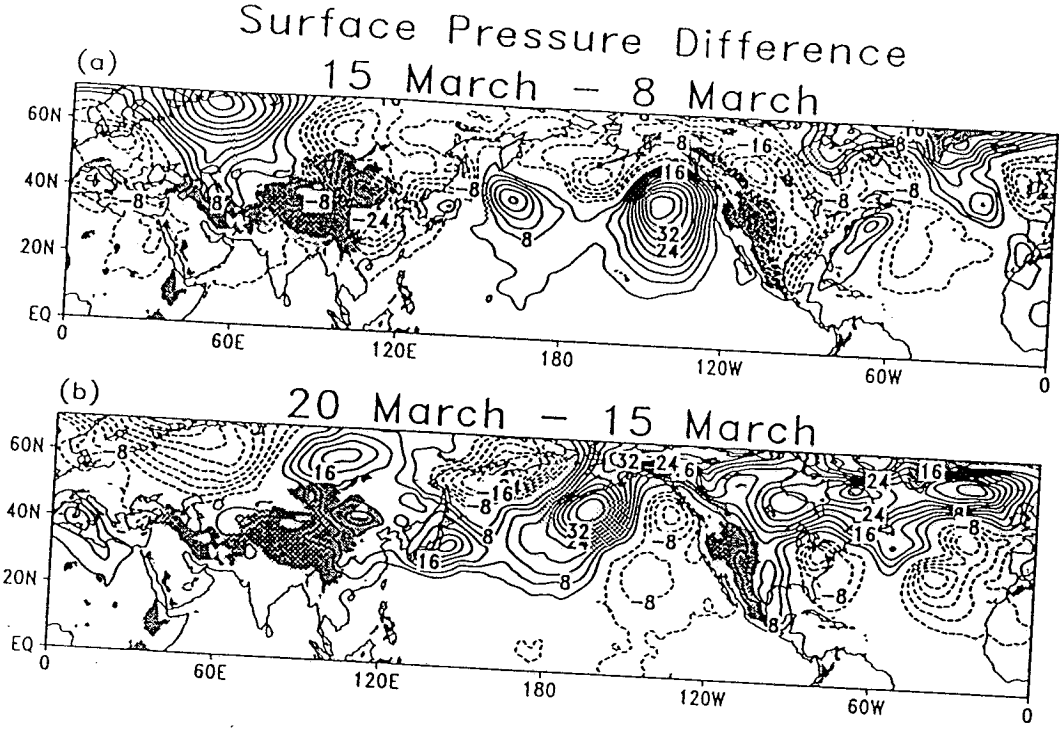
Surface Pressure Difference
(a)
15 March − 8 March
60N
40N
20N
EQ
0
60E
120E
180
120W
60W
0
(b)
20 March − 15 March
60N
40N
20N
EQ
0
60E
120E
180
120W
60W
0

FIG. 9

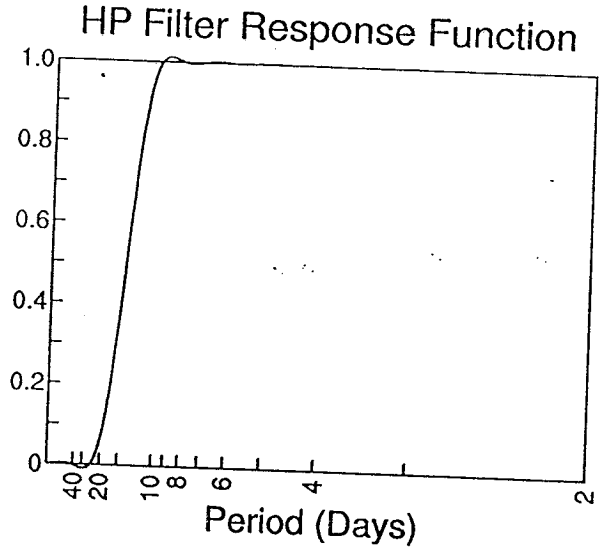
HP Filter Response Function
1.0
0.8
0.6
0.4
0.2
0
40
20
10
8
6
4
2
Period (Days)

FIG. 10

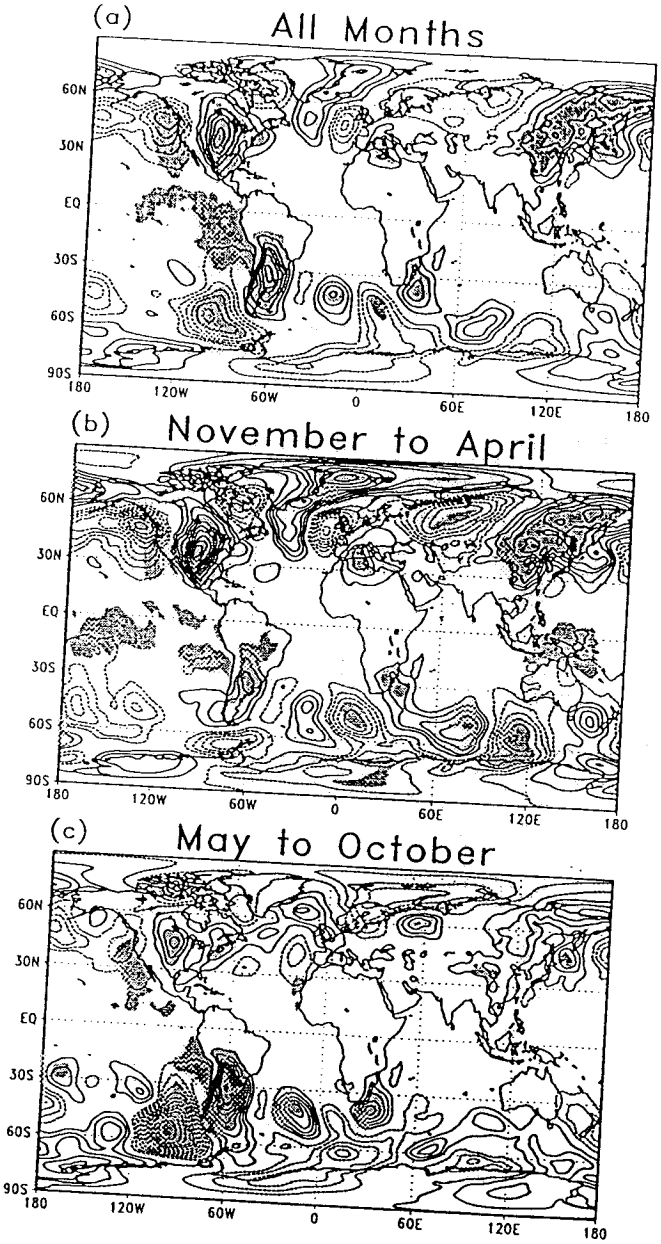
(a)
All Months
60N
30N
EQ
30S
60S
90S
180
120W
60W
0
60E
120E
180
(b)
November to April
60N
30N
EQ
30S
60S
90S
180
120W
60W
0
60E
120E
180
(c)
May to October
60N
30N
EQ
30S
60S
90S
180
120W
60W
0
60E
120E
180

FIG. 11

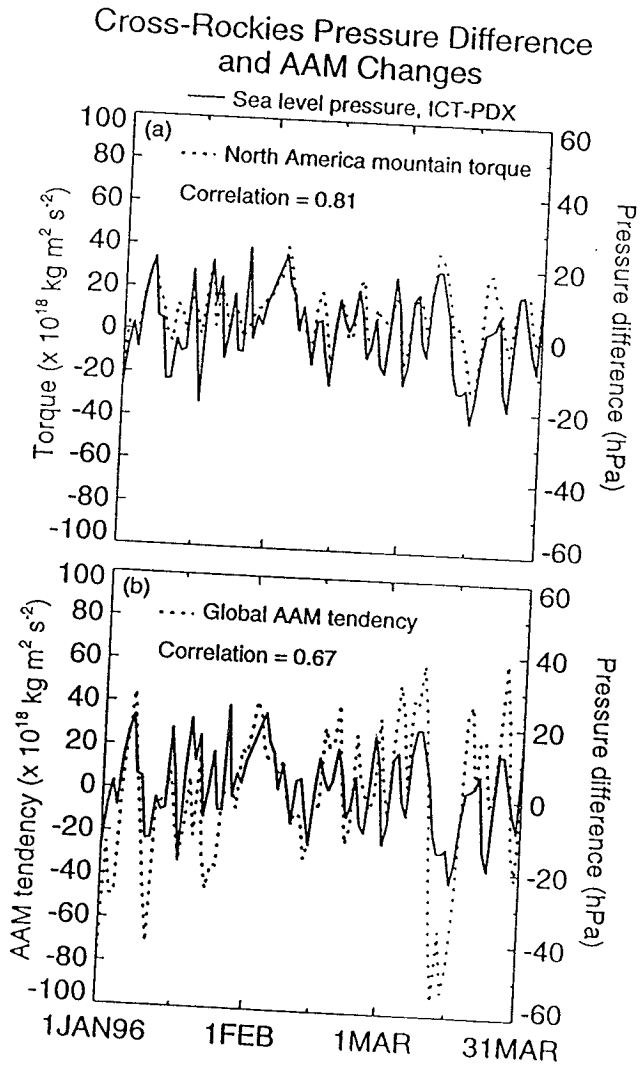
Cross-Rockies Pressure Difference
and AAM Changes
Sea level pressure, ICT-PDX
(a)
North America mountain torque
Correlation = 0.81
Torque (x 10^18 kg m^2 s^-2)
Pressure difference (hPa)
(b)
Global AAM tendency
Correlation = 0.67
AAM tendency (x 10^18 kg m^2 s^-2)
Pressure difference (hPa)
1JAN96
1FEB
1MAR
31MAR

FIG. 12.

NASA
National Aeronautics and Space Administration

Report Documentation Page

1. Report No.	2. Government Accession No.	3. Recipient's Catalog No.
P602 Final		

4. Title and Subtitle	5. Report Date
FINAL REPORT ON DIAGNOSTIC STUDIES WITH GLA FIELDS	December 1997
	6. Performing Organization Code

7. Author(s)	8. Performing Organization Report No.
David A. Salstein	
	10. Work Unit No.

9. Performing Organization Name and Address	11. Contract or Grant No.
Atmospheric and Environmental Research, Inc. 840 Memorial Drive Cambridge, MA 02139	NAS 5-32861

12. Sponsoring Agency Name and Address	13. Type of Report and Period Covered
National Aeronautics and Space Administration Washington, DC 20546-0001	Final 1995 - 1997
	14. Sponsoring Agency Code

15. Supplementary Notes

16. Abstract

Assessments of the NASA Goddard Earth Observing System-1 Data Assimilation System(GEOS-1 DAS), regarding heating rates, energetics, and angular momentum quantities were made. These diagnostics can be viewed as measures of climate variability. Comparisons with the NOAA/NCEP reanalysis system of momentum and energetics diagnostics are included. Water vapor and angular momentum are diagnosed in many models, including those of NASA, as part of the Atmospheric Model Intercomparison Project.

The GEOS-1 and NOAA/NCEP global atmospheric angular momentum values are coherent on time scales down to about three days. Furthermore, they agree with the series of Earth angular momentum, as measured by tiny fluctuations in the rotation rate of the Earth, as variations in the length of day. The torques that effect such changes in atmospheric and Earth momentum are dominated by the influence of particular mountain systems, including the Rockies, Himalayas, and Andes, upon mountain torques on time scales shorter than about two weeks. Other project areas included collaboration with Goddard Space Flight Center to examine the impact of mountainous areas and the treatments of parameterizations on diagnoses of the atmosphere. Relevant preprints are included herein.

17. Key Words (Suggested by Author(s))	18. Distribution Statement
global, diagnostics, angular momentum, energetics, water vapor	Unclassified-Unlimited

19. Security Classif. (of this report)	20. Security Classif. (of this page)	21. No. of pages	22. Price
Unclassified	Unclassified		

NASA FORM 1626 OCT 86